Theses and Dissertations

Spring 2017

Longitudinal medical imaging approaches for characterization of porcine cancer models

Emily Marie Hammond
University of Iowa

Recommended Citation

Hammond, Emily Marie. "Longitudinal medical imaging approaches for characterization of porcine cancer models." PhD (Doctor of Philosophy) thesis, University of Iowa, 2017.
http://ir.uiowa.edu/etd/5491.

LONGITUDINAL MEDICAL IMAGING APPROACHES FOR CHARACTERIZATION OF
PORCINE CANCER MODELS

by

Emily Marie Hammond

A thesis submitted in partial fulfillment
of the requirements for the Doctor of Philosophy
degree in Biomedical Engineering in the
Graduate College of
The University of Iowa

May 2017

Thesis Supervisor: Assistant Professor Jessica C. Sieren

Graduate College
The University of Iowa
Iowa City, Iowa

CERTIFICATE OF APPROVAL

_____

PH.D. THESIS

_____

This is to certify that the Ph.D. thesis of

Emily Marie Hammond

has been approved by the Examining Committee for
the thesis requirement for the Doctor of Philosophy degree
in Biomedical Engineering at the May 2017 graduation.

Thesis Committee: _____
                       Jessica C. Sieren, Thesis Supervisor

                       _____
                       Joseph M. Reinhardt

                       _____
                       John D. Newell, Jr.

                       _____
                       Milan Sonka

                       _____
                       Edwin L. Dove

                       _____
                       Eric A. Hoffman

To my husband for his continual support and encouragement of me in this pursuit; I love you. Lastly, to my family for instilling my love of education and pursuit of knowledge and giving me something to strive for.

ABSTRACT

Cancer is the second deadliest disease in the United States with an estimated 1.69 million new cases in 2017. Medical imaging modalities, such as computed tomography (CT) and magnetic resonance imaging (MRI), are widely used in clinical medicine to detect, diagnose, plan treatment, and monitor tumors within the body. Advances in imaging research related to cancer assessment have largely relied on consented human patients, often including varied populations and treatments. Tumor bearing mouse models have been highly valued for basic science research, but imaging focused applications are limited by the translational ability of micro imaging systems. Pig models are well suited to bridge the gap between human cohorts and mouse models due to similar anatomy, physiology, life-span, and size between pigs and humans. These models provide the opportunity to advance medical imaging while simultaneously characterizing progressive changes resulting from an intervention, exposure, or genetic modification. We present a foundation for effectively characterizing disease models in pigs, susceptible to tumor development, using longitudinal medical image acquisition and post-processing techniques for quantification of disease.

Longitudinal, whole-body protocols were developed with CT and MRI. Focus was placed on systematic process, including transportation, anesthesia and positioning, imaging, and environmental controls. Demonstration of the methodology was achieved with six pigs (30-85 kg) with four to seven imaging time points acquired per animal. Consistent positioning across time points (CT to CT) and within time points (CT to MRI) was assessed with distance measures obtained from the skeleton following rigid registration between images. Alignment across time points was achieved with an average value of 16.51 ($\pm$ 12.46) mm observed all acquired measurements. For consistent, retrievable, and complete qualitative assessment of acquired images, structured reports were developed, including assessment of imaging quality and emphasis on tumor development throughout the body. Reports were used to perform a systematic, semi-

qualitative comparison of CT and MRI lung assessment with an overall agreement of 72% in detection of disease indicators.

A multi-level registration algorithm was developed to align anatomic structures of interest in the acquired longitudinal datasets. The algorithm consisted of initialization followed by repeated application of a core registration framework as the input data reduced in image field of view. It was applied to align regions of interest in the brain, upper right lung, and right kidney. Validation was performed with overlap (range = [0.0,1.0], complete overlap = 1) and distance measures (range = [0.0, ∞], perfect match = 0.0) of corresponding segmentations with overall results of 0.85 (± 0.11) and 0.41 (± 0.83) mm, respectively. An extension of the algorithm was created, demonstrating the ability to incorporate directional growth and feature extraction measurements into longitudinal tumor progression monitoring. Techniques were applied to a phantom dataset showing solid tumor growth and transition from a non-solid to part-solid lesion in the lungs.

Finally, the developed methods – imaging, structured reporting, registration, and longitudinal feature extraction – were applied to four different porcine models pre-disposed to tumor development. 1) A genetically modified Li-Fraumeni ($TP53^{R167H/+}$/$TP53^{R167H/R167H}$) background model showing the development of osteosarcoma and lymphoma. 2) A $TP53^{R167H/+}$ animal with exposure to crystalline silica showing progression of silicosis in the lungs. 3) $TP53^{R167H/+}$/$TP53^{R167H/R167H}$ animals with exposure to radiation for targeted sarcoma development and 4) $TP53^{R167H/+}$ pigs with conditional $KRAS^{G12D/+}$ mutation activated in the lung and pancreas. Whole-body and targeted imaging protocols were developed for each model and qualitatively interpreted by a radiologist using structured reports. Multi-level registration was used to align identified tumors and longitudinal features were extracted to quantitatively track change over time. Overall, the developed methods aided in the effective, non-invasive characterization of these animals.

PUBLIC ABSTRACT

Cancer is the second deadliest disease in the United States with an estimated 1.69 million new cases in 2017. Medical imaging systems are widely used in clinical medicine to non-invasively identify, diagnosis, plan treatment, and monitor tumors within the body. Advances in imaging research related to cancer assessment have largely relied on consented human patients, often including varied populations and treatments. Tumor bearing mouse models have been highly valued for basic science research, but imaging focused applications are limited by the direct application of developed techniques. Pig models are well suited to bridge the gap between human patients and mouse models due to their biological similarly to humans. These models will allow researchers to methodically cross compare state of the art medical imaging procedure related to the early detection, diagnosis, monitoring, and treatment planning of cancer with direct application to clinical medicine.

In this thesis, we have developed methods for longitudinal tracking of disease development in four tumor prone pig models using current clinical method imaging systems, computed tomography (CT) and magnetic resonance imaging (MRI).

Following image acquisition, a reporting system was constructed for consistent, visual interpretation of images, image alignment was performed on identified tumors, and imaging characteristics were automatically extracted from tumors. Methods were applied to tumor prone pigs with additional exposure to known cancer causing agents. Detected cancers included bone and kidney tumors and lymphoma, and anticipated development of lung and pancreatic tumors.

TABLE OF CONTENTS

LIST OF TABLES

LIST OF FIGURES

xiii

CHAPTER 1: INTRODUCTION

Medical imaging technology has made great advances in the last thirty years becoming a key clinical tool for the non-invasive assessment of human disease. A study published in 2010 reported an estimated number of imaging procedures ranging from 12 to 23 per patient diagnosed with a wide range of cancers within two years of diagnosis with increasing trends seen over a 6 year period [1]. In general, imaging related to cancer has been used for screening programs to detect tumors early in high risk, non-symptomatic patients and for staging of cancer to identify the extent of disease and aid treatment planning. In addition, repeated imaging is used to longitudinally evaluate cancer following intervention with developed metrics to quantify tumor burden at each imaging time point. Post-acquisition, image processing algorithms have been developed for several applications including tumor segmentation, multi-modal fusion, and exploration of image biomarkers in cancer identification.

Medical imaging research related to detection, diagnosis and monitoring of tumors has relied largely on consented human patients and/or small animal models as research subjects. However, limitations exist in utilizing human patients, including varied populations, stages, comorbidities and treatment strategies. In mouse models, disparities exist in the technical capabilities of micro-imaging systems compared to equivalent clinical imaging systems, limiting their translational ability with regards to medical image protocols and data analysis. Pig models have emerged as surrogates for human disease due to their similar anatomy, physiology, life-span, and size to humans, bridging the gap between the small animal model and the human cohort. Pig models provide the opportunity to advance medical imaging while simultaneously characterizing progressive changes in the model that result from an intervention, exposure, or genetic modification. Specifically, repeated imaging of these models facilitates clinically translatable investigation of disease precursors, initiation, progression, and treatment response while providing a longitudinal database for post-acquisition processing development. Therefore, the goals of this research are to lay the foundation for effectively characterizing disease models in pigs using medical imaging techniques and developing longitudinal post-acquisition processes for quantification of disease.

1.1 Specific aims

To provide disease characterization in porcine models as surrogates of human disease, we propose three aims:

Aim 1: Develop imaging protocols for the characterization of the phenotype to genotype relationship in novel porcine disease models. Multi-modality imaging methods developed for whole-body, longitudinal disease screening of porcine disease models are presented in CHAPTER 3: LONGITUDINAL MEDICAL IMAGE ACQUISITION. These methods include several important considerations across a wide variety of disease models, including transportation, anesthesia, positioning, and environmental controls.

Aim 2: Develop longitudinal post-acquisition image analysis methods for monitoring disease progression. Developed post-acquisition methods were separated into three areas of focus.

1. Custom structured reporting methods for systematic qualitative assessment of disease are presented in CHAPTER 4: STRUCTURED REPORTING.
2. A multi-level registration algorithm for alignment of whole-body, longitudinal datasets is presented in CHAPTER 5: MULTI-LEVEL REGISTRATION.
3. Longitudinal feature extraction to assess directional growth and regional matching is presented in CHAPTER 6: LONGITUDINAL FEATURE EXTRACTION.

Aim 3: Utilize the developed medical imaging techniques to characterize tumorigenesis in a variety of genetically modified, cancer prone pig models. Our developed methods were applied to four different animal models. Generation of characterized models was focused on tumor development with emphasis in the lungs.

1. A Li-Fraumeni heterozygote and homozygote base model is characterized in CHAPTER 7: LI-FRAUMENI.
2. Extension of this model with additional crystalline silica exposure in the lungs is presented in CHAPTER 8: CRYSTALLINE SILICA EXPOSURE MODEL.
3. The Li-Fraumeni model with additional radiation exposure in the hind legs is presented in CHAPTER 9: RADIATION EXPOSURE MODEL.
4. Additional conditional activation of genetic modifications to the *KRAS* oncogene in the lungs and pancreas in the Li-Fraumeni model is presented in CHAPTER 10: CONDITIONALLY ACTIVATED KRAS MODEL.

CHAPTER 2: BACKGROUND AND SIGNIFICANCE

2.1 Medical imaging

Medical imaging has been widely used to aid in the diagnosis and evaluation of human cancers with greater benefits and applications as technology advances [2]. Due to its ability to assess physiologic structure and function, medical imaging can non-invasively assist in the detection, diagnosis and staging, and monitoring progression of tumor development. Given these advantages, medical imaging is continually being advanced for utilization in cancer management ranging from disease screening to evaluating progression.

There are five main imaging modalities used in cancer management: x-ray and computed tomography (CT), magnetic resonance imaging (MRI), positron emission tomography (PET), and ultrasound. In this work, we focus on the use of CT and MRI with future expansion to include PET.

Computed tomography: CT uses x-ray technology to create a three-dimensional (volumetric) image of anatomy in the body. As x-rays pass through the body, they are attenuated depending on the tissues they interact with and their corresponding densities. The resulting image is then a density map of the anatomy with standardized voxel units of Hounsfield (HU), such that -1000 HU corresponds to the density of air and 0 HU to the density of water. It is widely used for clinical assessment due to its wide availability, fast scanning times, and high resolution capabilities. The major drawback of CT is the use of ionizing radiation, measured by radiation dose in milli-Gray (mGy). Significant research has focused on the acquisition of high quality images with low-dose protocols. These have included the use of tube current modulation [3, 4] and iterative reconstruction (IR) [5-7].

CT and x-ray technology are widely used in screening for early cancer detection. These screening programs involve imaging high risk patients at recommended intervals as a precautionary measure to detect cancer early. Biennial mammography, using traditional x-ray, for breast cancer screening has been recommended since 2009 [8]. Similarly, in 2014 the United States Preventative Services Task Force recommended annual screening to lung cancer with low-dose CT [9]. The National Lung Screening Trial (NLST) has shown a 20% reduction in mortality through early detection of lung cancer [10] while various mammography studies have shown a

9% to 32% reduction in mortality due to breast cancer [8]. In 2016, CT was added to the potential tests in screening for colorectal cancer [11] with studies showing the potential for added benefit due to incidental findings in the widened imaging field of view compared to traditional colonoscopy [12].

Magnetic resonance imaging: MRI is also a tomographic imaging modality that uses magnetic pulses to interrogate and obtain an image from different tissue properties. In traditional MRI, the detected signal is due to the relaxation of hydrogen atoms, called protons, back into alignment with a constantly applied magnetic field. The resulting image is then a map of protons corresponding to the specific relaxation property depending on the parameters of the acquisition protocol. The intensity of each voxel is dependent on the strength of the detected relaxation signal proportional to the size of the voxel and proton density of the tissues. Because of this, MRI excels at soft tissue contrast and does not required the use of ionizing radiation; however, there is typically a balance between acquisition time and quality of the image, specifically with respect to voxel resolution.

The invention of MRI arose from the desire to detect signal differences between malignant and benign tissues as reported with nuclear magnetic resonance (NMR) [13, 14]. Since then, it has been used in cancer imaging making use of its functional imaging capabilities, particularly in the brain and soft tissues. It has also been investigated as a tool for breast cancer screening in patients with increased susceptibility supplemental to traditional mammography [15].

Functional imaging: Several functional protocols have been developed to detect and predict malignancy. In CT, perfusion imaging has shown different values between malignant and benign process potentially identifying increased angiogenesis within in the tissue [16, 17]. MRI has also used perfusion imaging to characterize blood flow through tumors [18, 19]. These techniques involve injecting a contrast agent into the blood stream followed by repeated imaging to observe enhancement and clearance patterns in tissue. Diffusion weighted imaging (DWI) has also been used in MRI for differentiation of tissue. DWI measures the random diffusion of water molecules with the idea that less water diffusion occurs in tumors compared to surrounding tissue due to the extra structure [20]. Frequently, more than one MRI protocol is used for full characterization of tissues.

While CT and MRI are used to assess anatomic structure with functional capabilities, PET imaging is a purely functional imaging modality. Images are obtained using a radioactive

compound, known as a radiotracer, which mimics a chemical compound frequently used in the body and decays. This decaying produces positrons that are detected by the scanner such that areas of high uptake of the tracer contain more signal than areas of low uptake. The most common radiotracer used in cancer imaging is F18-fluorodeoxyglucose (FDG) and mimics glucose, detecting areas of high metabolism, i.e. malignant processes [21]. Similarly, F18-fluorodeoxythymidine (FLT) is an additional radiotracer that mimics thymidine used in DNA replication and is used to detect areas of high cell proliferation [22].

Typically, PET is combined with CT or MRI to acquire simultaneous anatomic information and is most often used for staging of disease [23]. The combination of anatomical and functional modalities is crucial in identifying the extent of disease stratified into a specified stage, I through IV, based on three criteria: the size of the primary tumor (T), the extent of lymph node involvement (N), and the level of metastasis that has occurred (M) [24]. This TNM staging describes the severity of the cancer, disease prognosis, and directs treatment options with recommendations based on the type of cancer. In general, stage I and II cancers describe localized extent with minimal or local lymph node involvement. Stage III involves greater involvement farther from the primary location and stage IV describes the most involved cancer with metastasis to other organs.

2.2 Imaging biomarkers

Following image acquisition, many image processing algorithms have been developed to enhance access and quantification of the information contained within acquired images. At a basic level, thresholding is used during viewing of the images to specify a range of intensities providing adaptable contrast surrounding a desired structure; a process known as windowing. Automatic tumor identification and segmentation algorithms have been developed to isolate tumors from surrounding tissue for a variety of applications including surgery planning [25-28]. In general, segmentation of tumors is useful for the delineation from surrounding tissues followed by additional analysis, such as feature extraction. Registration has also been utilized as a stepping stone to further analysis, including multi-modal fusion and radiation treatment planning [29-31]. Overall, these developed algorithms have aided clinicians in gaining further insight into disease and how to proceed with treatment. In this work, we focus on the development of algorithms applied to longitudinal datasets, including image registration and feature extraction.

Clinical criteria: Several quantitative markers have been developed to assess the progression of disease or tumor burden at each imaging time point. The most notable of these

measures are the World Health Organization (WHO) bi-dimensional measure [32] and the response evaluation criteria in solid tumors (RECIST) uni-dimensional measure – the current clinical standard [33, 34]. RECIST measurements include the largest diameter (in an axial image) of a specified number of tumors detected using CT and/or MRI. The overall tumor burden is compared across imaging and a progression outcome is determined: complete response, partial response, stable response, or disease progression. Limitations of RECIST include the varied reproducibility of measurements among radiologists leading to misclassification rates, concern over the use of a single, axial measurement as the representative criterion for a volumetric shape, and the growing use of targeted cancer therapies which may not follow the same traditional response pattern of progressive volume reduction [35].

In an attempt to overcome the limitations of the RECIST, focus has been placed on volumetric analysis of estimated tumor burden over time [36, 37]. With the advent of many automatic segmentation algorithms, tumor volume is a more objective, quantitative measure that takes advantage of the three-dimensional nature of medical imaging. This type of analysis has shown promise as a better predictor of overall survival in lung cancer [38, 39] and liver cancer [40].

Image registration: Image registration is an image processing technique that aligns two medical images into the same image space. Generally, an algorithm is comprised of four main components: an interpolator, an optimizer, a transform, and a similarity metric. With these elements, a moving image is iteratively transformed into alignment with the fixed image until a good match is found, defined by the similarity metric. Transforms are classified into rigid and non-rigid depending on the global or local deformation allowed during alignment. Goodness of a match is determined with three main similarity metrics: sum of squared differences and normalization correlation coefficient primarily applied to monomodal registrations and mutual information most widely used for multimodal applications.

Several registration algorithms have been developed aimed at tracking changes in tumor volume over time. Several algorithms have been focused on brain [41, 42], breast [43-45], and lung tumors [31]. In these instances, the results are used to infer information about tumor change. Additional work has extended the application to facilitate classification and targeted treatment planning to assess normal tissue and tumor tissue in liver cancer patients [46].

Imaging biomarkers: Of increased interest is the detection of imaging biomarkers as indicators of malignancy, treatment response, and overall survival. Several have already been

6

mentioned in this chapter, including functional imaging techniques and response criteria. With the implementation of several screening programs, computer-aided diagnostic (CAD) algorithms are being developed to evaluate risk of malignancy in identified lesions and aid physicians with clinical decision making. These algorithms are aimed at reducing invasive follow up procedures in those with benign lesions and selection of optimal diagnostic/therapeutic approaches for those with malignant lesions. In general, interrogation of intensities corresponding to detected lesions through feature extraction is performed followed by feature reduction and classification to identify features of interest [47]. A significant number of algorithms have been developed for breast and lung cancer [48, 49].

A limitation of the current tumor assessment criteria, including volume, is a lack of ability to detect variability in tissue types within a single tumor. Radiomics attempts to address this by extracting an extensive number of quantitative imaging features, similar to CAD, such as, shape, border, and texture features, and correlating them with non-imaging factors, like genetics and treatment strategies, as predictors of outcomes [50, 51]. Features are typically extracted from the entire tumor volume, isolated via segmentation; however, these principles may be applied on a cross-sectional basis or by stratification of intensities in order to obtain information about tumor heterogeneity [52].

2.3 Animal models

Ideally, advancements in cancer imaging, acquisition and processing, would involve in-vivo disease processes; however, there are difficulties when studying human subject cohorts [53]. These include variability in cancer subtypes, disease stage, lack of control over clinical treatment approaches, complications due to co-morbidities, and limited access to end-point data such as mortality and complete bio-specimens for pathological confirmation. From a psychological stand-point, recruiting patients is also difficult due to the need for extra non-diagnostic imaging, potentially increasing radiation exposure, and time commitment that adds additional burden to the patient.

Small animal models have been developed to overcome several of these limitations and have been crucial in advancing understanding cancer biology and treatment development. These have included genetically modified mouse models in an attempt to replicate the genetic make-up of cancers. However, translation from mice to humans has limitations due to significant disparities in size, anatomy, physiology, metabolism, and genetics. Micro-imaging modalities,

7

based on the same principles of clinical modalities, have emerged to provide greater insight into these models. These developments have provided a greater comprehensive longitudinal understanding of small animal exposure studies [54]; however, translatability of protocols is limited due to differing capabilities between micro-modalities and clinical modalities [55]. In addition, large size disparities between small animal models and humans limit the ability for protocol development with clinical modalities.

Cancers found in humans are complex, genetic diseases, something that is difficult to mimic with mouse models, leading to the exploration to more complex genetic animal models. Pigs have previously been used as biomedical models showing similar anatomy, pharmacokinetics, and size to humans [56-59]. Additionally, pigs have a more complex genetic background with technologies allowing for genetic manipulation in these animals [60]. These advantages present a promising background from which to develop cancer models that better reflect the human disease process providing a bridge between small animal models and human cohorts.

Several groups have developed genetically modified pig models. One group has focused on the development of a colorectal cancer model showing progression to tumor, monitored with regular colonoscopies [61]. Several groups, including our own group, have focused on the generation of *TP53* tumor suppressor mutant models with conditional activation [62] and germline mutations [63]. Conditional activation has also been explored for a *KRAS* oncogene mutant model [64] and a *KRAS/TP53* mutant model [65]. Other models have been generated and are reported in Watson, et al. [60] and Flisikowska, et al. [66]. The development of these models provides the opportunity to advance disease detection, diagnosis, and treatment while simultaneously employing and validating standard and novel medical imaging techniques.

2.4 Significance

Porcine cancer models present the opportunity to overcome several issues in critical care for cancer patients by serving as controlled surrogates to refine imaging protocols. Their comparable size allows for use of clinical imaging modalities providing direct translational capabilities. Pigs have previously been utilized for the development and translation of quantitative CT imaging characterization of human emphysema [67-69]. At a fundamental level, medical imaging can be used for the genotype to phenotype characterization of new models.

During this process, systematic screening protocols may be established with focus placed on early detection of tumors.

With growing access to medical imaging modalities, it is important to identify and justify the added benefit of specific imaging procedures. Pig models present the opportunity to conduct large cross-comparison studies with large datasets obtained from the same cohort of animals studied with multiple modalities and protocols. This provides tightly controlled studies for direct comparison and optimization of imaging protocols overcoming several limitations with human cohorts, including varied populations and patient concern. Examples of direct benefit include use of low dose CT, optimization of contrast enhanced protocol parameters for optimal scanning time, and verification of new PET radiotracers.

Pigs also have a long lifespan (15-20 years) allowing for continued characterization of disease though longitudinal imaging with readily available access to diseased tissue upon necropsy for confirmation of disease using histopathology. The repeated use of animals for imaging allows for study design with small populations. This allows for a better understanding of both temporal and spatial extent of disease with direct correlation between imaging and histopathology; important for identification and verification of imaging biomarkers sensitive not only to malignant/benign characteristics across tumors, but also within tumor heterogeneity.

Beyond protocol development, medical imaging is also used to monitor cancer progression over time. These models can be used where human models cannot, including unrestricted growth of cancer in the absence of treatment. Progression may also be monitored following systematic treatment strategies to identify and locate biomarkers of treatment response. In this instance, porcine models may act as an intermediary between basic science cancer research in mouse models and clinical trials. Lastly, imaging is essential in planning clinical interventions. The similar size and anatomy of pigs make these models ideal for testing new, advanced surgical techniques and approaches for stereotactic radiation treatment with confirmation of complete destruction and removal of all tumor cells.

CHAPTER 3: LONGITUDINAL MEDICAL IMAGE ACQUISITION

3.1 Introduction

Medical imaging is a rapidly advancing field enabling the repeated, non-invasive assessment of physiologic structure and function. As a clinical imaging modality, CT has a fast acquisition time, moderate cost, and superior structural resolution while MRI involves no ionizing radiation and has excellent soft tissue contrast. These modalities provide the opportunity to non-invasively characterize and compare progressive changes in pigs that can result from an intervention, exposure, or genetic manipulation. Longitudinal monitoring within the same animal can provide valuable information about the etiology of disease while also keeping the number of animals needed for a study to a minimum.

Animal models have been relied upon in medical research to develop and validate technological and/or procedural methods for translation to humans. Specifically, pig models can serve as a valuable human surrogate in imaging studies due to their similar anatomy, physiology, life-span, and size to humans [58, 59]. This allows for testing and validation of novel imaging methods on clinical imaging systems with direct comparison between multiple modalities, a feat that is challenging to accomplish in humans. Qualitative and quantitative interpretation of medical images is dependent on compromises made between acquisition parameters (i.e. radiation dose or acquisition time) and resultant image quality. Image quality is affected by internal factors, including noise, artifact, and contrast resolution [70], and external factors, such as growth of the subject, and consistent, whole-body positioning [71]. These factors are important when seeking to detect and measure change in biological structure and/or function over time, as is used to track disease development and treatment response. In previous small animal studies, these varying external factors have been accounted for by the development of imaging protocols to acquire uniform images in the presence of respiratory motion [37] and use of external positioning units to ensure consistency in positioning using multiple imaging modalities [72].

This chapter describes the development and testing of methods for the acquisition of longitudinal medical images for disease monitoring in porcine disease models to determine the genotype to phenotype relationship. In this work, we present modification of clinically relevant medical image acquisition protocols adapted to accommodate longitudinal positioning of a sedated pig. A genetically modified Yucatan miniature pig model with Li-Fraumeni syndrome

was developed by Exemplar Genetics (Sioux Center, Iowa). Prone to the development of a wide variety of tumors, a cohort of animals was utilized for longitudinal, multi-modality protocol development. Further characterization of this model is described in CHAPTER 7: LI-FRAUMENI.

3.2 Materials and methods

To facilitate longitudinal imaging of pigs, a variety of factors were taken into consideration during protocol development. Different model phenotypes present different ranges of potential impairments; therefore, it was important to ensure minimal stress was placed on the animal during each screening time point. In addition, minimal exposure to potential health hazards, such as airborne transmittable disease, was considered in the design process with placement of environmental controls. In choosing imaging modalities, access to facilities and transportation of the animal were important to consider as well as the strengths and limitations of each modality. Another consideration included consistent positioning of the animal during data acquisition, including between modalities and between imaging time points. This was important to support the application of image processing techniques reported in CHAPTER 5: MULTI-LEVEL REGISTRATION and CHAPTER 6: LONGITUDINAL FEATURE EXTRACTION. Lastly, full recovery of the animal at the end of each screening required a minimally invasive procedure. In-house equipment was engineered and image protocols were chosen to develop repeatable methods that provided high quality diagnostic images while taking in account these limitations.

Animal Preparation: All procedures were performed under anesthesia, induced with an intramuscular injection mixture of telazol (2.2 mg/kg), ketamine (1.1 mg/kg), and xylazine (1.1 mg/kg) and maintained with 0.5 – 5% isoflurane. All animals were mechanically ventilated through tracheal intubation with an appropriate sized balloon cuffed endotracheal tube. Ventilation was performed with 5 cm H_2O positive end expiratory pressure (PEEP) (ACCU-PEEP Valve, Cascade Healthcare Solutions, Renton, WA, USA) and an approximate tidal volume of 10 mL/kg. The ventilation protocol used a respiratory rate of 10-16 breaths per minute to maintain an end-tidal carbon dioxide pressure (ET-CO_2) between 35 and 45 mmHg and a blood oxygen saturation pressure (SpO_2) of 98-100%. Peripheral intravenous (IV) access was obtained via ear vein cannula (20G) for the administration of contrast and was maintained using heparinized saline (3-5ml, 500 units/L) flushes.

Physiologic monitoring was maintained through the duration of each animal imaging study: in CT with a Phillips physiologic monitor (Intellivue MP90, Phillips Healthcare, Best, The Netherlands), in transit with a portable physiologic monitor (Propac Encore, Welch Allyn Inc., Skaneateles Falls, New York), and in MRI with a MRI compatible physiologic monitor (Invivo MAGNITUDE:3150M, Medeco, Boise, Idaho). All experimental procedures were approved by the Institutional Animal Care and Use Committees (IACUC) of the University of Iowa and Exemplar Genetics.
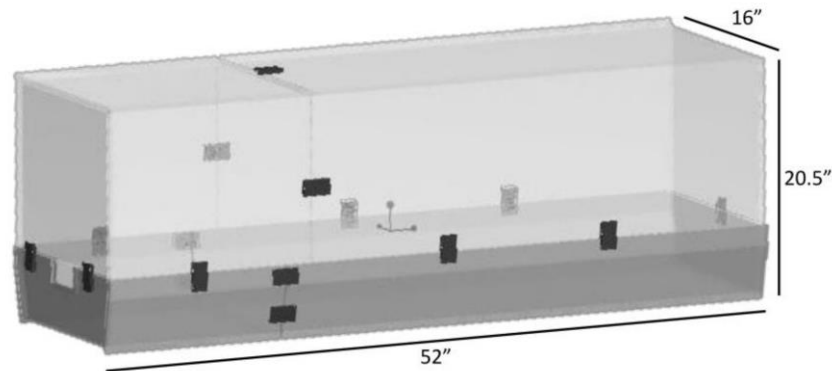
Figure 3-1: Consistent positioning unit. The computer aided design drawing of the positioning unit, with corresponding dimensions, illustrating four quadrants with corresponding latches and an opening for the port at the front of the unit.

Animal positioning: A positioning unit, designed by Samantha Dilger, illustrated in Figure 3-1, was designed to host the anesthetized animal during scanning and while in transit. With specific interest in CT and MRI, the completed unit was made from radiolucent and non-ferromagnetic materials with highly restrained hydrogen atoms to prevent MRI artifact. A modular design was implemented to allow for flexibility of MRI coil placement, easy access to the animal, and accommodation for varying bore sizes. Quadrants were made of ½-inch thick polycarbonate, chosen for its long list of desirable qualities, and properly aligned with polycarbonate pegs. Each quadrant was lined with 1/16-inch thick butyl rubber gasket and fastened together with polypropylene draw-style latches secured with nylon 6/6 machine screws to provide an air tight seal for environmental isolation during transit. Misalignment in the partitioning of the head quadrants was purposefully designed for greater overall support and an air-tight seal. Lastly, quadrants could be removed during imaging to allow for appropriate placement of a variety of MRI coils. A rubber diaphragm was designed to fit into a chamfered port placed in the bottom head quadrant to house tubing for ventilation to the animal, intravenous

access, and a one-way value to prevent pressure build up in the unit. Movement of the unit was performed with a nylon sleeve with wooden handles placed below the unit.

With interest in whole-body positioning, specifically organs of the head, thorax, and abdomen, animals were placed supine in the positioning unit for all imaging protocols and manually adjusted into alignment. The same positioning was maintained in MRI as the animal remained in the positioning unit during transit between modalities. Minimal differences included removal of the small base quadrant for placement of head coil in MRI and the front legs of the animal were extended out of the thoracic field of view in CT only. This allowed for optimal acquisition of CT datasets and accounted for the use of MRI surface coil placement on the abdomen and thorax.

To increase efficiency, an MRI compatible cart (240-100 MRI stretcher, Biodex Medical Systems, Shirley, New York) was used as a central location to place and transport the positioning unit. A custom developed aluminum mounting system was attached to the cart to hold a portable MRI compatible anesthesia ventilator (Primer XP MRI-Compatible Veterinary Anesthesia Ventilator, DRE Veterinary, Louisville, Kentucky) equipped for isoflurane administration for uninterrupted administration of anesthesia. A removable aluminum (non-ferromagnetic) tray was machined to fit directly above the wheels to store materials for MRI contrast administration, an oxygen tank for use during transit, and backup supplies.

Imaging protocols: Comprehensive, full-body screening protocols were developed to obtain optimal image phenotyping within an efficient research study time frame. CT was chosen for fast acquisition, high resolution, and quantitative imaging and MRI was selected for superior soft tissue contrast imaging without the use of ionizing radiation.

Computed Tomography: Whole-body image acquisition was performed with a series of head, chest, and abdominal protocols to assess structural detail and comprehensive disease development throughout the body. CT scans were obtained with a dual-source scanner (SOMATOM Definition Flash or SOMATOM Definition Force, Siemens Healthcare, Forchheim, Germany). Parameters for all CT scans are listed in Table 3-1. Thoracic scans were acquired at an inspiratory breath-hold of 20 cmH$_2$O PEEP (ACCU-PEEP Valve, Cascade Healthcare Solutions, Renton, WA, USA) following 2 minutes of pulmonary recruitment. Mouth pressure was monitored with in-house LabVIEW software (National Instruments, Austin, Texas) to confirm consistent inspiratory breath-holds during imaging. Cardiac gating was not used for any thoracic CT scans. Non-contrast and contrast-enhanced abdominal scans were also acquired at a 20

cmH$_2$O PEEP breath hold to minimize motion artifact due to breathing. Contrast-enhanced abdominal scans were acquired to enhance structural detail and obtained 70 seconds following continuous administration of 2 mL/kg of iodinated contrast (Isovue Multipack 370mg/ml, Bracco Diagnostics, Monroe Township, New Jersey) through the peripheral IV access at a rate of 4 mL/second. This protocol was modeled after the standard portal venous phase protocol for humans. Reconstruction of the head and body scans was performed with standard head and body reconstruction kernels, respectively, at 3 mm slice thickness for qualitative analysis and 0.75 mm slice thickness for quantitative CT analysis.

Table 3-1: CT Imaging Protocols. Parameters for CT imaging developed for a SOMATOM Definition Flash/Force dual-source scanner. Three main protocols were developed for the head, non-contrast chest, abdomen, and pelvis, and contrast-enhanced abdomen.

	Head	Non-contrast Chest/Abdomen/Pelvis		Contrast Abdomen	
Scanner	FLASH	FLASH	FORCE	FLASH	FORCE
Scan Type	Helical (SE)	Helical (SE)	Helical (SE)	Helical (SE)	Helical (SE)
Rotation time (s)	1.0	0.5	0.5	0.5	0.5
Det. Configuration	128 x 0.6	128 x 0.6	192 x 0.6	128 x 0.6	192 x 0.6
Eff. mAs	390	210	190	210	110
kV	120	120	120	120	120
Care Dose 4D	OFF	OFF	OFF	OFF	OFF
Pitch	0.55	1.0	1.0	0.6	1.0
Recon. Algorithm	H31	B35	Br40	B35	Bf40
Slice Thickness (mm)	3, 0.75	3, 0.75	3, 0.75	3, 0.75	3, 0.75
Scan time	< 10s	< 25s	< 5s	< 10s	< 5s
Breath hold	None	20 cm H$_2$O	20 cm H$_2$O	20 cm H$_2$O	20 cm H$_2$O

Magnetic Resonance Imaging: Comparable, whole-body imaging with MRI was performed using a series of scans of the head, chest, and abdomen. All MRI scans were acquired with a 3-Tesla MRI system (MAGNETOM TIM Trio 3T, Siemens Healthcare, Forchheim, Germany) with standard head and surface coils. Parameters for all MRI scans are listed in Table 3-2. A high-resolution brain scan to assess structural detail was performed using a T2 3D turbo spin echo with variable flip angle (SPACE) protocol. Subsequently, a diffusion tensor imaging (DTI) protocol was acquired to permit detailed analysis of the white matter. For the chest and abdomen, standard turbo spin echo T2-weighted scans acquired in the axial and coronal planes were used to assess areas of increased fluid content, such as metastatic tumors or areas of

inflammation. Respiratory navigation was performed to limit motion artifact during ventilation. A T1-weighted volume interpolated gradient echo (VIBE) contrast-enhanced abdominal sequence was acquired pre-contrast and 30, 60, and 180 seconds post IV administration of 0.2 mL/kg gadolinium MRI contrast agent. These scans were collected to incorporate functional analysis of blood flow through the liver and obtain greater anatomical detail in the abdomen. An additional post-contrast VIBE thoracic scan was acquired for increased anatomical detail in the lungs. Breath-holds of 25 seconds or less at an inspiratory pressure of 20 cm H_2O (ACCU-PEEP Valve, Cascade Healthcare Solutions, Renton, WA, USA) were used to reduce motion artifact for all VIBE scans. This MRI assessment was optimized after considering several pulse sequences including fluid attenuated inversion recovery (FLAIR), short tau inversion recovery (STIR), ultrafast 3D gradient echo (MP-RAGE), single-shot turbo spin echo (HASTE), and diffusion weighted imaging. Cardiac gating was not performed during any of the thoracic MRI scans.

Table 3-2: MRI protocols. Parameters for MRI imaging developed for a 3-Tesla TIM Trio scanner. Six main protocols were developed for focus on the brain, chest, and abdomen. Two sets, chest and abdomen, of T2 axial and coronal were acquired and a dynamic VIBE sequence acquired in the abdomen pre-contrast and 30, 60, and 180 seconds post-contrast resulting in a total of 11 scans.

	Head		Chest	Chest/Abdomen		Abdomen
	3D SPACE	**Axial DTI**	**Post-Contrast VIBE**	**T2 (Axial)**	**T2 (Coronal)**	**Dynamic VIBE**
Scanning sequence	Spin echo	Echo planar	Gradient echo	Spin echo	Spin echo	Gradient echo
Acquisition type	3D	2D	3D	3D	3D	3D
Repetition time (msec)	1630	2800	4.3	5285	5279	4.3
Echo time (msec)	119	83	1.92	156	157	1.92
Flip angle (º)	120	90	12	120	120	12
Echo train length	141	1	1	109	109	1
Slice thickness (mm)	0.9	5	3	5	5	3
In-plane resolution (mm)	0.9 x 1.1	1.5 x 1.5	1.0 x 1.8	1.4 x 1.8	1.5 x 2.0	1.0 x 1.8
Acquisition matrix	256 x 194	160x160	256 x 192	256 x 194	256 x 194	256 x 192
Number of Slices	96	12	72	48	40	72-80
Approx. Scan time (min:sec)	7:50	1:50	0:24	4:52	4:10	0:23
Respiratory management	None	None	Breath hold 20 cm H_2O	Navigator gating	Navigator gating	Breath hold 20 cm H_2O

Consistent positioning evaluation: Due to the desire to maintain consistent positioning, alignment of the skeleton and major internal organs in acquired images were evaluated using segmentation and rigid image registration. CT images from each imaging time point were registered with CT images obtained from the first time point for each animal to assess across time point alignment. MRI images were registered to CT images acquired in the same time point to assess within time point alignment. Registration was performed with a rigid and anisotropic scaling transform accommodating for simple translational and rotational alignment and growth of the animal, respectively. Initialization of the transform was performed by aligning the image centers of geometry and the mutual information metric formulized by Mattes, et al. was used to account for the use of multiple imaging modalities [73]. Additional metric initialization in all three axes was included for assessing positioning within time points between CT and MRI due to the disparities in anatomic fields of view. A comprehensive description of the registration framework and initialization methods is described in CHAPTER 5: MULTI-LEVEL REGISTRATION.

Positioning across time points was evaluated in CT images through quantitative measures using skeletal models generated through the methods shown in Figure 3-2. The skeleton of each animal was initially isolated in each non-contrast CT image with thresholding at voxel values above 200 HU. Morphological dilation was performed with a binary ball structuring element of radius one and connected areas of less than twenty thousand voxels were removed from the skeletal mask. A final mask was created with morphological erosion and manual inspection to remove non-skeletal areas that remained. Models of the skeleton were created using the model maker module in Slicer 3D [74, 75]. Visual alignment post-registration of skeletal models was observed and quantitative assessment was performed with eleven fiducial locations, obtained via single observer from each model corresponding to the sternum, scapulae, ribs, vertebrae, pelvis and legs. Three fiducials were acquired from a single observer at each of the eleven locations and averaged resulting in one fiducial per location. Locations were chosen to represent peripheral and central alignment, minimize segmentation error, and accommodate all fields of view. Misalignment was quantified by calculating the distances between corresponding fiducials from the first time point and all corresponding time points.

Positioning across modalities within each time point was performed through registration of CT and MRI acquisitions obtained with equivalent breath holds. Visual assessment was performed using checkerboard images to evaluate alignment of major internal organs. Lastly, preliminary quantification of skeletal growth was obtained via measurements of bone length of

the left femur and the sternum. Two measurements were made per bone with the digital calipers in 3D Slicer on the 3D skeletal models by a single observer and averaged for a final measurement. Change in growth was determined with difference measures between the first time point and all other time points. Similar measurements were obtained on the weight of the animal at each time point and compared to determine the relationship between skeletal growth and weight change.
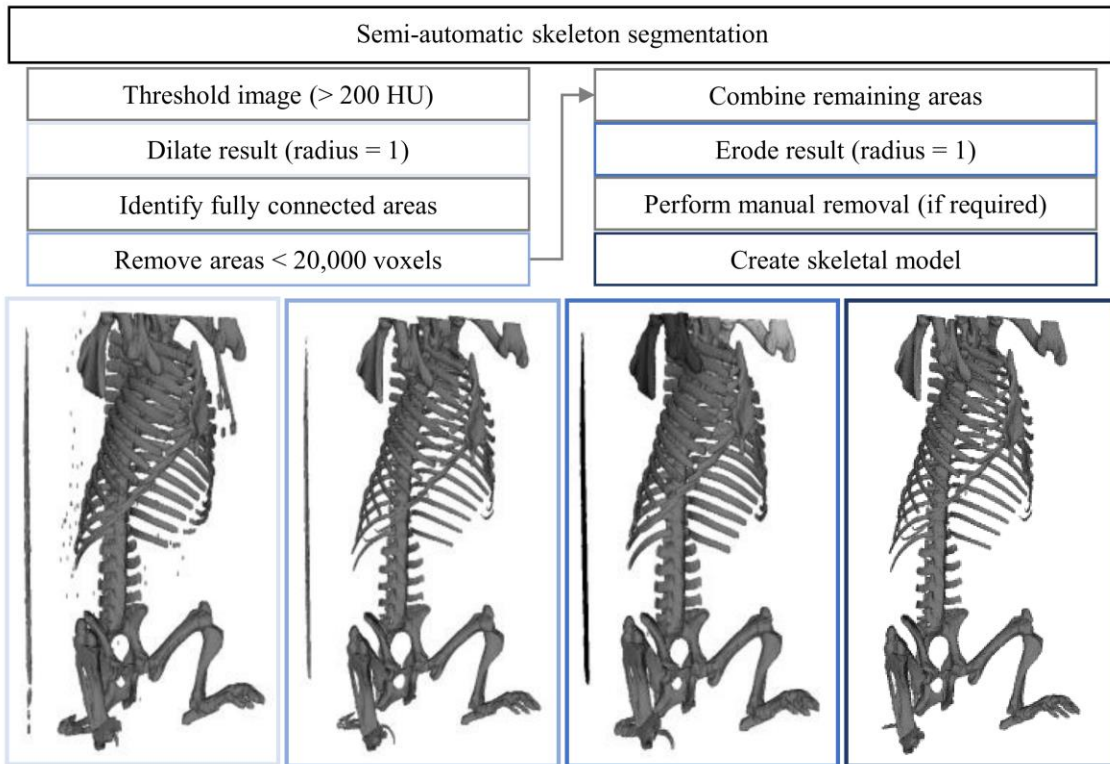
Figure 3-2: Creation of skeleton models. The methodology used to create skeletal models with examples of various steps displayed as an illustration of how the process is performed. The skeletal model used for fiducial placement was the result from the final step and is shown in the lower right corner of the figure.

Table 3-3: Longitudinal time points. The time points acquired for longitudinal imaging acquisition. Purple indicates that CT and MRI protocols were acquired, while blue indicates only CT protocols were acquired. Four wild type (WT) animals (A-D) were used for protocol development (PD). Subjects F-K were born at the end of September 2011 such that screening began at 12 months of age.

	2012									2013												2014												2015	2016			
Subject	A	M	J	J	A	S	O	N	D	J	F	M	A	M	J	J	A	S	O	N	D	J	F	M	A	M	J	J	A	S	O	N	D	J-D	J	F	M	A
WT A-D	PD																																					
F						X		X		X		X				X						X													X			
G						X		X		X		X				X						X																
H						X		X		X		X				X						X													X			
I						X		X		X		X				X						X								X								
J						X		X		X		X										X																
K								X		X		X										X																

17

3.3 Results

The designed, image-based monitoring procedure was applied to Yucatan miniature pigs between ages 10-52 months (30-85kg). Four wild type pigs were utilized to optimize and finalize CT and MRI protocols with respect to image quality and screening time. Six Li-Fraumeni animals were imaged repeatedly to longitudinally screen for tumor development using the finalized acquisition protocol. Of the initial six animals, one was replaced after the first time point due to an incidental medical condition. Imaging studies began at 12 months of age and occurred thereafter at 14, 16, 18, 21, 27, 36 and/or 51 months of age. CT was acquired at every imaging time points with MRI acquired at select time points as summarized in Table 3-3.
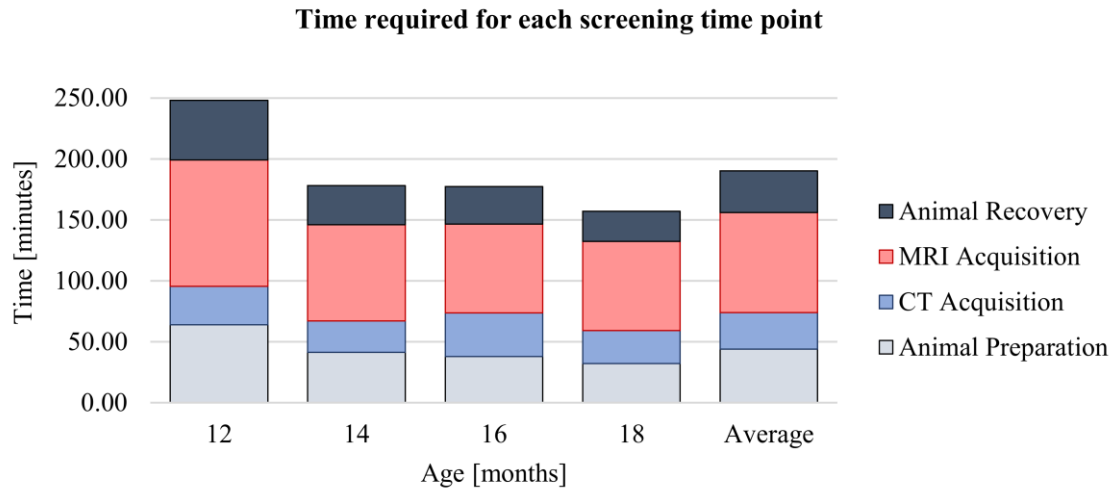
Figure 3-3: Time analysis of longitudinal studies. Graphical analysis of the time required the first four screening time points by age and overall average with a breakdown regarding animal preparation, recovery, and imaging time.

Time analysis was performed for the first four time points. The amount of time required for animal preparation, CT and MRI acquisition, and animal recovery was reported. CT imaging stayed relatively consistent with an average time of 30 ± 10 minutes with the most time required for animal alignment, breath-holds, and contrast injection. MRI required 82 ± 16 minutes to acquire all the protocols for full body acquisition with an imaging time of less than one hour and additional time required for equipment setup, positioning, and coil placement. Overall, the required time for each screening time point was an average of 201 ± 44 minutes with most of the variability seen in animal preparation and recovery. Increased efficiency can be seen through the four time points with an optimized average time of 165 minutes for time point 4 (18 months) as demonstrated in Figure 3-3.

Each imaging time point resulted in the 3 CT scans and 11 MRI scans per animal demonstrated in Figure 3-4, Figure 3-5, and Figure 3-6. Consistent inspiratory breath holds were achieved with an average of 20.19 ($\pm$ 1.54) cm H_2O PEEP for all thoracic and abdominal CT scans with the same PEEP value utilized in MRI. Consistent positioning assessment was focused on non-contrast, chest-abdomen-pelvis CT scans and breath-held chest and thoracic VIBE scans. CT scans were registered to the first acquired CT scan to evaluate positioning across time point. The final transforms showed minimal rotation (1.47 $\pm$ 1.28°), minimal translation (7.38 $\pm$ 17.18 mm) in all anatomical planes with the largest observed in the sagittal plane, and minimal scaling (1.03 $\pm$ 0.06) in all anatomical planes with the largest also observed in the sagittal plane. All skeletal models were successfully generated and aligned. Visual inspection showed the largest variations at the limbs, upper vertebral column, and upper sternum. Fiducials were obtained and differences were calculated between the first time point and all other time points. Quantitatively by fiducial location, illustrated in Figure 3-7, the largest skeletal deviations occurred at left knee with an average misalignment of 24.03 ($\pm$ 10.21) mm followed by the right knee at 19.31 ($\pm$ 11.59) mm. The smallest deviations were seen at the pubic symphysis joint with an average misalignment of 12.68 ($\pm$ 10.01) mm followed by the middle vertebrae at 13.89 ($\pm$ 7.61) mm.

Table 3-4: Consistent positioning by time point. The misalignment across time points calculated from all eleven fiducial locations showing the increased average error as the age of the animal increases.

Age at time point [months]	Age from first time point [months]	Average [mm]	Standard deviation [mm]	Minimum [mm]	Maximum [mm]
12	0	0.00	0.00	0.00	0.00
14	2	11.12	5.24	3.24	28.95
16	4	12.58	7.13	2.78	38.29
18	6	15.14	9.29	1.58	52.04
21	9	16.91	7.32	4.21	38.87
27	15	23.39	14.20	6.50	60.34
36	24	13.99	7.68	3.26	24.03
51	39	35.13	27.05	6.95	93.61

Observations across time points showed that misalignment increased as the difference in age of the animal increased. Error increased in a linear trend with average errors of 11.12 ($\pm$ 5.24) mm seen at 2 months from the first time point (14 months of age) to average errors of 35.13 ($\pm$ 27.05) mm seen at 39 months from the first time point (51 months of age). In comparison, maximum errors ranged from 28.95 mm to 93.61 mm at 2 months and 39 months from the first time point, respectively, as seen in Table 3-4. Overall, an average misalignment of 16.51 ($\pm$

12.46) mm occurred between all acquired measurements from all subjects at all measured locations.

VIBE pre-contrast abdominal and post-contrast chest MRI scans were registered to corresponding CT to assess within time point positioning. Visual evaluation of results focused on the internal alignment of organs and showed the presence of rotational changes about the sagittal plane, specifically in the alignment of the lungs. This is reflected in the resulting transforms with an average rotation of 1.94 ($\pm$ 2.16)^o required for the chest scans versus an average rotation of 1.63 ($\pm$ 1.45)^o required for the abdominal scans. Following initialization, minimal translation and scaling was required with an overall average translation of 1.8 ($\pm$ 5.13) mm and average scaling of 1.00 ($\pm$ 0.02). Demonstration of internal alignment is seen in Figure 3-8.

Final assessment of bone growth in the sternum versus the left long bone showed variable growth trends over time, irrespective of weight gain or loss. Animals weighed on average 45.20 ($\pm$ 10.66) kg at the first time point with a final weight of 63.17 $\pm$ 25.02 kg seen at their corresponding final time point, shown in Figure 3-9A. Average weight gain between the first time point and all other time points was 8.32 ($\pm$ 13.24) kg with a range of -11 kg to 44 kg. The sternum showed more aggressive growth rate across all time points compared to the femur which appeared to stabilize in growth around 27 months as observed in Figure 3-9B. Comparing measurements acquired from time point at 27 months, the sternum grew on average 16.84 ($\pm$ 5.71) mm versus a growth of 13.63 ($\pm$ 2.15) mm in the femur.
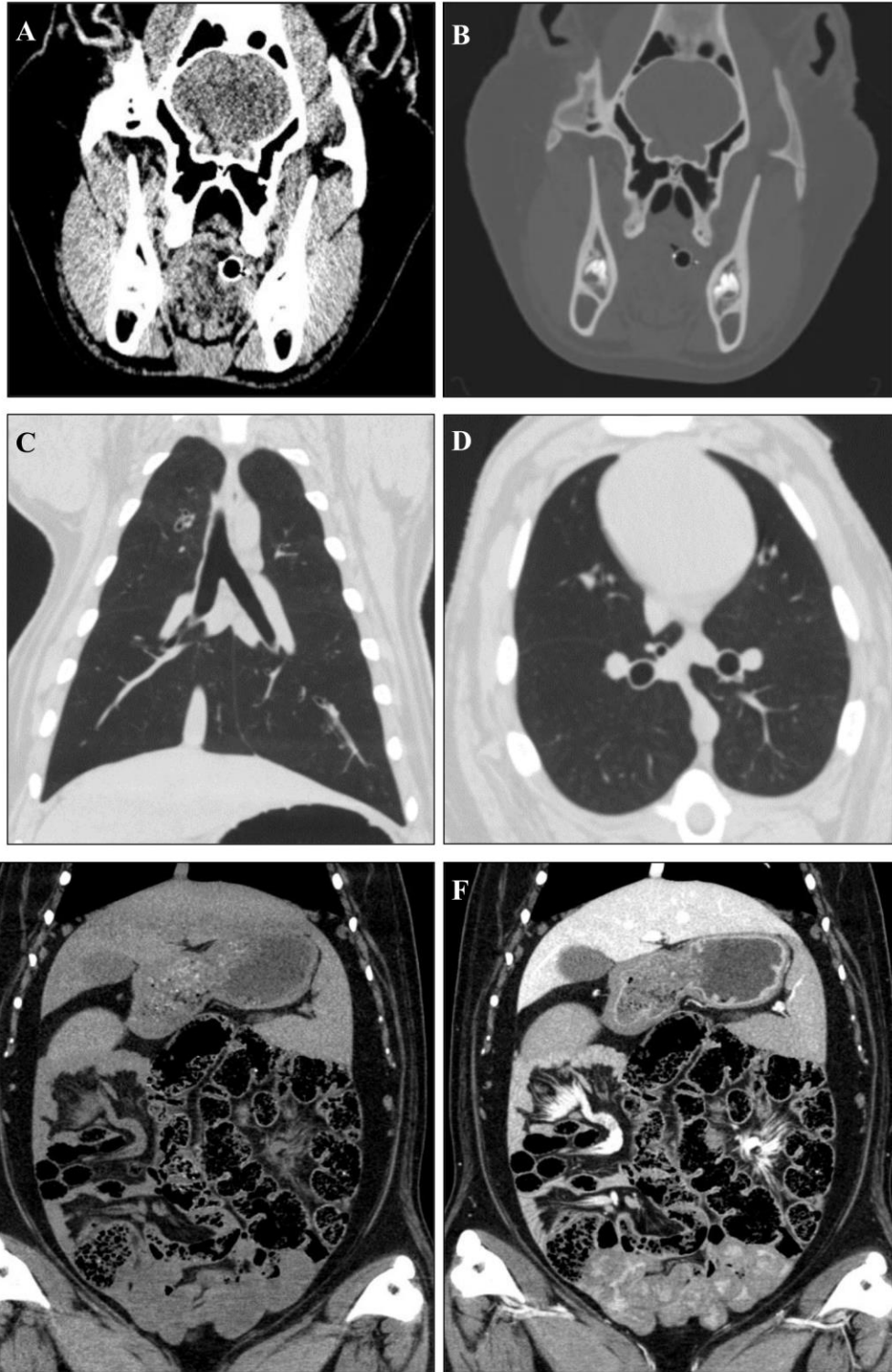
Figure 3-4: Acquired CT scans. Head scan in the (A) soft tissue (W:100, L:50) and (B) bone (W: 1000, L: 400) windows. The lungs focused on in the non-contrast chest, abdomen, and pelvis scan shown in a lung window (W: 1400, L: -500) in the (C) coronal and (D) axial anatomic planes. Abdominal anatomy from the (E) non-contrast chest, abdomen, and pelvis scan and the (F) contrast enhanced scan acquired 70 seconds post-injection shown in an abdominal window (W: 350, L: 40).
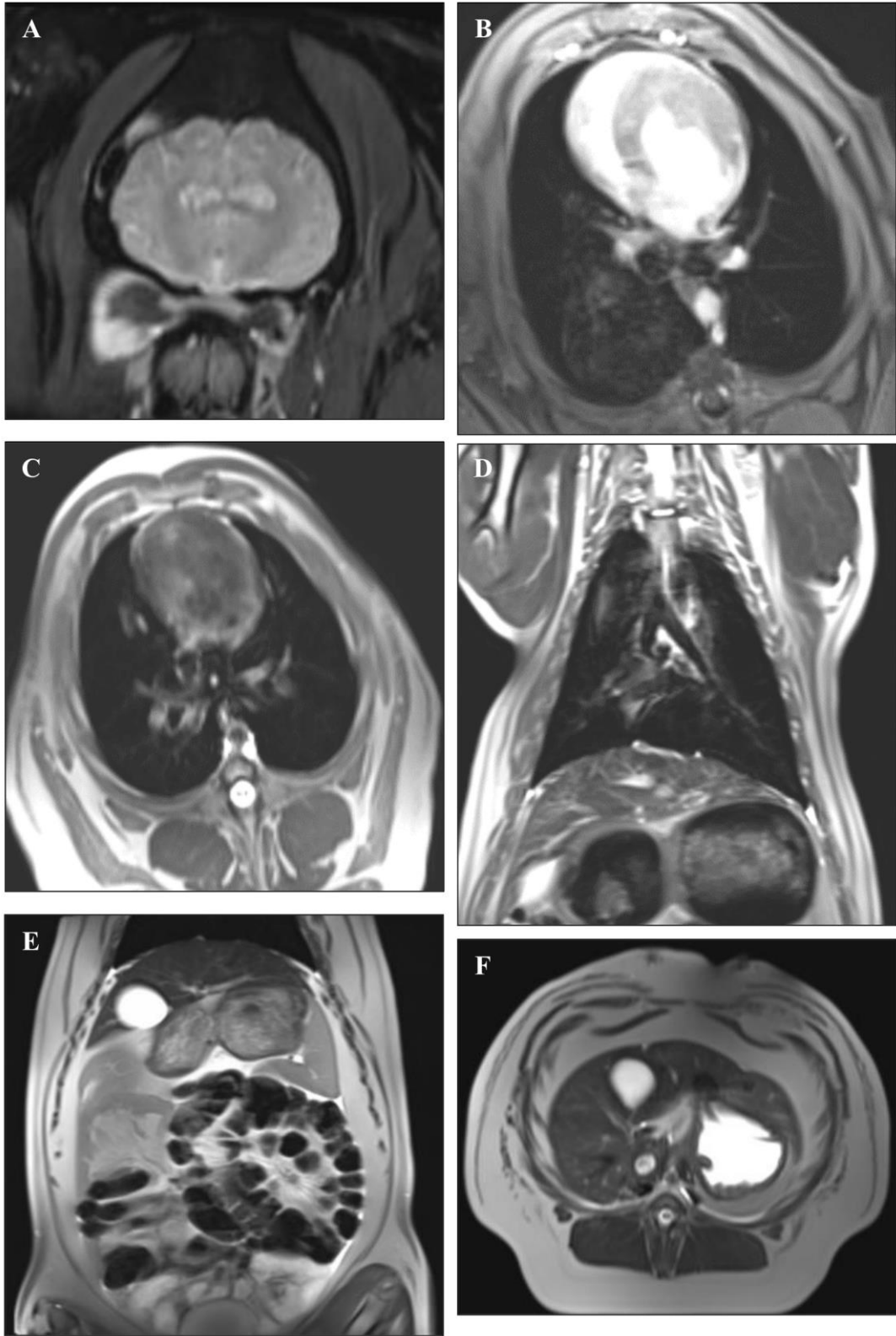
Figure 3-5: Acquired MRI scans. (A) 3D Axial SPACE scan of the brain. (B) Post-contrast VIBE scan of the thorax. (C) T2 axial and (D) coronal thoracic scans. (D) T2 axial and (F) coronal scans of the abdomen.
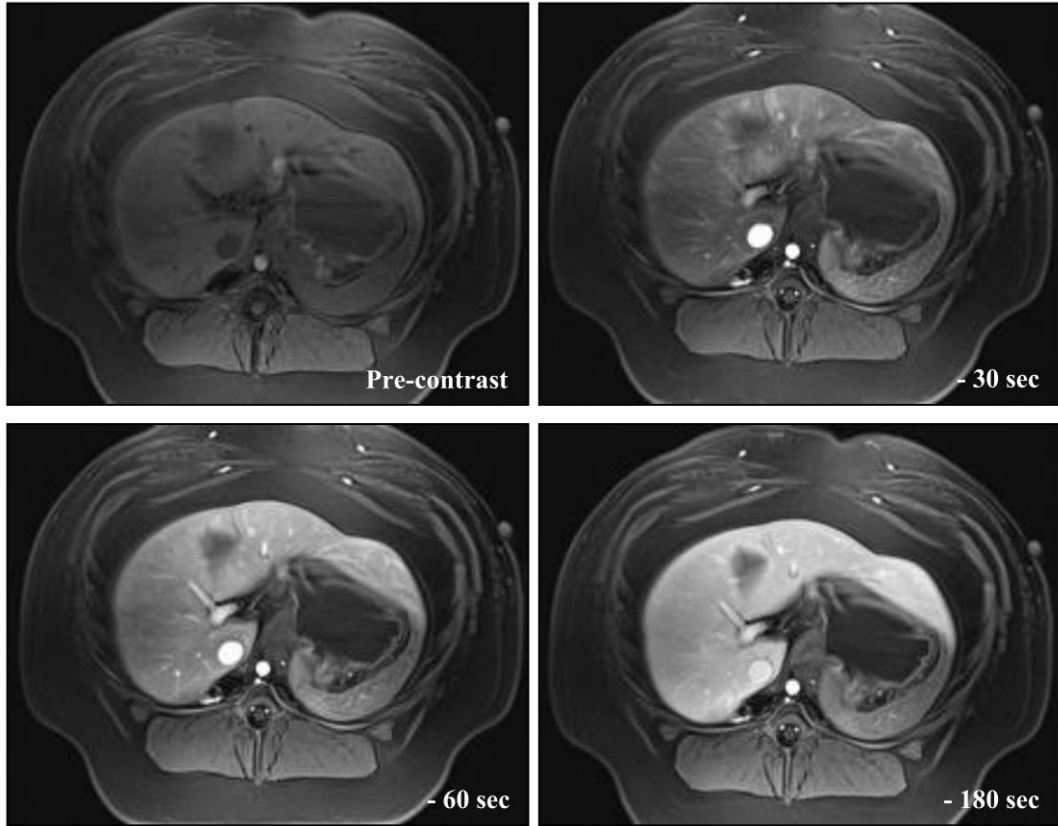
Figure 3-6: Acquired MRI scans. Contrast-enhanced VIBE sequence in the abdomen starting with the pre-contrast image, 30, 60, and 180 seconds post-contrast.
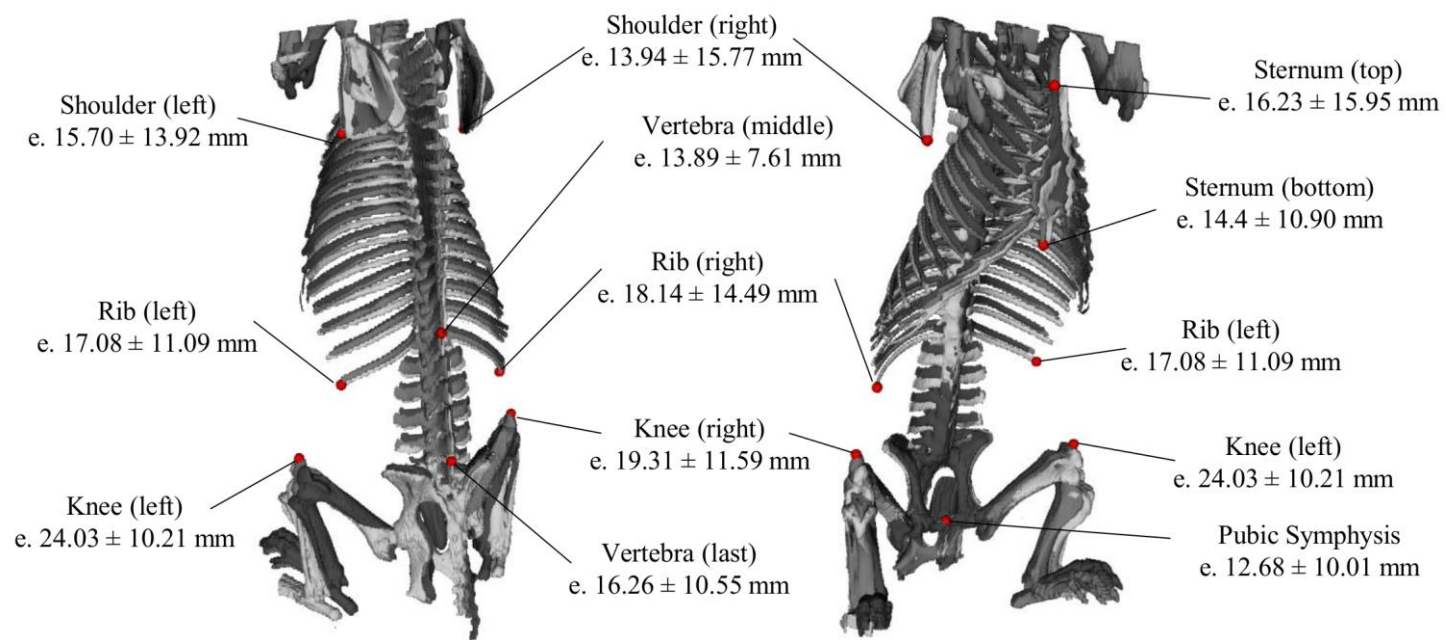
Figure 3-7: Consistent positioning by fiducial location. The aligned skeletal models at 12, 18, and 27 months of age (darkest to lightest) displaying visual and quantitative assessment of alignment. All measurements are reported as the average error between each time point and the first time point post-registration.
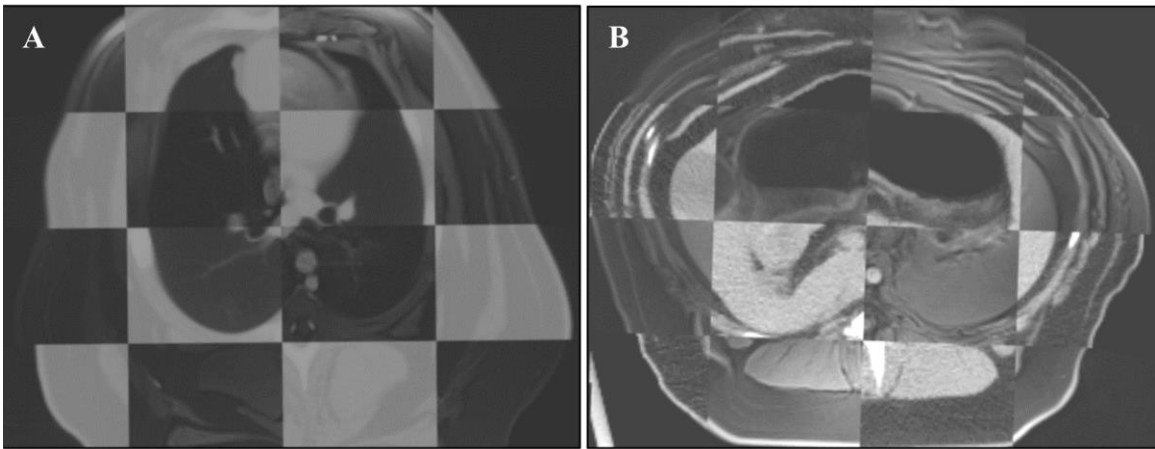
Figure 3-8: Consistent positioning within time points. Checkerboard images of aligned MRI and CT images demonstrating the internal alignment of internal structures. Images alternate beginning with MRI in the upper left corner.

A

Change in weight across time points

B

Bone growth rates across time points
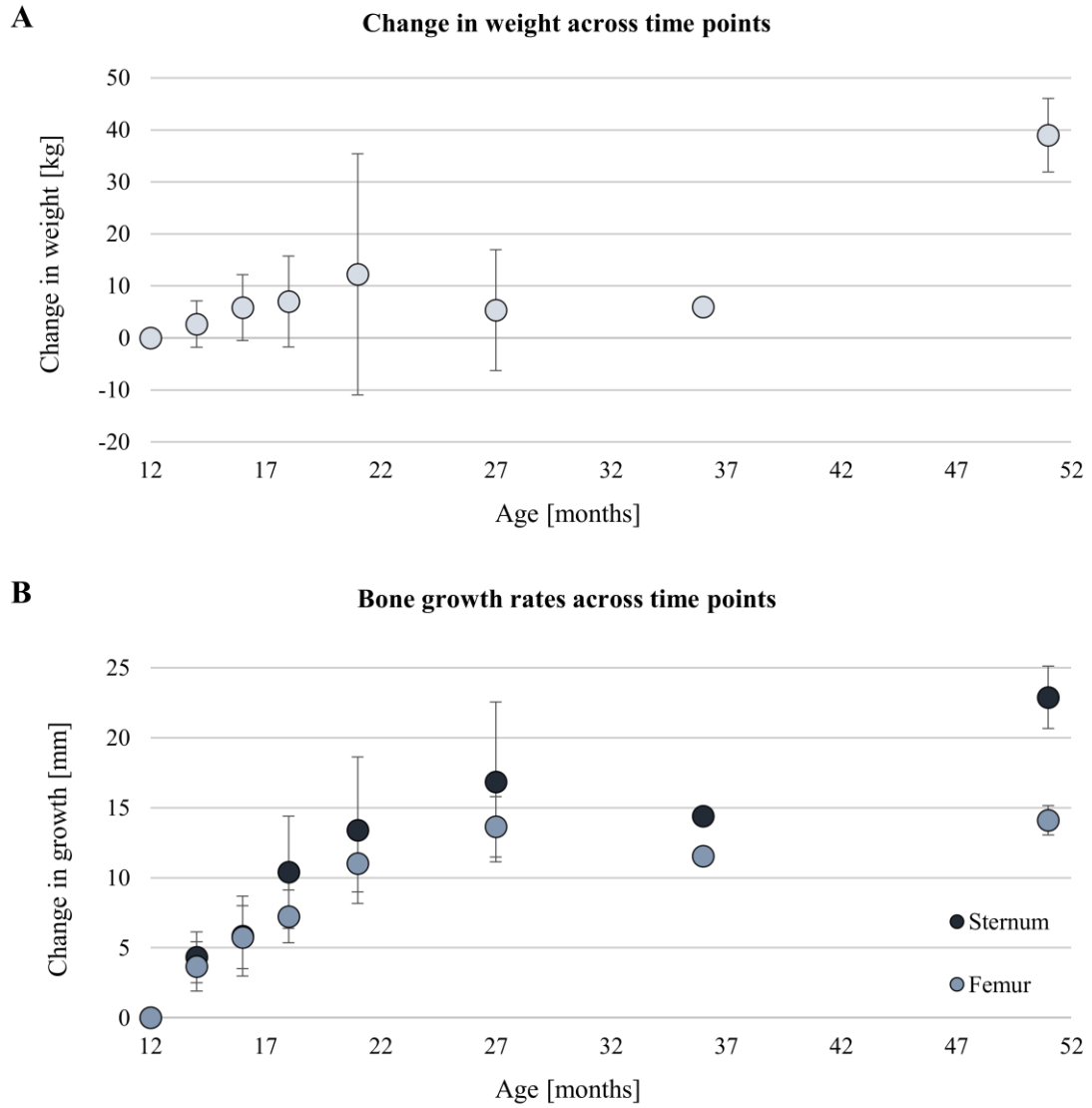
Figure 3-9: Skeletal growth and weight change. (A) Average change in weight across time points compared to the variable growth in the skeleton as demonstrated by the (B) sternum versus the left femur. All measurements are demonstrated as change from the first time point as illustrated by zero change at 12 months of age. Initial weight was 45.20 (± 10.66) kg, initial sternum length was 173.91 (± 11.43) cm, and initial femur length was 174.12 (± 7.98) cm.

3.4 Discussion

This chapter describes optimized CT and MRI acquisition methods for non-invasive characterization of disease development in porcine disease models. CT was selected for its fast acquisition of high resolution volumetric data, broad applicability, and wide availability in the clinical imaging field. MRI provided a strong complement with the lack of ionizing radiation making it ideal for longitudinal acquisition. Through the acquisition of 7 time points spanning over 3 years, we demonstrated the ability to use pig models for controlled longitudinal studies that is not easily accomplished with humans and with direct translatability not found with small animals. In addition, this work provides a platform methodology on which variations in targeted organ imaging may be developed as needed with potential extension to additional imaging modalities, such as positron emission tomography (PET). Further application of these imaging methods to several animal models is seen in CHAPTER 7 – CHAPTER 10.

Due to their comparable size, the use of large animals has been previously reported for the development and translation of CT protocols to aid in the quantitative CT characterization of human emphysema [67-69]. Furthermore, pig models have similar metabolic activity and lifespan providing a more robust surrogate for targeted therapies developed in large animal models for subsequent translation to humans [76, 77]. Our data acquisition was facilitated by the availability of dedicated research CT and MRI scanners and corresponding technologists at the University of Iowa. The imaging protocols for this study were chosen to parallel clinical protocols with an emphasis on obtaining the optimal achievable image phenotyping within an efficient research study time frame. In CT, minimization of radiation dose was not prioritized over high resolution, low noise images in the interest of obtaining high quality images throughout the whole-body. Studies evaluating recent CT technology aimed at lowering dose, including iterative reconstruction and dose modulation, have shown comparable qualitative and quantitative imaging data [3-5, 7, 78-80]. The use of such low dose protocols for whole-body screening in conjunction with targeted protocol development are demonstrated in CHAPTER 10: CONDITIONALLY ACTIVATED KRAS MODEL. In comparison, our MRI protocols required a balance between time and quality to achieve whole-body assessment within the target image acquisition period of one hour. Additionally, our MRI protocols were optimized within the limitations of available MRI scanner (3T vs. 1.5T), coils, and software. Specific focus on targeted acquisitions in lieu of whole-body screening could lead to shorter scan times with increased anatomic or functional detail, as demonstrated in CHAPTER 9: RADIATION EXPOSURE MODEL.

Incorporating medical imaging surveillance has proven to be a useful tool for pathological analysis of pig models. Imaging modalities can screen large volumes of tissue more effectively and efficiently than can be done at a typical necropsy. In these instances, detection of tumors via non-invasive medical imaging aids in the timing of necropsy and guidance of tissue collection for histopathological examination as demonstrated in CHAPTER 7: LI-FRAUMENI and CHAPTER 9: RADIATION EXPOSURE MODEL. Volume rendering is particularly advantageous, specifically using CT due to the acquisition of isotropic voxels providing finer detail. Once regions of interest are identified they can be spatially targeted by their distance as precisely as 1 mm from selected anatomic landmarks, similar to the way imaging can guide surgeons during an operation [81]. Thus, imaging modalities complement and improve pathological examination and assessment of pig models.

In addition to imaging methods, we have also described a method for consistently positioning pigs for longitudinal monitoring with assessment across time points and within time points facilitated by the design of a custom positioning unit. Similar longitudinal image positioning techniques have been employed for human cohorts specifically for the alignment of PET and MRI images of the breast focusing on imaging just the region of interest [82]. Our methods showed positioning across time points to be consistent within 17 mm on average following the acquisition of a rotational, translational, and anisotropic scaling transform to align acquired datasets; within time point positioning was visually confirmed and showed minimal change in positioning between modalities outside of the chest. Observed rotations in the chest may be explained by the differences in positioning of the front legs between MRI and CT where they were extended outside of the thoracic field of view. This qualitative and quantitative assessment showed the ability to control consistent positioning; however, additional external factors remained outside of our control, such as animal growth over time.

Yucatan miniature pigs have the potential for continuation of growth throughout their lifespan beginning at 0.5 kg at birth to 12-45 kg within 4 months and 45-100 kg within 1 year [56, 83]. Our time points began at one year of age to minimize the rate of growth change and allow for potential disease development to occur over 3.5 years of monitoring. While the majority of the rapid growth phase of the juvenile period (<16 months) [84] was excluded in this study, we still found continued skeletal growth that is variable across bones and is not consistently correlated to weight change. This continued growth is likely the cause of the increased error in skeletal alignment seen over time. This may also be of particular importance in conjunction with symptoms of disease, such as anorexia, that can influence weight gain/loss between imaging time

points suggesting an inherent error that cannot be completely accounted for by consistent positioning. While we still achieved average errors of less than 17 mm, the achieved errors were larger than desired for targeted region of interest analysis. Rather, this level of error indicates what was achievable with implementation of a consistent positioning schema supporting the need for a more sophisticated, post-acquisition registration approach as presented in CHAPTER 5: MULTI-LEVEL REGISTRATION.

Lastly, we chose the first acquired time point as the reference dataset to allow more time points to occur without requiring analysis to be repeated. To potentially minimize this trend, a different reference dataset may be used to reduce the temporal misalignment between the reference and all other datasets and lessen the degree of growth that may have occurred between time points. In some instances, it may also be desirable to begin screening before one year of age where more rapid development may occur. This, in conjunction with targeted acquisition protocols, may require additional considerations during positioning of the animal and data analysis.

In conclusion, the ability to longitudinally characterize porcine disease models with medical imaging presents an opportunity to develop novel validated CT and MRI protocols for direct translation to the diagnosis and treatment of human disease. We have demonstrated optimized CT and MRI imaging including the acquisition of tightly controlled protocols and the maintenance of consistent positioning with an average skeletal misalignment of less than 17 mm. These developed methods open the door for sustainable tracking and assessment of disease progression and lay a foundation for the development of qualitative and quantitative methods for comparison.

CHAPTER 4: STRUCTURED REPORTING

4.1 Introduction

In the field of radiology, structured reports have been developed as a method of standardizing radiology report information to guide measures, standardization, and improvement of delivering health care. These reports are generated to contain patient demographics, information about the imaging procedure, including date, time, and technical factors, and standard language that radiologists use to provide imaging observations and summarize findings [85]. Such reporting methods have been implemented in breast imaging and successfully evolved since the 1980s [86-89] with expanded growth to include a wide range of imaging uses. Increased adoption rates across radiology departments – typically in conjunction with an automated voice recognition system – have been shown to lead to less textual errors [90], better communication practices between radiologists and referring clinicians [91, 92], and improved clarity and content [93, 94]; however, limitations exist in efficient use and training in standard language [95].

The use of standard language leads to a natural interface with electronic health records for data mining purposes and an evidence based support system for determining and justifying optimal imaging methods for characterizing disease [85]. Different qualitative scales denoting the presence/absence or severity of a diagnosis have been reported for comparative studies [96, 97]; however, implementation of structured reports provides an inherent documentation for such analysis. For example, the Breast Imaging Reporting and Data System (BI-RADS) diagnostic categories [89] have previously been used for comparison of traditional mammography, breast ultrasound, and MRI for monitoring breast cancer in high risk patients [98]. In addition, these methods are important for the refinement of protocols for human applications, including detection, diagnosis, and monitoring of disease, and validation of novel imaging methods.

In this chapter, we present the use of developed structured reports for longitudinal, qualitative interpretation of the data acquired in CHAPTER 3: LONGITUDINAL MEDICAL IMAGE ACQUISITION. We also extend their use to present a systematic, semi-qualitative comparison of imaging protocols from both CT and MRI for lung assessment to determine the diagnostic strengths/weaknesses of the included MRI protocols versus the CT protocols . These results have previously been published by Hammond, et al. [99].

4.2 Materials and methods

Structured reports were developed, modeled after the Radiologic Society of North America (RSNA) radiology reporting initiative [100], to provide consistent, retrievable, and complete qualitative interpretation for each scan of an acquired time point. Each structured report led the assessment of the diagnostic quality of the scan, targeted anatomies, and peripheral structures with specific focus placed on whole-body screening for tumor progression. For identified tumors, the RECIST diameter [33, 34], including the dataset slice number corresponding to the measurement, was noted. Anatomic location, boundary appearance, and imaging characteristics were also reported. A comprehensive list of anatomies and other indicators of disease prompted for evaluation is listed in Table 4-1.

Table 4-1: Structured reporting anatomies. A comprehensive list of anatomies and indicators of disease assessed with the structured reports. Bold indicates a major organ of interest with indicators in italics and additional structures in plain text.

Head		Abdomen	
Brain	Musculoskeletal	**Liver**	
Nodules	Sinus	*Nodules*	**Kidneys, Adrenals**
Calcifications	Lymph nodes	*Calcifications*	*Nodules*
		Size	*Size*
Chest		*Iron*	*Fat*
Lungs		*Fat*	*Texture*
Right: cranial, middle, caudal		*Texture*	Bile ducts
Left: cranial, caudal		**Spleen**	Gallbladder
Accessory	Large airways	*Nodules*	Peritoneal fluid
Nodules	Esophagus	*Size*	Lymph nodes
Consolidation	Pleura	*Texture*	Peritoneum
Emphysema	Cardiovascular	**GI Tract**	Cardiovascular
Cysts	Lymph nodes	*Nodules*	Retroperitoneum
Bronchiectasis	Chest wall	*Lumen size*	Abdominal wall
Atelectasis	Lower neck	*Wall thickness*	Bladder
Bronchial wall thickening	Musculoskeletal	**Pancreas**	Musculoskeletal
Reticular abnormalities	*Nodules*	*Nodules*	*Nodules*
Ground-glass opacities	Mammary	*Size*	Mammary
Honeycombing	*Nodules*	*Fat*	*Nodules*
Linear opacities		*Texture*	

Structured reports were defined for each modality, subject, and screening time point and used by a radiologist for systematic reporting of findings. Diagnostic quality of each scan was tabulated and reported followed by full-body, structural assessment, incorporating both CT and MRI, in all animals for complete tumor phenotype characterization.

A comparative analysis study was performed with datasets acquired from the first four time points (12, 14, 16, 18 months of age) of the longitudinal image acquisition study described

in CHAPTER 3: LONGITUDINAL MEDICAL IMAGE ACQUISITION. Focus was placed on a subset of lung disease indicators to compare the relative merits of CT and MRI in characterizing lung disease. To minimize reader bias, scans were randomized by subject and time point within each modality resulting in pseudo time points. Developed structured reports were matched with the corresponding set and were read by a radiologist in one week intervals. The true subject and time point remained blinded to the radiologist at the time of reading.

The reported lung disease findings were divided into upper (right and left cranial, right middle) lung and lower (right and left caudal, accessory) lung. The T2 thoracic images and the T1 VIBE thoracic images were read in combination for the MRI structured reporting results. The gathered data was used to assess the percent agreement between the two imaging modalities with CT considered the gold standard for lung imaging. Percent agreement was calculated as the number of congruent findings, where both CT and MRI showed the same presence/absence of a condition, divided by the total number of time points. Results were also tabulated by modality and disease indicator to identify overestimation and underestimation of indicators by MRI compared to CT.

4.3 Results

A total of 14 unique structured reports were created corresponding to the acquired scans (3 CT scans, 11 MRI scans) and used for assessment of all acquired imaging datasets by a single radiologist (6 animals, 4 time points). Ninety-eight percent (71/72) of CT scans were of excellent diagnostic quality with a single non-contrast chest-abdomen-pelvis scan showing respiratory motion. In comparison, 100% of T2 MRI scans showed excellent diagnostic quality. Significant distortion was seen in all DTI scans of the brain demonstrating limited diagnostic capabilities. Twenty-nine percent (7/24) post-contrast chest VIBE scans showed aliasing artifacts, yet diagnostic ability was still maintained. Lastly, minor artifact was observed in a single (1/24) SPACE brain scan and a single set (1/24) of the dynamic VIBE abdominal sequence.

No significant tumor related findings were seen in the cohort of Li-Fraumeni animals imaged in CHAPTER 3: LONGITUDINAL MEDICAL IMAGE ACQUISITION providing a baseline measure of animals. Several small, calcified granulomas were noted across all animals in CT in the neck corresponding to the pre-anesthetic injection site. A 2.3 cm mass was detected in the right paracardial mediastinum in all chest MRI scans for subject I at 18 months of age displaying as hyper intense in T2 scans and isointense in T1 VIBE scans compared to soft tissue

with a defined border. Inspection in the corresponding CT scan showed a dense collection of blood vessels with no presence detected at subsequent imaging time points in both CT and MRI. Other findings include a chronically enlarged heart seen in subject J and caked small bowels among all animals. Lymph nodes were consistently measured for comparison showing a range of measures from 8 mm to 20 mm throughout the lymphatic system.

Table 4-2: Percent agreement between CT and MRI. Additional conditions included nodules, emphysema, cysts, reticular abnormalities and honeycombing, but were minimally identified. Percent agreement was calculated as the number of congruent findings (presence and absence of condition) divided by the total number of analyzed time points.

Lobe	Right cranial	Right middle	Right lower	Accessory	Left Cranial	Left Lower	Total
Consolidation	78%	87%	83%	100%	100%	48%	83%
Bronchiectasis	74%	83%	48%	96%	96%	52%	75%
Atelectasis	74%	78%	91%	96%	70%	78%	81%
Bronchial wall thickening	91%	100%	70%	100%	96%	83%	90%
Ground glass opacities	30%	96%	39%	100%	35%	30%	55%
Linear opacities	52%	52%	17%	96%	52%	17%	48%
Total	67%	83%	58%	98%	75%	51%	**72%**

The comparative analysis between CT and MR focused on findings in the chest, using CT as the gold standard. An overall 72% agreement was observed among all conditions in all lobes of the lung as seen in Table 4-2. MRI (including management of respiratory motion) was shown to be useful in the detection of consolidation, atelectasis, and bronchiectasis, and bronchial wall thickening with an agreement above 75% with CT in those categories. Linear opacities (48%) showed poor congruency, specifically in the lower lobes (17%), with CT. Upon further tabulation, it was seen that linear opacities were underestimated as seen in Figure 4-1. At only 55% agreement, MRI systematically over estimated ground glass opacities in the lungs, as indicated in Figure 4-1, particularly in the cranial and caudal lung lobes. Lobar location in the lungs showed higher agreement (67%, 75%) in the cranial lobes than the lower lobes (58%, 51%) with the right middle (83%) and accessory (98%) lobe showing the greatest agreement; however, minimal findings occurred in the right middle and accessory lobes with both modalities.

Figure 4-1: Frequency and congruency of noted conditions. Visual demonstration of the occurrence of disease indicators in the lungs separated by upper and lower lung and by subject. Time point is noted by quadrant per the key in the upper left corner. Black indicates the presence of a condition, white is absence of a condition, and gray denotes that that imaging did not occur at that time point.

4.4 Discussion

A structured reporting framework was developed to aid in systematic, longitudinal characterization of pig models where developed reports successfully led the evaluation of all images. A majority of scans demonstrated diagnostic capabilities even given minor artifacts; however, DTI scans showed significant distortions due to the large cavernous sinuses in the skull creating multiple bone/air interfaces [101]. No significant tumor related findings were seen in this cohort; however, baseline understanding of animals was inferred.

In addition, we performed a comparative analysis study to determine the relative merits of CT and MRI in the detection of lung disease characteristics. Predictably, CT was superior over MRI in the detection of fine structural details, such as linear opacities. Comparatively, MRI was shown to be reliable in the detection of bronchiectasis, atelectasis, and bronchial wall thickening. However, the results indicated a large disagreement in the incidence of ground glass detected in MRI compared to CT. It was inferred that this was the result of artifacts due to cardiac motion and contrast enhancement observed in the T1 post-contrast VIBE scans. To reduce reader bias, data was presented to the radiologist observer in a randomized, blinded fashion with assessments focused on detection (presence/absence) of conditions that have been well defined in the literature [102]. However, a limitation of this sub-study was that intra-observer and inter-observer assessments were not included.

It is important to note that pathology ground truth was not acquired for any conditions and real transient findings may have occurred given that MRI scans were acquired post CT acquisition. In addition, longer ventilation time may have increased the presences of atelectasis and additional secretions, specifically in the lower lobes despite lung recruitment maneuvers. Improved detection of lung conditions in MRI may be achieved with the use of cardiac gating and increased frequency of pulmonary recruitment. Due to these factors, routine imaging with CT is preferred for detection of early structural assessment with adequate capture of later stage disease development using MRI. Future application of ultra-short echo time (UTE) sequences could further enhance lung structure assessment of MRI [103, 104]. We can now use the developed structured reporting method and comparative analysis to assess performance of these methods.

The use of animal models presents an advantage in comparative studies. Systematic acquisition of multimodal images across multiple protocols using such models is possible without the risks and complications associated with human cohorts, such as radiation exposure. In our study, we acquired diagnostic quality images across several time points with multiple modalities.

In addition, the use of structured reports provided a standardized language across longitudinal time points and imaging modalities. We chose to focus our comparative analysis on lung indicators of disease, given that minimal findings were indicated by the radiologist in the head and/or abdomen; however, extension of these principles may be applied across the whole-body. With respect to cancer, multimodal, whole-body imaging comparative studies have previously been reported specifically related to tumor staging and metastatic disease between PET/CT and proton MRI [105], diffusion weighted imaging MRI [106], and PET/MRI [23], with PET/CT as the current clinical standard.

As previously mentioned in CHAPTER 3: LONGITUDINAL MEDICAL IMAGE ACQUISITION, CT requires the use of potentially harmful ionizing radiation with specific CT technological implementations aimed at reducing the amount of dose required for an examination. Additional strategies have included the substitution of MRI for CT where appropriate due to its lack of ionizing radiation [107], specifically in radiation sensitive patients, such as pregnant women and children. MRI has been explored as an acceptable alternative to CT imaging in cystic fibrosis patients [108-110]. Similar to our results, these studies suggest that MRI may be used as a reasonable alternative in the event of short-term follow-up. It is important to note that cystic fibrosis and tumor development are diseases that increase the amount of tissue present and, subsequently, MRI signal. In assessment of disease that results in loss of tissue, such as emphysema and chronic obstructive pulmonary disease, imaging with low dose CT may remain more prudent.

CHAPTER 5: MULTI-LEVEL REGISTRATION

5.1 Introduction

Systematic acquisition of medical images provides a substantial database for the testing and development of image processing tools for characterization of porcine disease models with direct translational application to clinical disease management. Registration is an image processing technique that aligns similar anatomical structures across different images. This is beneficial for understanding disease progression through the identification of the same region over time to evaluate relative change. Longitudinal imaging has frequently been performed with MRI, specifically on the brain. Image registration has been used in this context to study the cortical reduction in the development of psychosis by comparing regional changes over time [111]. Applications to brain tumors, such as gliomas and meningiomas, have included automatic change detection and intensity mapping using a combination of segmentation and registration [42]. In these instances, registration in conjunction with additional processing/analysis provided relevant clinical information.

Longitudinal imaging is also important for clinical cancer management. Screening programs have been recommended and implemented for breast and lung cancer that include annual imaging for high-risk individuals. These programs are aimed at early detection of tumors and inclusion of risk assessment by analyzing nodule/tumor change over time [9, 112]. Change is also important in assessing treatment. Current clinical practices use the RECIST as a quantitative measure to determine complete response, partial response, stable disease, or progressive disease [33]. With the advent of immunotherapy, these measures may not accurately reflect the pattern of response as treatment has shown to result in delayed response via no change in tumor size, increased tumor size, or the appearance of new lesions that occur prior to a decline in tumor burden [113]. The use of registration with additional analysis across longitudinal images presents the opportunity to monitor regional change with greater sensitivity to tumor progression.

This chapter describes a multi-level registration algorithm designed to align similar anatomical structures relating to disease development in longitudinal datasets for investigating early precursors of disease and tracking disease progression. The algorithm was designed to accommodate the datasets acquired in CHAPTER 3: LONGITUDINAL MEDICAL IMAGE ACQUISITION, including the use of both CT and MRI, growth of an animal over time, and whole-body acquisition. Similar objectives have been required for alignment of longitudinal

images of small animal models resulting in articulated registration of images to a skeletal atlas [71]. We present a technique that focuses on alignment of a specific anatomy or diseased region of interest using surrounding anatomical structures as a guide during registration. Additional considerations include the need for adaptability and reusability of processing techniques to various phenotypes from a wide variety of disease models. First, we present our multi-level registration algorithm followed by its application to align desired regions of interest in the whole-body datasets.

5.2 Materials and methods

A multi-level registration algorithm was developed to align anatomical structures of interest in longitudinal datasets. The algorithm consisted of initialization followed by the repeated application of a core registration framework as the input data reduced in image field of view. Details regarding pre-processing, initialization, the registration framework, the multi-level process, and metrics used for validation are described in the following sections. All developed code was implemented with the ITK libraries and packaged as a 3D Slicer extension for interaction with the greater medical image processing community.

Preprocessing: Thresholding was implemented as a pre-processing step in the event of large disparities in intensities between fixed and moving images. For example, brain imaging in MRI results in greater detail about the brain structures compared with CT brain imaging. Upper and lower thresholds were user defined such that the image intensities above and below the defined thresholds, respectively, were set to the given thresholds.

Initialization: Initialization of the complete multi-level approach was performed using alignment via the center of geometry of the images. Additional initialization was performed for image sets with a large disparity in the coverage of anatomy (i.e. CT coverage including the chest, abdomen, and pelvis in a single dataset aligned with an MRI dataset containing the chest) and/or large positional changes across time points as shown in Figure 5-1. For large translational and rotational differences, the negative mutual information metric was calculated between the two images at defined translation steps and/or rotational steps. The moving image was translated along the length of the fixed image in a desired direction – axial, coronal, and/or sagittal – in twenty equal steps. The translation resulting in the largest negative value was chosen as a new initialization. After the desired translation was acquired, the moving image was rotated from -45º to 45º in 2º steps about a desired plane – axial, coronal, and/or sagittal – to acquire the optimal

rotational alignment. Additionally, for targeted region of interest acquisitions, rasterization through the fixed image in 125 steps was performed (i.e. MRI brain scan aligned with the CT head scan). Lastly, if those initialization techniques were inadequate, the use of a manually defined transformation was optional for initialization.
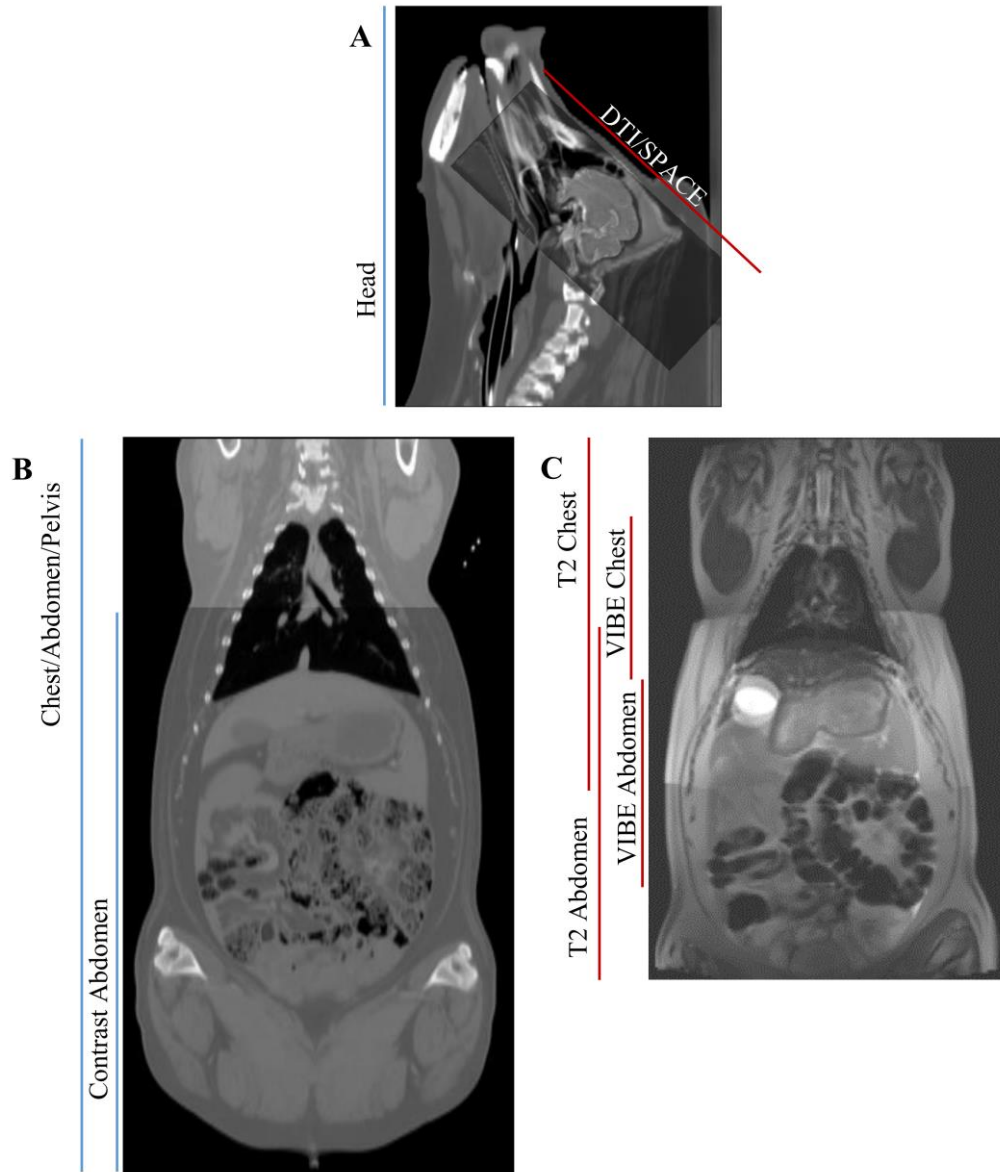
Figure 5-1: Anatomic coverage by modalities. Visual demonstration of the anatomic coverage in the (A) head for both MRI and CT and the rest of the body for (B) CT and (C) MRI.

Registration framework: A registration framework was developed to align images without non-linear warping of the data, preventing the distortion of data related to disease development and/or change. Registration was performed with a rigid transform allowing for

global translation, global rotation, and anisotropic scaling accounting for changes in positioning and growth of the animal over time. The rigid transformation is defined in equation (5-1) where $\mathbf{x}^\grave{}$ is the transformed point, $\mathbf{x}$ is the original point, S is the scaling matrix, T is the translation vector, and R_v is the rotational matrix.

$$\mathbf{x'} = (R_v + S)\mathbf{x} + T, \text{ where}$$

$$S = \begin{pmatrix} s_0 - 1 & 0 & 0 \\ 0 & s_1 - 1 & 0 \\ 0 & 0 & s_2 - 1 \end{pmatrix} \text{ and } T = \begin{pmatrix} t_0 \\ t_1 \\ t_2 \end{pmatrix} \qquad (5\text{-}1)$$

R_v is the rotational component of the transformation described by a unit quaternion, known as a versor, defined in equation (5-2), where α is the rotation angle and u is the axis of rotation. The rotational matrix, R_v, can then be generated by equation (5-3) [114].

$$q = w + xi + yj + zk = w + (x, y, z) = cos\left(\alpha/_2\right) + sin\left(\alpha/_2\right)u \qquad (5\text{-}2)$$

$$R_v = \begin{bmatrix} w^2 + x^2 - y^2 - z^2 & 2xy - 2wz & 2wy + 2xz \\ 2wz + 2xy & w^2 - x^2 + y^2 - z^2 & 2yz - 2wx \\ 2xz - 2wy & 2wx + 2yz & w^2 - x^2 - y^2 + z^2 \end{bmatrix} \qquad (5\text{-}3)$$

During registration, a regular step gradient descent optimizer parsed through the parameter space of the defined transform until the negative mutual information was minimized. Mutual information was chosen as the metric for its adaptability in registration of multi-modality datasets and calculates the amount of statistical dependence between the two images. It is defined in equation (5-4) where H(F) and H(M) define the entropies of the individual images and H(F, M) defines the joint entropy [73]. Entropy is defined in equation (5-5) where $p_A(a)$ is the probability of intensity a occurring in image A as defined by the histogram of the image intensities.

$$Mutual\ information: MI(F, M) = H(F) + H(M) - H(F, M) \qquad (5\text{-}4)$$

$$Entropy: H(A) = -\int p_A(a)\ logp_A(a)\ da \qquad (5\text{-}5)$$

Region of interest selection: Volumetric rectangular regions of interest (ROIs) were selected in the fixed image space only to reduce the image field of view at each level,

demonstrated in Figure 5-2. Initial field of view corresponded to all available image data. ROIs were then defined isolating an anatomic region (i.e. thoracic organs, abdominal organs) to reduce the field of view. Further reduction was achieved with a final ROI isolating a specific anatomy of interest (i.e. upper right lung, brain, kidney). For adaptability to a wide array of disease models, minimal restrictions were placed on the number of ROIs created given they correspond to the number of desired registration levels and are generated such that they reduce the field of view at each level.

Multi-level approach: Following initialization, the registration framework was applied and the field of view was reduced for the number of desired levels in the following manner. All previous transforms were applied to the initial moving image, including the initial transform, resulting in the moving image defined in fixed image space. Both the fixed and moving images were then cropped per the first defined ROI and the registration framework was applied to the cropped images. This process – transformation, cropping, registration – defined a level, was then repeated for the specified number of ROIs.
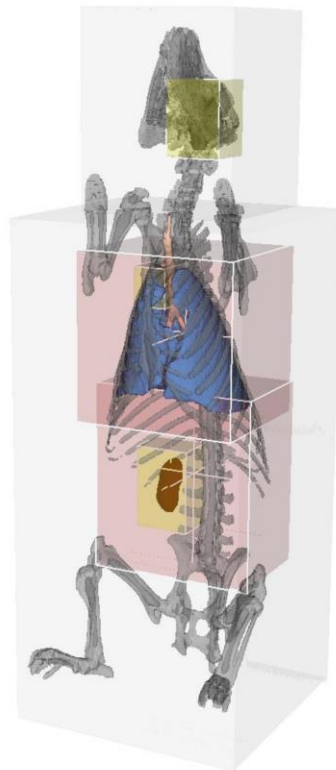
Figure 5-2: Multi-level regions and anatomies of interest. Demonstration of the reduction in volume used at each level of registration using three-dimensional renderings of the masks used for validation and isolation of the skeleton. The largest volume (gray box) was used for whole image registration. The red volume indicates the second from last level of reduction (F-1) and the yellow box indicates the final level of reduction (F).
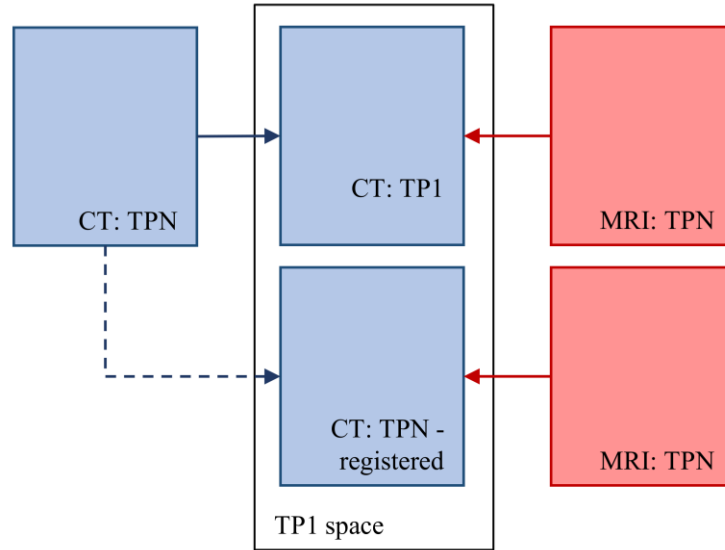
Figure 5-3: Registration flow. Illustration of how CT and MRI images were registered and aligned in the image space from the first time point. Lines represent the relationship between images such that solid lines extend from the moving image to the fixed image and the dotted line represents the resampling of the image from moving image space to fixed image space.

Application: The multi-level registration algorithm was applied to align the acquired longitudinal datasets described in CHAPTER 3: LONGITUDINAL MEDICAL IMAGE ACQUISITION focused on three anatomies of interest: the brain, the upper right lung, and the right kidney. Non-contrast, chest-abdomen-pelvis CT images at each time point were registered to the corresponding CT images acquired at the first time point. Non-contrast abdominal VIBE and post-contrast chest VIBE MRI acquisitions were then registered to the CT image acquired at the first time point through registration with the corresponding CT image previously transformed into baseline image space as described in Figure 5-3. All final transformed images were presented in the first time point image space to enable direct comparison with the first CT image acquired.

To demonstrate the benefit of a multi-level approach, a second set of registrations was performed on solely the anatomy of interest isolated with a rectangular ROI. ROIs were created independently in all acquired images corresponding to the anatomies of interest and used to crop each image. Registration was performed between cropped images using the same rigid registration framework initialized by center of geometry. Results were similarly presented in baseline image space.

Validation: Validation was performed with visual assessment, target overlap measures, and average Hausdorff distance measures to assess the performance of the two registration methods. Quantitative measures were obtained after initialization and after each level of

42

registration to assess the performance of the multi-level registration algorithm. For comparison to the multi-level approach, equivalent quantitative measures were obtained on the results from the single step, cropped image registrations. Difference measures were calculated comparing results between the two registration methods obtained on the same anatomy of interest. Differences were tested for normality using the Jarque-Bera goodness-of-fit test and significance was determined with a paired t-test or a Wilcoxon signed paired rank test for normal and non-normal data, respectively.

Lung masks in CT images were generated via in-house software (PASS: Pulmonary Analysis Software Suite [115]) excluding major airways and vessels to assess gross overlap of the lungs. For assessment of internal alignment of the lungs, CT airway masks were acquired with the Apollo software (VIDA Diagnostics, Coralville, IA) and eroded to isolate the main airway branches. MRI airway masks, incorporating the trachea and the left and right main bronchi, CT kidney masks, and MRI kidney masks were manually segmented with the Editor module in 3D Slicer. CT and MRI brain masks were acquired with a basic thresholding technique and manually modified using the Editor module. These segmentation masks were then used to acquire quantitative measures for registration validation.

Target overlap (TO), defined in equation (5-6), was used to calculate the amount of overlap of segmented structures with respect to the fixed image mask where M_f is a mask of the anatomy in the fixed image and M_m is the mask of the anatomy in the moving image. This relates to the sensitivity of the algorithm, indicating the percent of voxels that are correctly aligned. A value of zero indicates no overlap, while a value of one indicates perfect overlap [116].

$$Target\ Overlap\ (TO) = \frac{\left|M_f \cap M_m\right|}{\left|M_f\right|} \qquad (\ 5\text{-}6\ )$$

Distance measures were also acquired to assess misalignment at the boundary of the aligned structures. The average Hausdorff distance (aHD) was calculated by averaging the minimum distances between edge pixels, after zeroing all negative distances to remove areas of overlap. The formula is shown in equation (5-7) where i are edge pixels in M_f and j are edge pixels in M_m. Calculations considered the distances from the moving mask to the fixed mask and vice versa. A value of zero indicates perfect border alignment where a value greater than zero indicates misalignment expressed in millimeters.

$$Average\ Hausdorff\ distance\ (aHD)$$

$$= \frac{1}{2}\left(\frac{1}{I}\sum_{i=1}^{I}\ \underset{i\ \in\ M_f}{min}\{\,d(i,j)\,\} + \frac{1}{J}\sum_{j=1}^{J}\ \underset{j\ \in\ M_m}{min}\{\,d(i,j)\,\}\right) \qquad (\ 5\text{-}7\ )$$

An outline of the completed algorithm is displayed in Table 5-1 and the completed graphical user interface within 3D Slicer is displayed in Figure 5-4.

Table 5-1: Multi-level registration algorithm. An outline of the multi-level registration algorithm to align the moving image to the fixed image at each level.

Read in fixed image (**F**) and moving image (**M**)
If fixed image transform is defined, apply to fixed image (**F**)
Perform preprocessing
Perform initialization
Add initial transform to composite transform
For the number of defined levels
If number of levels is equal to the number of ROIs and it is the first iteration
Apply composite transform to moving image (**M**)
Crop fixed image (**F**) and moving image (**M**) with first defined ROI
Define cropped images as fixed image (**f** = **F**) and moving image (**m** = **M**)
If it is not the first iteration
Apply composite transform to moving image (**M**)
Crop fixed image (**F**) and moving image (**M**) with the next defined ROI
Define cropped images as fixed image (**f** = **F**) and moving image (**m** = **M**)
Else
Apply composite transform to moving image (**M**)
Define the fixed image (**f** = **F**) and moving image (**m** = **M**)
If it is not the first iteration
Divide previous level registration parameters by the parameter relaxation factor
Else
Set registration parameters as defined
Apply registration framework on the defined fixed image (**f**) and moving image (**m**)
Add resulting transform to composite transform
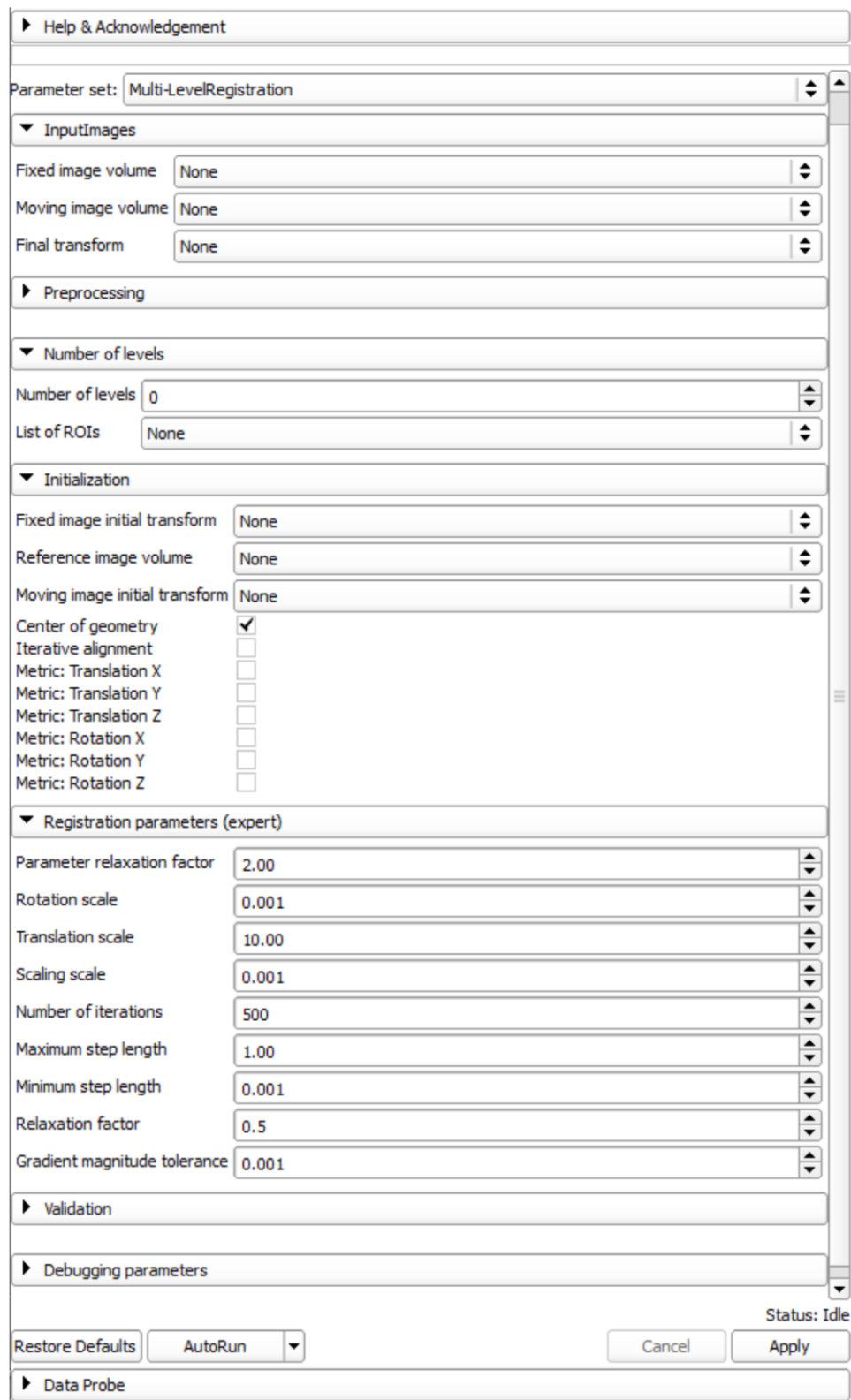
Figure 5-4: Slicer GUI with multi-level registration GUI. A screenshot of the graphical user interface designed within 3D Slicer for the multi-level registration. This corresponds to the left most panel in 3D Slicer with windows for image viewing and rendering in panels to the right.
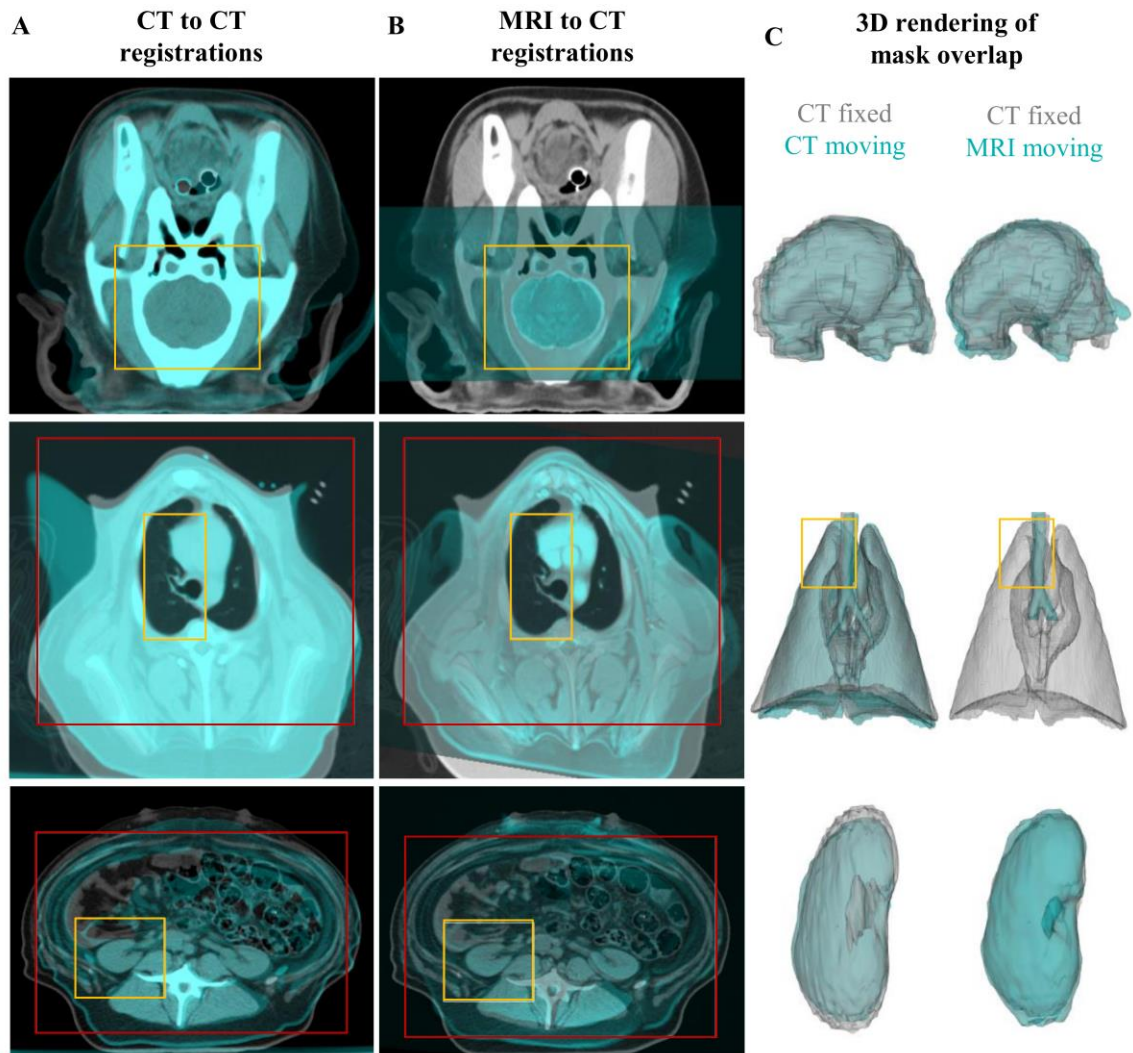
Figure 5-5: Multi-level registration results. Final registrations for a single subject of the brain with datasets acquired at 12 and 16 months of age (first row), upper right lung with datasets acquired at 12 and 18 months of age (middle row), and the right kidney with datasets acquired at 12 and 27 months of age (bottom row) shown through (A) CT to CT registrations and (B) MRI to CT registrations. The fixed image used for registration is shown in standard grayscale intensities with the moving image shown as an overlap with cyan intensities. The red box indicates the second from last level volume reduction (F-1) and the yellow box indicates the final volume reduction (F). (C) Overlap of three-dimensional renderings of the masks used for validation to demonstrate volumetric alignment with both CT to CT and MRI to CT registrations with the same color scheme applied from A and B.

5.3 Results

A total of 90 CT to CT and 83 MRI to CT multi-level registrations were performed for a total of 173 registrations for all three volumes of interest. Three levels of registration were utilized for alignment of the upper right lung and right kidney with both CT to CT and MRI to CT registrations with applied ROIs illustrated in Figure 5-2. Initialization was performed by center of geometry with additional translational or rotational alignment when large discrepancies in

46

alignment were identified. A total of 5 manual initializations were required for the upper right lung registrations and 11 for the right kidney registrations. Initialization was followed by whole-image registration for alignment with the baseline CT image. Following whole image registration, the second level of registration used an average 85% and 88% reduction in fixed image volume to isolate the lungs and the abdomen, respectively. An additional average of 98% and 93% reduction in fixed image volume was used to isolate the upper right lung and right kidney, respectively, for the last level of registration. Total amount of time required for upper right lung and right kidney registration was 143 ($\pm$ 39) seconds and 126 ($\pm$ 51) seconds, respectively.

Two levels of registration were used for CT to CT alignment of the brain initialized by center of geometry with applied ROIs illustrated in Figure 5-2. Initialization was followed by whole image registration and a reduction of 95% in fixed image volume for the final level of registration for a total time of 43 ($\pm$ 16) seconds. Due to large disparities between intensities within the brain in CT and MRI, MRI brain scans were preprocessed by thresholding such that all intensities greater than a value of 145 were set to 145. This value was chosen such that a uniform intensity within the brain was observed mimicking the corresponding CT scan. Initialization was performed using rasterization along the CT head scan with 11 manual initializations required and was followed with 1 level of registration corresponding to the ROI defined around the brain in the CT image requiring 25 ($\pm$ 21) seconds to complete.

Registrations were visually confirmed showing a majority overlap of desired structures. Due to the rigid transform, qualitative assessment was focused on structures within the region of interest. Visual demonstration of final alignment can be seen in Figure 5-5. Final transforms showed decreasing amounts of rotation at each level with an average rotation of 1.60 ($\pm$ 1.56) degrees required for all transforms at level 1, 1.39 ($\pm$ 1.17)º at level 2, and 0.29 ($\pm$ 0.23)º at level 3. Similar trends were observed across all other parameters with translations of 1.80 ($\pm$ 12.41) mm, 0.95 ($\pm$ 5.97), and 0.08 ($\pm$ 0.76) mm for all axes during level 1, level 2, and level 3 registrations, respectively. Minimal scaling was observed across all levels of registration with average values of 1.01 ($\pm$ 0.03) in all axes.

A **Target Overlap by volume of interest**

B **Average Hausdorff Distance by volume of interest**
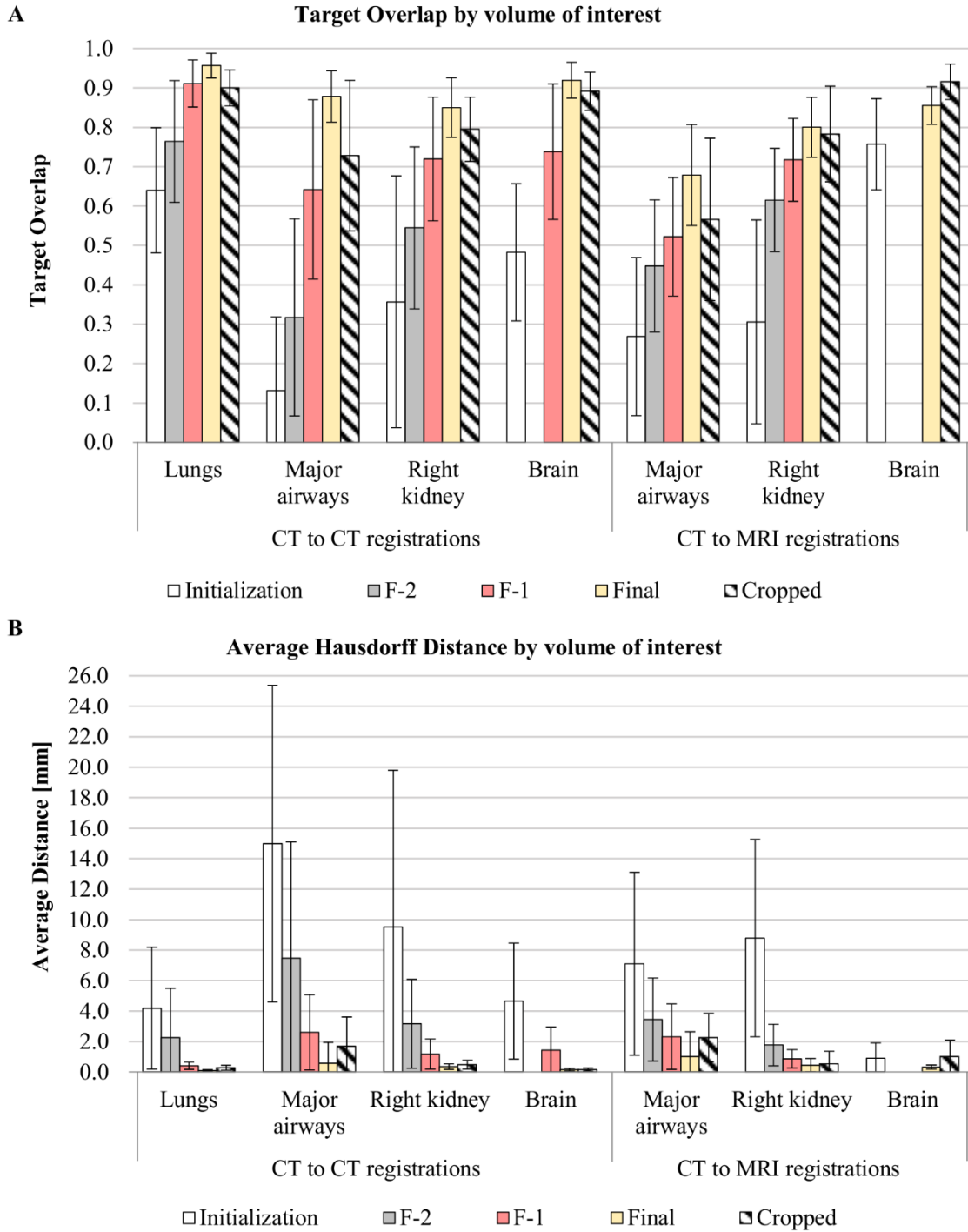
Figure 5-6: Multi-level registration validation. Validation measures (mean ± standard deviation) by level for each anatomy of interest separated out by type of registration (CT-CT, MRI-CT) showing the increase in target overlap (A) and decrease in average Hausdorff distance (B) as the volumetric region of interest decreased. The measures are in order of initialization, second from last volume reduction (whole dataset registration for the upper right lung and right kidney), first from last volume reduction (abdominal and chest region of interest registration and whole dataset registration for the brain), and final volume reduction level and compared to results from the cropped registrations.
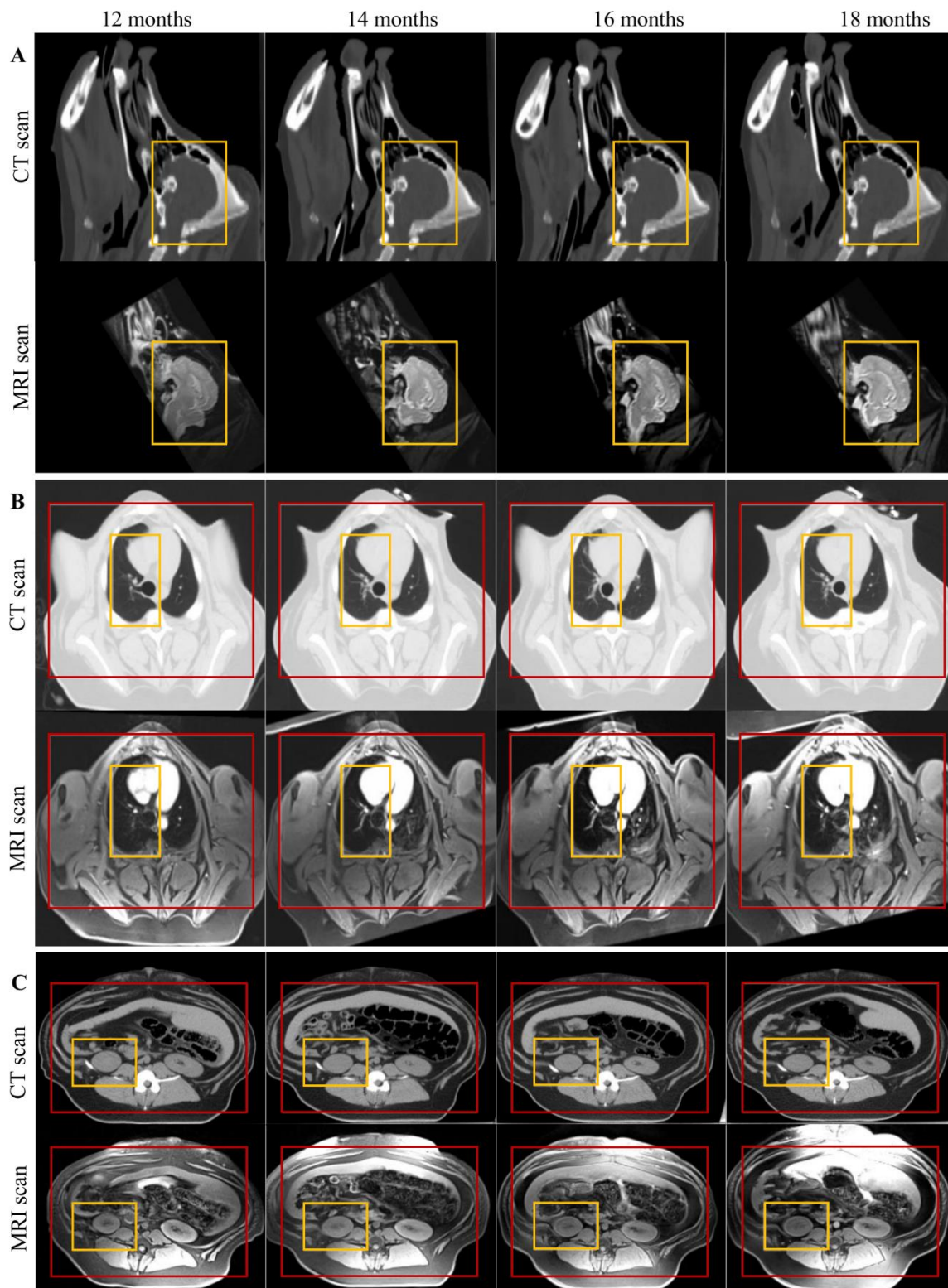
Figure 5-7: Longitudinal registration results. Final (A) brain, (B) lung, and (C) kidney registrations (CT-CT top, MRI-CT bottom) for subjects with datasets acquired at 12, 14, 16, and 18 months of age. The red box indicates the second from last volume reduction (F-1) and the yellow box indicates final volume reduction (F). Images are presented in registered image space corresponding to 12 months of age.

To validate the alignment of anatomies at each step of registration, TO and aHD measures were obtained. The resulting transforms following initialization and each subsequent level of registration were used to align the anatomical masks to the baseline masks. Once the masks were aligned, TO and aHD measures were computed to quantify the agreement of anatomies. Similar trends were observed with all registrations. Initialization showed the least amount of TO at 0.43 ($\pm$ 0.29) for all registrations with increasing TO seen with each level of registration with an average of 0.54 ($\pm$ 0.24) TO after level 1, 0.72 ($\pm$ 0.19) at level 2, and a final TO of 0.85 ($\pm$ 0.11) at level 3. Similar trends were observed regarding the aHD with measures of 7.14 ($\pm$ 7.93) mm, 3.68 ($\pm$ 4.74) mm, 1.44 ($\pm$ 1.71) mm, and 0.41 ($\pm$0.83) mm, respectively from initialization to final registration result. CT to CT registrations performed better than MRI to CT registrations with an average final TO of 0.90 ($\pm$ 0.08) compared to 0.78 ($\pm$0.11) and final aHD measures of 0.34 ($\pm$ 0.81) mm compared to 0.57 ($\pm$ 0.97) mm, respectively. Given in-plane resolutions of 0.6-0.8 x 0.6-0.8 mm^2 for CT acquisitions (depending on field of view) and 1.37 x 1.37 mm^2 for MRI acquisitions, final aHD measurements were sub-resolution on average.

Similar trends were observed among individual regions of interest, seen in Figure 5-6. CT to CT registration of the upper right lung via the lung mask showed the greatest TO and smallest aHD with final values of 0.96 ($\pm$0.03) and 0.10 ($\pm$ 0.06) mm, respectively. The smallest TO for CT to CT registrations was observed for the right kidney with a final TO of 0.85 ($\pm$0.08) and aHD of 0.36 ($\pm$0.18) mm. For MRI to CT registrations, the greatest alignment was in the brain with final values of 0.86 ($\pm$ 0.08) and 0.32 ($\pm$ 0.14) mm for TO and aHD, respectively. Overall, the smallest final TO and largest aHD were observed in the major airways for the MRI to CT registrations with values of 0.68 ($\pm$ 0.13) and 1.01 ($\pm$ 1.63) mm, respectively. An example of longitudinal alignment is shown in Figure 5-7 demonstrating the final registered location of the brain, upper right lung, and right kidney in baseline CT image space.

An additional 173 registrations were performed solely on the cropped images and difference measures were calculated. Results of the comparison between the final level of the multi-resolution approach (Final), compared to that of the cropped regions without the multi-level approach (Cropped) are summarized in Figure 5-6. Overall, the multi-level registration algorithm had an improvement of TO of 0.05 ($\pm$ 0.14) greater and an improved aHD of 0.47 ($\pm$ 1.2) mm less than the cropped registrations. The greatest improvement was seen in registration of the upper right lung comparing measures obtained from the airway masks with average TO improvement of 0.15 ($\pm$ 0.18) for CT to CT registrations (p-value <0.0001) and 0.15 ($\pm$ 0.23) for CT to MRI registrations (p-value 0.0036). Average HD measures improved on average by 1.13 ($\pm$ 1.80) mm

for CT to CT registrations (p-value <0.0001) and by 1.17 (± 1.88) mm for CT to MRI registrations (p-value 0.0049). The least amount of improvement was seen in registration of the brain with minimal improvement of 0.03 (± 0.04) for TO (p-value 0.0012) and 0.00 (± 0.12) mm for aHD (p-value 0.4653) for CT to CT registrations. CT to MRI cropped registrations in the brain showed a higher TO than the multi-level registration algorithm with an average value of 0.06 (± 0.07) (p-value < 0.0001); however, the multi-level registration algorithm still showed an average 0.68 (± 1.07) mm improvement in aHD measures (p-value 0.0004). Significant improvement was observed with CT to CT registration of the right kidney (TO: p-value 0.0006, aHD: p-value 0.0135); however, no significance was seen in CT to MRI registrations of the right kidney (TO: p-value 0.3695, aHD: p-value 0.2059).

5.4 Discussion

We have developed a multi-level registration algorithm for alignment of longitudinal images. The algorithm was designed to accommodate multiple applications with minimal restrictions placed on the number of levels or the reduction in size of the regions of interest. We have demonstrated its capabilities on longitudinally acquired CT and MRI data of pigs showing alignment in the brain, upper right lung, and right kidney with improvement shown over isolated registration of the anatomy of interest. Common preprocessing and initialization techniques were included in the pipeline; however, those included are not exclusive. The registration framework can also be adapted to fit a more specific application while still incorporating the multi-level approach. Here, we have developed a framework that can be generalized to fit a wide range of applications throughout the body, such as disease progression and response to treatment, as well as injury resolution. Additional inclusion of the 3D Slicer and ITK communities allows for inherent interaction with our algorithm and the greater medical imaging community.

Our registration framework contains a rigid transform allowing for global translation and rotation and anisotropic scaling. The nature of biological variability in longitudinal imaging poses a unique problem with respect to the fact that there is not an expected perfect match between two time points, especially if major disease changes have occurred. With the use of a rigid transform, it is guaranteed that visual representation of the region of interest, and potential disease change within, will be maintained. Additionally, the multi-level process accommodates for the comprehensive anatomy acquired in the images and iteratively focuses on a specific region of interest. Following this process, the addition of a non-rigid registration algorithm could further improve the final TO and aHD of structures within a desired region of interest. Several such

51

longitudinal algorithms have been reported for specific anatomical alignment with registration performed on a previously isolated volume of interest. These include alignment of tumors in human breast [43-45, 117], liver [41], brain [42, 118], and lung [31] cancer for modeling organ and tumor deformation and assessing volume changes during treatment.

In addition to biological change, positioning of the subject between time points and modalities and imaging modality coverage influenced final alignment. The wide range of techniques used in this study for initialization accommodated significant positioning differences. There were only 27 image registrations out of 173 that required manual initialization, the majority (20/27) which were for MRI to CT image registrations. For this study, our image registration method used the maximum amount of information in each image. Due to the wide coverage of anatomy, the acquired CT images contained a much larger field of view compared to the acquired MRI images. Specific acquisition of targeted anatomy may reduce the need for a complex initialization process and simplify the number of levels required during image registration. In addition, research has been done extending feature detection algorithms to medical imaging, such as scale invariant feature transform (SIFT) and speeded up robust features (SURF), for feature based registration [119]. Recent applications to multimodal registration [120] and stitching of spine MRI datasets [121] suggest the potential for use as an initialization technique which may also reduce the need for manual initialization specifically in multimodal applications with large differences in image field of view.

The use of the multi-level approach allows for the incorporation of various levels of reference anatomy to aid in alignment of a diseased region. We included a comparison between our developed approach and isolated registration of the anatomy of interest using the same registration framework. The multi-level approach showed significant improvement in all but one of the registration tasks. The largest and most significant improvement was noted in alignment of the upper right lung, specifically in alignment of the major airways. This may be due to the small amount of surrounding reference anatomy compared to the right kidney and brain which showed less improvement. Significant improvement was observed in CT to CT registrations of the right kidney with no significance found in the CT to MRI registrations. This may be due to the acquisition of CT and MRI occurring on the same day with minimal positioning differences between modalities. CT to MRI registration of the brain showed a lower TO with our method compared to isolated registration; however, a greater aHD distance was observed. Visual inspection of the isolated registrations showed large amounts of rotation not corrected for in the final transformation without the multi-level approach. This indicates the importance of

initialization given the wide range in image field of views at acquisition, specifically in multimodal applications.

We demonstrated the use of a maximum of three levels due to the large reduction in volume used at each level with a final reduction focused on a single anatomical structure. For our method, a level is defined as the combined application of a set of transformations to the moving image, cropping of the fixed and moving images, and registration of these images. In this instance, the registration framework is applied to varying image field of views at each level depending on the defined ROIs. Several other multi-level registration techniques have been widely used in image processing to reduce the complexity of the registration process. These include increasing the complexity of the transformation in a hierarchical approach [122] and decreasing the amount of applied smoothing or increasing the resolution of the image data at each level in a scale space approach [123]. In comparison, these methods are applied to the entire image field of view at each registration level and may be more applicable given a targeted image acquisition where the region of interest composes the entire image.

In conclusion, in this study we have developed and applied a multi-level registration approach to longitudinally acquired CT and MRI image datasets. We have shown generalizability of the algorithm through the registration of three regions of interest – brain, upper right lung, and right kidney – in both CT and MRI images. Further, it was applied to longitudinal image datasets of a porcine disease model presenting substantial longitudinal changes in subject anatomy due to disease progression. The new image registration method reported here increases the ability to extract meaningful CT and MRI image biomarkers of disease to systematically phenotype presentation and progression of disease.

CHAPTER 6: LONGITUDINAL FEATURE EXTRACTION

6.1 Introduction

Understanding the spatial and temporal relationship between imaging based features has the potential to provide further insight into differentiating cancer phenotypes. This trend towards personalized medicine has led to the growth in development of quantitative imaging biomarkers for identification and differentiation of pathologic processes [124]. This has involved segmentation of a tumor or region of interest followed by extensive image feature extraction and can include external feature inclusion, such as demographic and genomic information. The most important features are then identified with a feature reduction schema and used for classification [49, 51]. In these situations, measurements and features are acquired and assessed independently in each image. Incorporating feature change over time, including regional matching of features via image registration, gives way to further provide important information in disease change.

Current imaging features used in clinical assessment have included basic quantitative size measurements and qualitative assessment of visual tumor characteristics. Of the most notable, size measurements have included the World Health Organization bi-dimensional measurement [32] and the Response Evaluation Criteria in Solid Tumors (RECIST) uni-dimensional measurement – the current clinical standard [33, 34]. However, these criteria are limited to solid tumors, reliant upon subjective measurements, and do not consider the volumetric nature of medical imaging. With improvements in medical imaging and image segmentation techniques, recent research has focused on volumetric assessment of tumor burden as a more representative measure [39, 125-127]. These advancements, in conjunction with image registration, present the opportunity to additionally track change in shape and directional growth over time as valuable future biomarkers.

This chapter focuses on an extension of the multi-level registration algorithm to demonstrate the ability to incorporate directional growth into progression and response evaluation and include regional matching of features for the identification of early biomarkers of disease. The developed techniques are applied to a phantom dataset focused on a chest CT with a simulated tumor in the upper left lung and simulated progression of a non-solid to solid ground glass lesion in the upper right lung. Applications of the longitudinal feature extraction approach and additional methods for the evaluation of specific animal models are described in CHAPTER 7 – CHAPTER 10.

An extension was developed in the 3D Slicer framework to aid in the extraction of features in aligned longitudinal datasets. The extension can accommodate two or more image datasets from the same subject. Additional input is the transforms required to align each image into the reference image space as described in CHAPTER 5: MULTI-LEVEL REGISTRATION. The extension subsequently allows: a) features to be extracted from a consistent, propagated volume of interest and/or b) relative change in shape over time determined from independently segmented volumes of interest. An outline of the algorithm is displayed in Table 6-1 with the generated graphical user interface is displayed in Figure 6-1.

Table 6-1: Longitudinal feature extraction algorithm. An outline of the algorithm designed to extract features in an aligned longitudinally acquired dataset. User activated actions and inputs are obtained from the graphical user interface (GUI) and indicated in bold.

Specify the number of images, **N**, in longitudinal dataset

Select a **file** to store results

Identify reference image, **I₁**, and corresponding segmentation, **S₁**

If **resample mask** (individual image space)

    For N-1 images I_n

        Define transform, T_n, from image I_n to image I_1

        Apply the inverse transform, $inv(T_n)$, to S_1 resulting in S_n

If **calculate statistics**

    For N images I_n

        Define image I_n and corresponding segmentation S_n

        Extract features from image I_n within S_n

    Print out results to file

If **resample mask** (reference image space)

    For N-1 segmentations S_n

        Apply transform, T_n, to segmentation resulting in S_n in reference image space

If **calculate directional growth**

    Identify minimum and maximum indices of segmentation for X, Y, and Z axes in reference segmentation S_1

    For N-1 segmentations

        Identify minimum and maximum indices of segmentation S_n for X, Y, and Z axes

        Take difference between results and reference values

        Multiply by corresponding spacing obtained from reference segmentation

    Print out results to file

Figure 6-1: Longitudinal feature extraction GUI. A screenshot of the graphical user interface designed within 3D Slicer for longitudinal feature extraction. The number of images is variable and renders the number of dialog boxes for input. This corresponds to the left most panel in 3D Slicer with windows for image viewing and rendering in panels to the right.

Phantom generation: Phantom images were generated simulating two clinical progressions: the growth of a tumor in the upper left lung and the progression of a non-solid ground glass lesion to the development of a solid component. A previously acquired chest-abdomen-pelvis CT scan from a single subject was chosen as the first imaging time point. For the simulated tumor component, a mask was created identifying the size, location, and shape of a pseudo-tumor in the upper left lung. This was repeated two more times with the masked region increasing in size simulating growth. Intensities corresponding to fat were inserted into the corresponding region to model a tumor using equation (6-1) where I_{tumor} corresponds to the resulting image with the pseudo-tumor composed of the original image, $I_{original}$, and fat intensities, I_{insert}, using the created mask, M_{tumor}.

$$I_{tumor} = I_{original} * inv(M_{tumor}) + I_{insert} * M_{tumor} \qquad (\text{ 6-1 })$$

This process was repeated to generate the development of a part-solid lesion in the upper right lung. To simulate an original non-solid lesion, original lung intensities were adjusted to zero, multiplied by three, readjusted by the same factor and inserted into a corresponding masked region, I_{insert}. A solid component was added to the non-solid lesion by incorporating intensities corresponding to muscle, I_{insert}, in a similar manner for the last two simulated time points. This process resulted in 4 time points, illustrated in Figure 6-2, labeled as time point 1-4. Transforms were then applied to each pseudo image, modeled after the transforms observed in CHAPTER 5: MULTI-LEVEL REGISTRATION, resulting in a phantom longitudinal dataset with tumor growth.

Propagated volume of interest – ground glass lesion: Three volumes of interest were segmented via the draw tool in the Editor module in 3D Slicer corresponding to a normal lung region, a non-solid component, and the solid component within the part-solid lesion in the upper right lung of the fourth generated time point. Images and transforms, obtained using the multi-level registration algorithm, were input into the created extension with the fourth time point as the reference image. The defined segmentations were propagated to all other images through the application of the transform from the reference image space to each individual image; this corresponded to the inverse of the transform acquired during registration. Segmentations were then associated with the appropriate image and basic imaging features were acquired, including volume, mean intensity, standard deviation of intensities, and minimum and maximum intensities, from each segmentation and image pair in its corresponding image space. Trends were observed

to demonstrate change in the simulated diseased region across time points including features prior to disease development compared to features obtained from normally appearing lung tissue.

Independent segmentations – solid tumor: Individual segmentations were acquired isolating the solid tumor in the upper left lung in time points 2-4. The segmentation from the second time point was propagated back to the first time point to identify the region corresponding to pre-tumor development. Segmentations were associated with the appropriate image and intensity features were acquired as listed above. Basic shape features were also identified through finding the extent of the tumor in reference image space. This was accomplished through the application of the transform from each image to the reference image space on the segmentation. The directional extent of the transform was then identified and comparative growth in each direction in reference image space was reported. As a baseline metric, the RECIST diameter was independently acquired in all images prior to registration. Following registration, regional diameters were acquired tracking the RECIST diameter across all images corresponding to the second and fourth time points to assess growth of the tumor in a single plane.

6.3 Results

Normal intensities, determined to be in a range of -921 HU to -679 HU with an average value of -879.62 ($\pm$ 23.09) HU, were consistently identified across all images and all regions in the first time point, illustrated in Figure 6-2 and quantitatively described in Figure 6-3. In comparison, the part-solid lesion in the upper right lung showed an increase in density to -614.00 ($\pm$ 72.89) HU in the second time point corresponding to a non-solid lesion. Values in that region remained relatively stable at -590.75 ($\pm$ 55.03) HU at time point 3 and -594.54 ($\pm$ 65.79) HU at time point 4. Within the solid component of the ground glass lesion, a shift was similarly detected in the second time point with average intensities of -642.42 ($\pm$ 56.16) HU prior to formation of the solid component. Formation of the solid component showed increasing density with average intensities of -28.98 ($\pm$ 127.30) HU at time point 3 and 39.33 ($\pm$ 38.60) HU at time point 4.
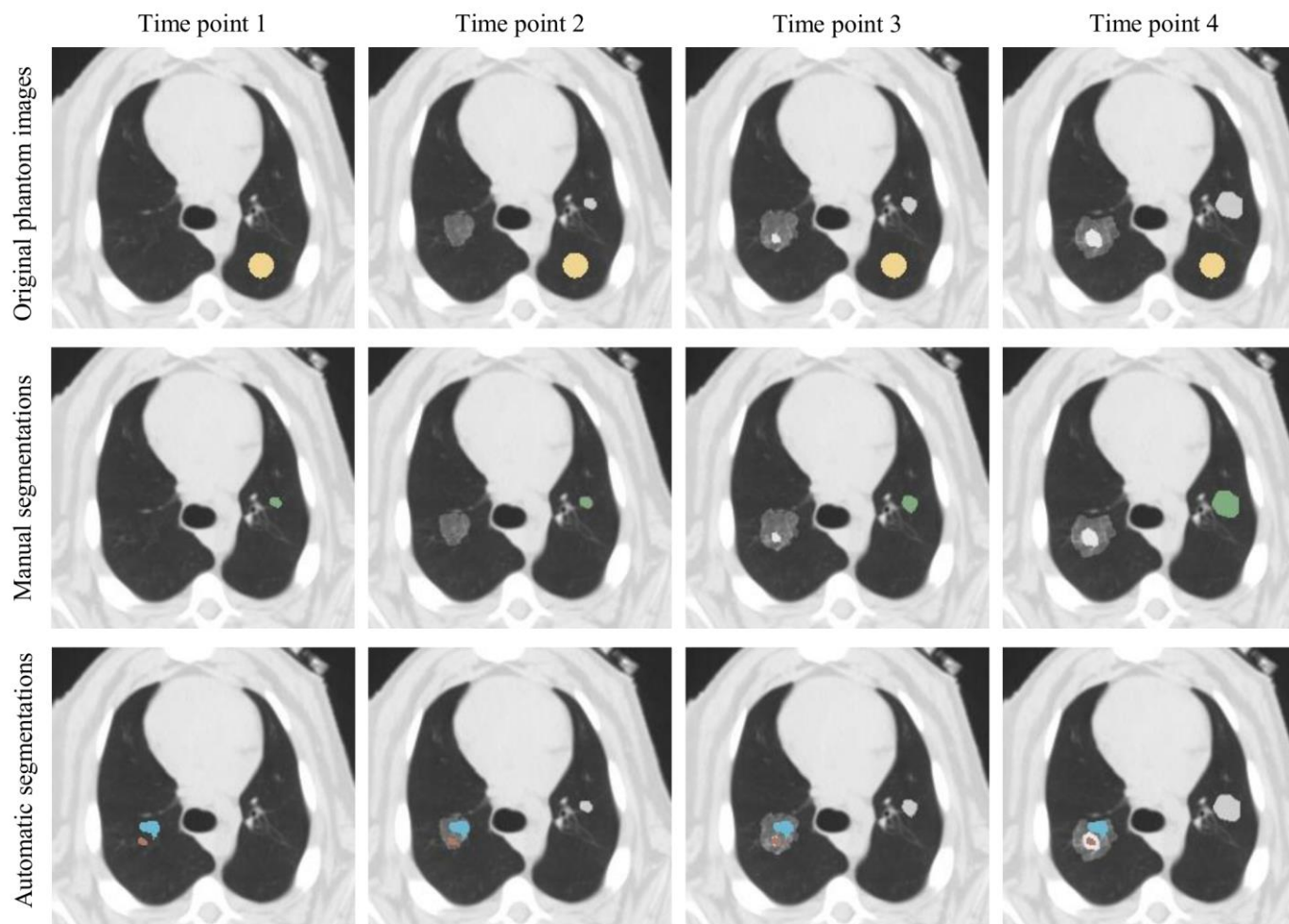
Figure 6-2: Generated phantom and segmentations. The generated phantom CT data (top row) illustrating the pseudo-tumor growth in the upper left lung, the ground glass lesion in the upper right lung and the normal lung region of interest (yellow). Individual segmentations (middle row, green regions) of the simulated tumor in each image. Automatically identified segmentations (bottom row) in the ground glass lesion corresponding to the solid component (red) and the non-solid component (blue)
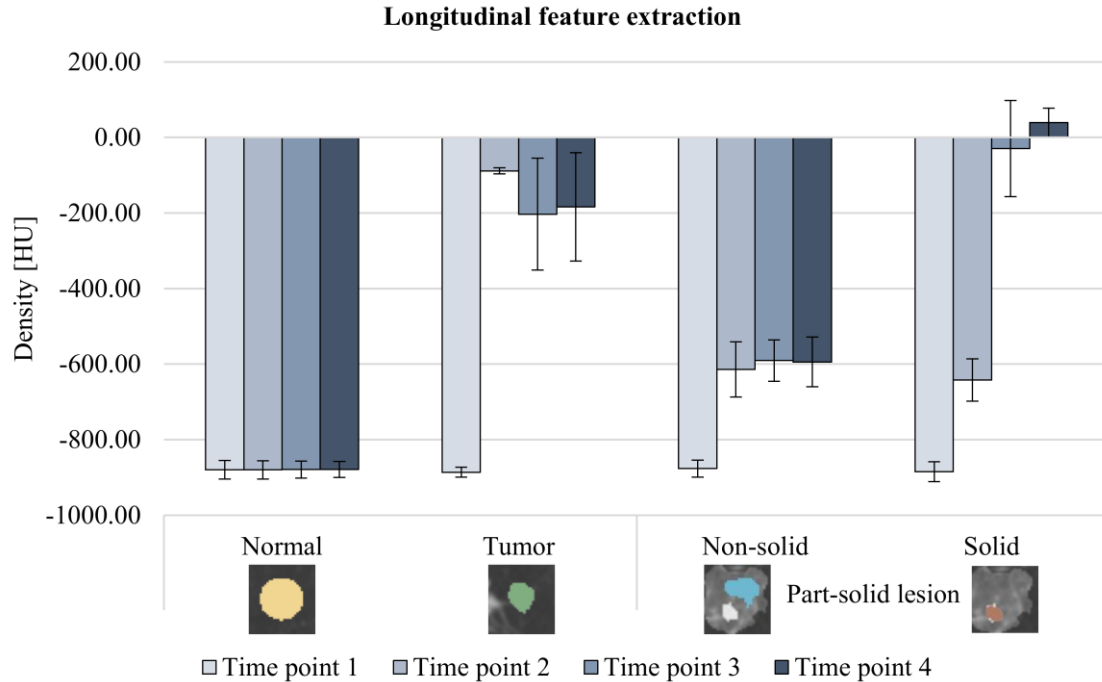
Figure 6-3: Longitudinal feature extraction. Graphical display of the mean intensity and standard deviation extracted from normal lung tissue, the independent segmentations for the simulated tumor in the upper left lung, and the propagated segmentations from the ground glass region in the upper right lung showing a region progressing from a non-solid to a solid.

Focusing on the features obtained from the simulated tumor in the upper left lung, seen in Figure 6-2, a shift was observed with an average value of -886.56 (± 13.13) HU in the original image without the presence of a tumor to -88.36 ± 7.83 HU after the placement of the tumor, shown in Figure 6-3. Subsequent time points showed an additional shift to -202.92 (± 148.44) HU in time point 3 and -183.57 (± 143.35) HU in time point 4 as seen in Figure 6-3. Comparing volumes, the tumor doubled in size between the second (0.329 mL) and third (0.721 mL) time points, and again tripled between the third and fourth (3.068 mL) time points for approximately 10 times growth overall.

As shown in Table 6-2, the RECIST diameter was measured across multiple slices isolating each simulated tumor ranging from 7.1 mm to 17.6 mm for a total estimated growth of 10.5 mm in the axial plane. Following registration, the slice corresponding to the RECIST diameter from time point 2 showed a range of 7.1 mm to 14.9 mm in growth, while the slice corresponding to the RECIST diameter from time point 4 showed growth from 6.7 mm to 17.6 mm. Comparing directional growth, minimal growth occurred in the axial plane (± X and ± Y growth) between time point 2 and 3 as seen in Table 6-3 with a total growth of approximately 2 mm in both directions. Greater growth was observed between time points 2 and 4 in the axial

plane with total growth of approximately 9.0 mm in both directions. This change is reflected by the RECIST diameter; however, we can see that growth occurred more in the +X and -Y directions as demonstrated in Figure 6-4. In addition, growth in the ± Z directions was calculated where we see greater growth in the -Z direction toward the base of the lungs as illustrated in Figure 6-4.

Table 6-2: RECIST measurements. The RECIST measurements obtained from the largest axial cross-section chosen independently without registration of the time points and corresponding measurements following the largest axial diameter of the tumor from time point (TP) 2 and TP 4 post-registration.

	Slice	Time point 2	Time point 3	Time point 4
Pre-registration				
RECIST	Various	7.1	9.7	17.6
Post-registration				
Following RECIST (TP2)	193	7.1	8.7	14.9
Following RECIST (TP4)	191	6.7	9.6	17.6

Table 6-3: Directional growth measurements. Directional growth measures acquired from the registered manual segmentations in the reference image space.

TP	-X growth	+X growth	-Y growth	+Y growth	-Z growth	+Z growth
2	0	0	0	0	0	0
3	-0.69	1.39	1.39	-0.69	0.00	-6.00
4	-3.47	5.55	6.24	-2.77	3.00	-9.00
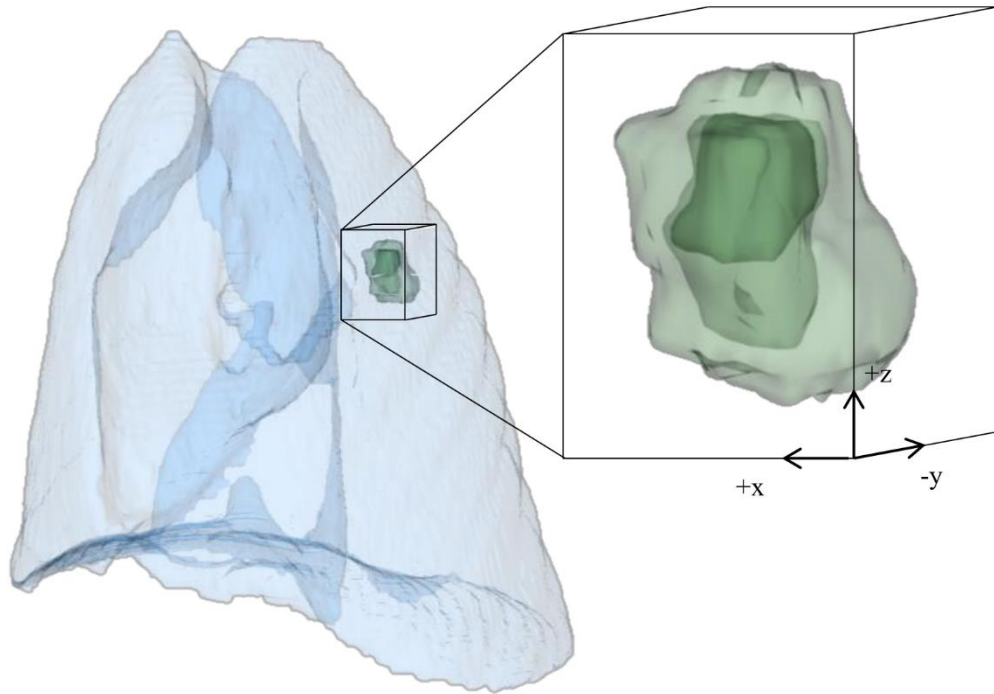
Figure 6-4: Directional growth of simulated tumor. Rendering of tumor located inside the lungs with corresponding coordinate system used in determining directional growth.

6.4 Discussion

The ability to extract longitudinal features from a series of images that have been previously aligned allows for the inclusion of directional growth and the investigation of imaging features throughout cancer progression. Previous work has been done monitoring volumetric change and intensity mapping over time applied to brain tumors [42]. In this work, we focus on the extraction of basic imaging features and the addition of global directional growth. This was demonstrated with the development of a 3D Slicer extension and application to a generated phantom dataset to simulate the growth of two disease processes in the upper right and left lung.

Significant work has been done developing feature extraction and classification methods, or computer-aided diagnosis tools, for determining the likelihood of malignancy for a large number of cancers [128]. We have presented the ability to extract basic intensity features in longitudinal datasets through the identification of a consistent segmented region across datasets. These basic intensity features were initially chosen due to their current integration into 3D Slicer. Further expansion to include histogram, tumor shape, and texture features analyzed across a longitudinal dataset may further improve the ability to non-invasively characterize detected

tumors. We believe the inclusion of longitudinal analysis will particularly benefit analysis of transitions from non-solid to solid tumors in the development of lung cancer as demonstrated in this phantom dataset [129, 130]. In these instances, borders are not clearly defined, but rather specific tracking of a sub-segmental region with feature and texture analysis may be performed with our developed tool.

We showed the potential for detecting precursor imaging features through the identification of the simulated tumor location in the pre-disease image with both disease processes. Early detection of cancer increases the 5-year survival rate across all types of cancer [131]. It is well known that tumors are composed of a wide variety of tissue and typically encourage the development of angiogenesis and other cellular processes [132, 133]. Previous work has shown that image feature extraction and texture analysis including the tissue surrounding lung nodules [49] and breast microcalcifications [134] have proven useful in the diagnosis of cancer suggesting detection of lesion interaction and invasion into the surrounding tissue.

Minimal limitations were placed on the selection of transform associated with each image to allow for the use of any registration algorithm. Due to the desire to acquire quantitative features in each individual image space, the transform must be inverse consistent, a characteristic of most biologically relevant transforms [135]. It is noted that the accuracy of the transform in aligning the images is important in extracting accurate features. With the integration into the 3D Slicer framework, any segmentation can be easily edited using the Editor module [74, 136]. In addition, more advanced segmentation algorithms, such as region growing, may be incorporated to provide automatic segmentation of tumors using our tool for automatic identification of an initial starting point across longitudinal images [137].

Lastly, we demonstrated the ability to track directional growth of tumors through a simple analysis by comparing the extent of the registered tumors over time. It is well established that limitations of the RECIST measurement include lack of volumetric information and the use of subjective one-dimensional measurements [138]. Automatic measurements allow for a more objective approach and can easily incorporate growth in multiple dimensions. Volumetric analysis has been explored to improve the assessment of tumor burden [39, 42, 45, 125-127]. Beyond volume, analysis of the Jacobian following non-rigid image registration has also been explored for breast cancer tumors as a potential biomarker for predicting response in treatment [44]. Additional growth patterns, symmetrical/asymmetrical and directional growth toward

vessels/lymph nodes may provide further information about malignancy, aiding non-invasive risk assessment and/or refined treatment selection.

CHAPTER 7: LI-FRAUMENI

7.1 Introduction

Li-Fraumeni is a condition found in humans that is identified by a germline mutation in *TP53*, tumor protein 53. This mutation results in a strong predisposition to tumor development as normal functioning *TP53* is essential in halting the cell cycle for DNA repair and initiating apoptosis in cells that fail to repair damaged DNA. The overall risk of cancer developing in human carriers of this mutation is 75% in males and 93% in females with an overall 40% risk of cancer developing within the first 20 years of life [139]. This mutation has been commonly seen in a variety of human cancers [140] and targeted *TP53* mouse models have been shown to develop a wide range of tumors including carcinomas, soft tissue and osteosarcomas, leukemia, and glioblastoma multiform [141-144].

A genetically modified Yucatan miniature pig model with Li-Fraumeni syndrome was created with both heterozygote ($TP53^{R167H/+}$) and homozygote ($TP53^{R176H/R176H}$) mutations by Exemplar Genetics (Sioux Center, Iowa). Gene targeting was used to introduce a R167H missense mutation in the endogenous *TP53* gene. *TP53* targeted pigs were generated through somatic cell nuclear transfer, in which the *TP53* targeted vector was introduced into a pig fetal fibroblast, inserted into harvested oocytes, and the resulting embryos transferred to a recipient sow producing heterozygote piglets. Of the heterozygote animals, a cohort was used for disease monitoring and a cohort was bred to produce homozygote animals.

This chapter presents the application of the methods described in CHAPTER 3: LONGITUDINAL MEDICAL IMAGE ACQUISITION for non-invasive characterization of this model. Due to the possibility of a wide range of cancer development, whole-body disease monitoring was required to determine the genotype to phenotype relationship. Data obtained from the heterozygote animals has previously been shown in CHAPTER 3: LONGITUDINAL MEDICAL IMAGE ACQUISITION. Additionally, a full characterization of this model, including genetic and molecular analysis, can be seen in Sieren, et al. [63].

7.2 Materials and methods

Image acquisition: A cohort of 6 heterozygote animals and 5 homozygote animals were imaged for disease characterization using the image protocol acquisition methods described in CHAPTER 3: LONGITUDINAL MEDICAL IMAGE ACQUISITION. Heterozygote animals were imaged at intervals over 3 years to assess the development of disease. In comparison, homozygote animals were imaged upon indication of clinical signs, including palpable lymph nodes, abnormal blood work, and physical/behavioral abnormalities. A selection of the whole-body protocols, listed previously in Table 3-1 and Table 3-2, were acquired for each animal at each screening time point. Upon detection of disease, additional targeted scans were acquired with protocols listed in Table 7-1.

Table 7-1: Targeted brain MRI protocols for the homozygote TP53$^{M/M}$ model. Parameters for MRI developed for a 3-Tesla TIM Trio scanner. Scans were acquired for targeted imaging of a cranial bone lesion.

	3D SPACE (post-contrast)	T1 Axial	T1 Sagittal/Coronal
Scanning sequence	Spin echo	Spin echo	Spin echo
Acquisition type	3D	2D	2D
Repetition time (msec)	1630	600	600
Echo time (msec)	119	7	7.4
Flip angle (º)	120	70	70
Echo train length	141	1	1
Slice thickness (mm)	0.9	4	4
In-plane resolution (mm)	0.86 x 0.86	0.625 x 0.625	0.47 x 0.47
Acquisition matrix	256 x 194	384 x 269	512 x 256
Number of Slices	96	19	20
Approx. Scan time (min:sec)	7:50	2:40	2:35
Respiratory management	None	None	None

Structured reports: Structured reports, described in CHAPTER 4: STRUCTURED REPORTING, incorporating whole-body disease development, were used for longitudinal qualitative data collection. All scans were read by a radiologist and disease findings were recorded. The RECIST diameter, imaging characteristics, and anatomic location were identified for each detected tumor.

Registration: Detected tumors were registered over all available time points using the multi-level registration algorithm. Subsequent CT acquisitions were registered to the first CT

acquisitions and MRI acquisitions were registered to CT acquisitions acquired during the same imaging study. Up to three levels of registration were used as described in CHAPTER 5: MULTI-LEVEL REGISTRATION as appropriate for the location of the tumor.

      Feature extraction: Quantitative features were extracted for identified tumors using the methods described in CHAPTER 6: LONGITUDINAL FEATURE EXTRACTION. Tumors were manually segmented and volume and intensity features were extracted and directional growth was identified where applicable. Additional quantitative features were identified in the liver and spleen of each animal. Each organ was manually segmented, excluding major vessels, using the Pulmonary Analysis Software Suite [115] with the contrast enhanced abdominal CT scans. Volume and intensity features (minimum, maximum, mean, and standard deviation) were extracted. To assess contrast clearance in the abdominal MRI contrast enhanced VIBE sequence, regions of interest were identified in each scan of the sequence corresponding to the same tissue region. Intensity features were extracted and values were normalized to an equivalent sized region in the muscle to standardize across and within subject for final evaluation. Relevant measures were tracked by time and weight to give insight into potential disease markers.

Table 7-2: Li-Fraumeni imaging time points. The imaging time points acquired for characterization of the Li-Fraumeni TP53 heterozygote (M/+) and homozygote (M/M) model. An X indicates imaging occurred, a capital N indicates imaging occurring followed by necropsy within 24 hours, and a lowercase n indicates necropsy occurred without any imaging. Purple indicates that both CT and MRI were acquired where blue indicates only CT was acquired.

TP53^{M/+}

Model	Subject	2011 J	A	S	O	N	D	2012 J	F	M	A	M	J	J	A	S	O	N	D	2013 J	F	M	A	M	J	J	A	S	O	N	D	2014 J	F	M	A	M	J	J	A	S	O	N	D	2015 J-D	2016 J	F	M	Necropsy Diagnosis
TP53^{M/+}	Het 1		B														X		X		X		X		X							X														n			
	Het 2		B																X		X		X									X														n			
	Het 3		B																X		X		X									X														n			
	Het 4		B														X		X		X		X		X							X														N			
	Het 5		B														X		X		X		X		X							X														N			
	Het 6		B														X		X		X		X		X							X								N									

TP53^{M/M}

Model	Subject	2012 J	A	S	O	N	D	2013 J	F	M	A	M	J	J	A	S	O	N	D	2014 J	F	M	A	M	J	J	A	S	O	N	D	2015 J	F	M	A	M	J	J	A	S	O	N	D	2016 J-D	2017 J	F	M	Necropsy Diagnosis
TP53^{M/M}	Hom 1		B							X					n																																	Lymphoma
	Hom 2		B											N																																		Osteosarcoma
	Hom 3		B											X		N																																Osteosarcoma
	Hom 4																B											N																				Lymphoma
	Hom 5																		B										N																			Lymphoma

7.3 Results

Het 1-6 were imaged for 4-7 time points ranging from 12 months of age to 51 months of age reviewed in Table 7-2. MRI and CT acquisitions were acquired at 12, 14, 16, 18, and 27 months of age. Additional CT acquisitions were acquired at 21, 36, and/or 52 months for a subset of animals. Following data analysis, no spontaneous tumors were identified among heterozygote animals; therefore, acquired datasets were utilized for tool development as previously described in CHAPTER 3: LONGITUDINAL MEDICAL IMAGE ACQUISITION and as baseline measures for the phenotype. Disease was identified and pathologically confirmed in all homozygote animals within 15 months of age with 1 to 2 imaging time points acquired per animal as seen in Table 7-2. Lymphoma was observed in 60% (3/5), osteosarcomas in 40% (2/5), and an additional Wilm's tumor in 20% (1/5).

Imaging for subject Hom 1 occurred at 6 months of age, 4 months prior to necropsy and diagnosis of lymphoma. Mildly enlarged to enlarged (RECIST >10 mm) lymph nodes were observed throughout the abdomen. An abnormal soft tissue mass (RECIST: 8.3 cm) with an undefined border was indicated near the right shoulder with a hyper-intense signal seen in the corresponding MRI head scan. Liver and spleen volumes from the heterozygote cohort were used to calculate baseline trends showing R^2 values of 0.8 and 0.84 for liver and spleen volumes, respectively, seen in Figure 7-1. Comparison with subject Hom 1 revealed an enlarged liver (predicted = 584.3 mL vs. 923.3 mL) and a mildly enlarged spleen (predicted = 499.8 mL vs. 532 mL) given the weight of the animal.

At 4 months prior to necropsy, minimal differences were observed in quantitative measures comparing liver and spleen values in the acquired MRI contrast-enhanced abdominal sequence for subject Hom 1 and the heterozygote cohort. Quantitatively, organ to muscle ratios were lower than those observed in the heterozygote cohort; however, ratios showed the same contrast enhancement pattern in the dynamic VIBE series. Heterogeneity measures also followed the same patterns seen in the heterozygote cohort with similar values.

Imaging occurred at 11 and 9 months of age for subjects Hom 4 and Hom 5, respectively. Advanced diffuse disease was identified following the same pattern of enlarged lymph nodes, spleen, and liver volumes and was pathologically confirmed as lymphoma. Due to scanner availability, MRI protocols were not obtained for subject Hom 4 and 5.

Volume vs. Weight
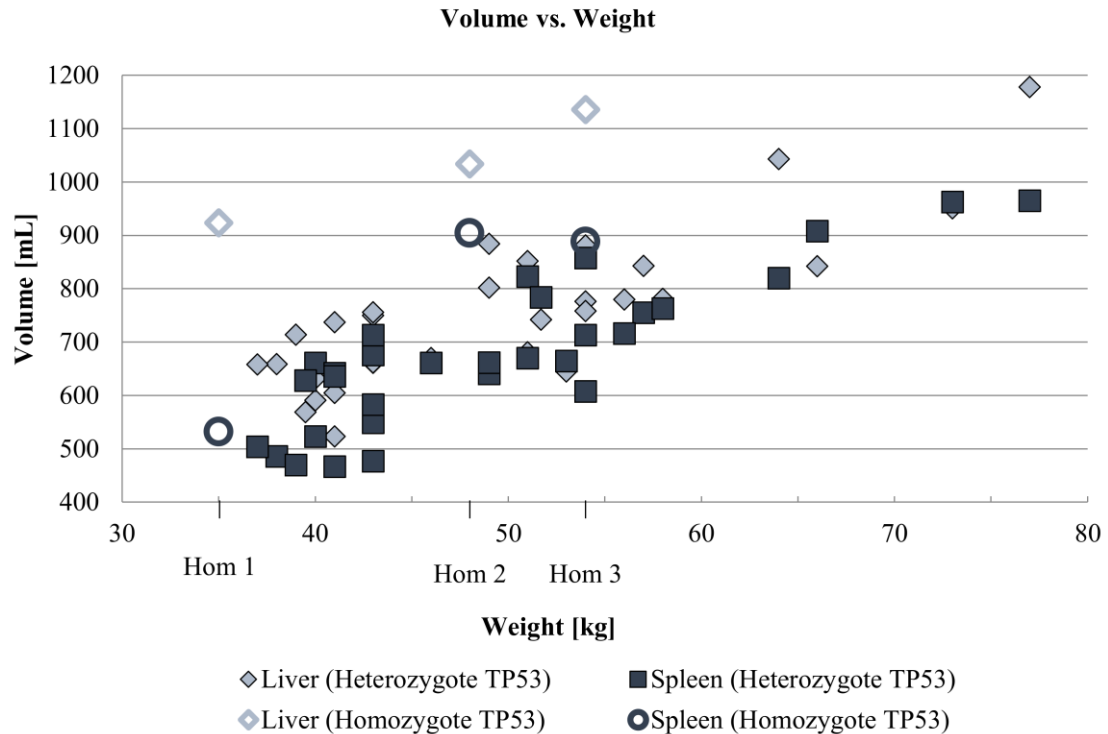
Figure 7-1: Liver and spleen volumes. Scatter plot of the liver and spleen volumes versus the corresponding weight of each animal. Elevated liver volumes are seen in subject Hom 1 demonstrating early indications of lymphoma.

Two spontaneous cranial osteosarcomas were observed in subjects Hom 2 and Hom 3 with multiple peripheral lesions identified in the tibia, femur, and sacrum. CT and MRI revealed a 28 mm right parasagittal, calvarial lytic (110 HU) tumor in subject Hom 2 illustrated in Figure 7-2A. The tumor expanded into the cranial cavity with additional destruction of adjacent bone tissue. SPACE T2 MRI images showed an isointense tumor compared to the soft tissue of the brain. An additional post-contrast T1 head acquisition was obtained showing minimal contrast enhancement observed.

Hom 3 was imaged at two screening time points at 12 and 14 months of age. Initial screening showed normal appearance of the brain, cranium, and frontal sinuses; however, peripheral lesions were identified in the long bones. At the second screening (51 days post initial screening) a 39 mm osteolytic (367 HU) tumor was detected with infiltration into the cranial cavity and frontal sinuses. MRI presentation revealed a hypo-intense signal in the T2 SPACE acquisition. Additional post-contrast T1 head acquisitions were acquired showing enhancement in the tumor. The identified peripheral lesions ranged from 8 to 18 mm presenting lytic lesions and heterogeneous hyper-dense lesions.

Multi-level registration was performed between the two acquired time points to align the tumor using two levels of registration. Due to the appearance in only one time point, visual inspection was performed to compare the tumor across all acquired datasets as seen in Figure 7-2B.

An additional renal tumor was located with CT and MRI in subject Hom 3, identified as Wilm's tumor upon histopathologic diagnosis, illustrated in Figure 7-2C. The tumor was located in the right cranial pole of the kidney. Initial identification showed two components to the tumor (32.3 mL): solid (RECIST: 25.8 mm, 8.9 mL) and hemorrhagic (23.4 mL) components. The hemorrhagic component appeared hypointense under T2 imaging, while the T1 pre-contrast VIBE showed a hyperintense signal. The solid component of the tumor was isointense under T1 weighting with a heterogeneous enhancement pattern throughout the tumor observed in T2 imaging and throughout the dynamic T1 sequence post-contrast. At the second screening, the hemorrhagic component appeared to be resolved while the solid component of the tumor remained. Minimal changes in size were observed of the solid component with a decrease in mean CT attenuation (62 to 55 HU). Tumor characteristics showed a hypointense signal in the T1 pre-contrast VIBE with greater exaggeration of the hypointensity upon the delivery of contrast. T2 characteristics also changed showing an iso to hyperintense signal compared to a hypointense signal seen previously. Characterization is summarized in Table 7-1.

Multi-level registration was performed with three levels of registration. Tumors were segmented individually and extend of growth was determined. The resolve of the hemorrhagic component accounted for much of the change in growth; however, the tumor grew or shifted 4.5 mm to the top of the kidney.

Table 7-3: Wilm's tumor characteristics. CT and MRI characteristics of the kidney tumor identified in subject Hom 3.

Time point	Component	Volume [mL]	Mean [HU]	Standard Deviation [HU]	T2 intensity	T1 (VIBE) intensity
1	Solid	8.9	61.5	24.8	Heterogeneous	Isointense/ Heterogeneous
	Hemorrhagic	23.4	58.8	26.8	Hypointense	Hyperintense
2	Solid	7.1	54.9	28.3	Iso/ Hyperintense	Hypointense
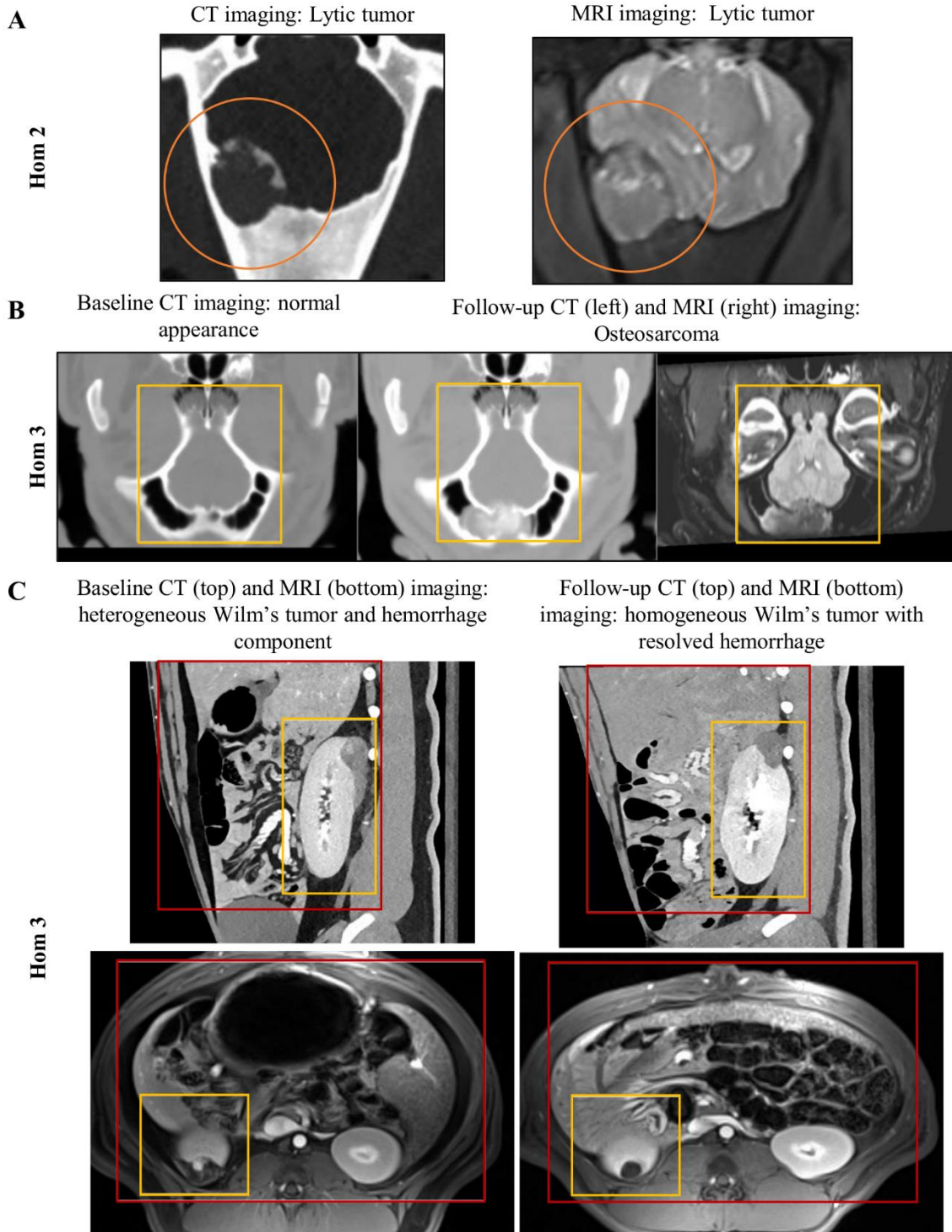
Figure 7-2: Detected tumors. (A) The lytic tumor located in the skull of subject Hom 2 showing a hypo-intense tumor in CT and an iso-intense tumor in MRI. (B) The tumor identified in subject Hom 3 in CT prior to development (left) and 51 days later (middle) with corresponding MRI (right). The yellow box indicates the region of interest used during multi-level registration for volume reduction. (C) The Wilm's tumor from subject Hom 3 see in CT (coronal, top) and MRI (axial, bottom) at the first imaging time point (left) and the second imaging time point (right). Red and yellow boxes indicate the regions of interest used during multi-level registration for volume reduction.

72

7.4 Discussion

We have presented the characterization of a heterozygote and homozygote *TP53* animal model of disease using the developed methods described in CHAPTER 3 – CHAPTER 6. Heterozygote models did not develop tumors within the project time frame (4.25 years) and were used as a baseline measure for the phenotype. A total of 3 tumors were identified in two homozygote animals and qualitatively characterized using structured reports. Due to their heavy involvement in detoxifying and filtering the blood, quantitative characterization of the liver and spleen was focused upon. Indicators of disease in these organs have previously been noted by the heterogeneity of the liver and the size of the spleen [145-147]. Lastly, we demonstrated the performance of the multi-level registration algorithm for the alignment of a cranial osteosarcoma and a kidney lesion in two time points of a longitudinal dataset.

Mutations in the *TP53* gene are seen in approximately 50% of all human cancers [148]. Protein 53 (p53), encoded for by the *TP53* gene, plays an important role in tumor suppression mainly through signaling for apoptosis, or cell death, in the event of damaged DNA. All homozygote animals showed the development of lymphoma, osteosarcoma, and/or nephroblastoma (Wilm's tumor); cancers commonly observed in mouse models of Li-Fraumeni [149] and human cohorts [139, 150]. In all instances imaging was beneficial in detecting disease showing early indicators of lymphoma development, development of skeletal lesions, and progression of a kidney tumor. Due to scanner availability, MRI was only acquired for two homozygote animals (Hom 2, Hom 3) presenting cranial tumors and kidney tumor and provided additional targeted characterization for identified tumors. For the kidney tumor, MRI imaging characteristics were consistent with previously reported observations regarding Wilm's tumor presentation as diagnosed at necropsy [151]. For all homozygote animals, detection of tumors aided in the timing of necropsy and guidance of tissue collection for histopathological examinations. In these cases, volume rendering was advantageous, specifically using CT due to the acquisition of isotropic voxels providing fine detail.

In addition to imaging, the developed registration and quantitative feature extraction methods were used for characterization of this animal model. The lack of tumor development in the heterozygote animals provided a baseline for organ development revealing elevated liver volume as an early indicator of lymphoma in subject Hom 1. Multi-level registration was used to visually demonstrate tumor progression for subject Hom 3. In both instances, visualization of the significant disease change was possible with the rigid transform. Additionally, MRI to CT registrations were beneficial in highlighting the differences in distinguishing components of the

tumor for both imaging modalities. Quantitative features were acquired in both modalities. In CT, these measures related to density of the tissue, such that 0 HU corresponds to the density of water and -1000 HU to the density of air. MRI features were normalized to values obtained from a same sized region in the muscle to compare acquired values across subjects [152, 153].

While cancer development was seen in all five homozygote animals, there are limitations with this model. We focused our efforts on developing methods to determine the genotype to phenotype as demonstrated by the use of the heterozygote data in CHAPTER 3 – CHAPTER 6. This resulted in a small number of animals presenting a limited number of cancers. Mouse models with similar genetic background have demonstrated early development of lymphoma in addition to a wide range of sarcomas and carcinomas [143]. In human cohorts, breast carcinomas are the most frequently observed tumor types, which was not detected in this cohort. Additionally, detected cancers in homozygote animals were imaged upon clinical indications limiting our ability to longitudinally monitor cancer development as demonstrated with the heterozygote cohort. Disease was seen in all homozygote animals within 18 months of age (1.5 years) presenting a feasible research timeline. As more animals are monitored, we expect to see similar trends with presentation of additional cancers common to the *TP53* family. After 51 months (4.25 years), no spontaneous tumors were found in the heterozygote animals. While we do expect tumors to eventually develop in animals with this genetic background, this extended window presents the opportunity to introduce additional exposures to encourage targeted tumor development.

CHAPTER 8: CRYSTALLINE SILICA EXPOSURE MODEL

8.1 Introduction

Lung cancer is the leading cause of cancer related deaths with a five-year survival rate of 17.8% with minimal improvement seen in the last 30 years despite major scientific advancements [154]. *TP53* mutations are commonly associated with lung cancer [155], suggesting a promising background for the promotion of lung cancer development. Crystalline silica (alpha quartz) as an environmental exposure has been shown to induce lung cancer in both animal studies [156, 157] and human studies [158, 159]. It has also been shown to induce pulmonary inflammation, progression fibrosis, airway wall thickening, and nodules; conditions that are noted by structural changes in the lungs identified by medical imaging [160, 161]. Given the *TP53* genetic background of the animal models developed by Exemplar Genetics (Sioux Center, Iowa), this chapter presents characterization of a $TP53^{R167H/+}$ animal model with additional exposure to crystalline silica in the lungs. Characterization of this model has also been reported in Hammond, et al [99].

8.2 Materials and methods

Model generation: To induce silicosis in the lungs, a subset (n = 3) of the Li-Fraumeni $TP53^{R176H/+}$ heterozygote disease monitoring cohort animals were exposed to alpha quartz. Medium grain quartz foundry sand was ground to micron-sized (<4µm) dust using a ball mill (Retch, Inc., MM-400). Samples of 250 mg were weighed into clean borosilicate glass vials into which 5 mL of sterile 0.9% saline was pipetted. Samples were vortexed prior to loading into a syringe for instillation in a targeted region of the lungs. Silica was injected in the right upper lobe through the right apical bronchus with the aid of a bronchoscope and flushed with 2 mL of saline. Confirmation of the location post-injection was achieved with a CT scan.

Image acquisition: A cohort of 6 animals, 3 exposure and 3 controls, were imaged for disease characterization using the image acquisition methods described in CHAPTER 3: LONGITUDINAL MEDICAL IMAGE ACQUISITION. Focus was placed on imaging the lungs for disease development. In summary, chest CT scans were obtained with a 128-multidetector dual-source scanner (SOMATOM Definition Flash, Siemens Healthcare, Forchheim, Germany) to assess lung density and anatomical detail (210mAs and 120kV, a rotation time of 0.5 second, pitch of 1 and, a CTDIvol of 14.2 mGy). No resultant effects were observed from this exposure,

which is slightly higher than a standard clinical high resolution chest protocol and less than a CT angiography exam. Scans were acquired at an inspiratory breath-hold of 20 cmH$_2$O following 2 minutes of pulmonary recruitment at an equivalent PEEP. Reconstructions were performed with a standard body kernel at slice thicknesses of 0.75 mm for quantitative analysis.

Chest MRI scans were acquired with a 3-Tesla MRI system (TIM Trio 3T, Siemens Healthcare, Forchheim, Germany) with standard surface coils. Turbo spin echo T2-weighted scans (TR of 5280 ms, TE of 156 ms, flip angle of 120°, and echo train length of 109) acquired in the axial and coronal planes were used to assess areas of increased fluid content, such as tumor development or inflammation. Five mm slice thicknesses were acquired with 1.4 mm x 1.8 mm and 1.5 mm x 2.0 mm in-plane resolution for the axial and coronal scans respectively. Respiratory gating was accomplished during this MRI sequence by using navigator echoes to eliminate respiratory induced motion artifacts. An additional post-contrast 3D single breath hold T1-weighted VIBE thoracic MRI scan (TR of 4.3 ms, TE of 1.92 ms, flip angle of 12°) was acquired post intravenous administration of 0.2 mL/kg gadolinium (Magnevist, Berlex Inc, Wayne, NJ) for increased anatomical detail in the lungs. In-plane resolutions of 1 mm x 1.8 mm were acquired at slice thicknesses of 3 mm. Breath-holds at an inspiratory pressure of 20 cm H$_2$O were used to reduce motion artifact for all VIBE scans. Parameters for all scans were previously reported in Table 3-1 and Table 3-2.

Structured reports: Structured reports incorporating lung disease development were used to provide consistent and complete visual interpretation of the lungs and surrounding anatomies. Each structured report included the assessment of the diagnostic quality of the scan and targeted anatomic structures of interest. The anatomic structures of interest included the large airways, pleura, heart and pericardium, mediastinum and hila, chest wall and lower neck, vessels, and bones. Within the lungs, a total of eleven conditions were prompted for within each lobe of the lungs to note presence or absence. These included consolidation, bronchiectasis, atelectasis, bronchial wall thickening, ground glass opacities, linear opacities, nodules, emphysema, cysts, reticular abnormalities and honeycombing. The RECIST diameter, imaging characteristics, and anatomic location were identified for each detected nodule. All scans were read by an experienced chest radiologist and indicators of disease were recorded.

Registration: Multi-level registration was performed focusing on the upper right lung corresponding to the location of crystalline silica injection. All CT scans were registered to the first CT acquisition prior to injection. Acquired MRI images were registered to CT scans obtained

at the equivalent time point. A total of three levels were used corresponding to whole image acquisition, the lungs, and the upper right lung.

Feature extraction: Quantitative analysis of the CT data focused on the right cranial lobe of the lung to assess disease progression in the airways and surrounding lung parenchyma related to the silica exposure. A cylindrical region of interest was placed in the upper right lung isolating a non-defined region corresponding to the injection confirmation area. Equivalent regions were automatically propagated from the region placed in time point 1 across all datasets following registration. For comparison, manually placed regions were visually placed in all datasets. Features were extracted from both the propagated and manually placed regions and mean intensity trends were compared between control animals and exposure animals. To account for the variation in lung volume across and within subjects, density measures were normalized to the mean density of the entire lung. Trends were observed to indicate the presence of increased parenchymal density in exposure animals compared to control animals. Airway analysis was performed using the Apollo software (VIDA Diagnostics, Inc., Coralville, IA). Airways were automatically segmented and specific airways of interest were identified along the apical bronchial tree. The wall area fraction (wall area as a percent of the total airway area) was measured and compared across the first and last time point to assess change in the airways between the exposure and control cohorts.

Table 8-1: Crystalline silica exposure model imaging time points. The imaging time points acquired for characterization of the crystalline silica exposure model. An X indicates imaging occurred, S indicates crystalline silica exposure occurred immediately followed by imaging, a capital N indicates imaging occurring followed by necropsy within 24 hours, and a lowercase n indicates necropsy occurred without any imaging. Purple indicates that both CT and MRI were acquired where blue indicates only CT was acquired.

Model	Subject	2011						2012												2013												2014												2015	2016			Necropsy Diagnosis
		J	A	S	O	N	D	J	F	M	A	M	J	J	A	S	O	N	D	J	F	M	A	M	J	J	A	S	O	N	D	J	F	M	A	M	J	J	A	S	O	N	D	J-D	J	F	M	
$TP53^{M/+}$	Het 1			B													X	X		X	X				X							X													n			Control
	Het 2			B													X	X		X	X											X													n			Control
	Het 3			B													X	X		X	X											X													n			Control
$TP53^{M/+}$ + Silica	Sil 1			B													X	S		X	X				X							X													N			Silicosis
	Sil 2			B													X	S		X	X				X							X													N			Silicosis
	Sil 3			B													X	S		X	X				X							X								N								Silicosis

78

Figure 8-1: Crystalline silica exposure. Demonstration of the progression of disease in CT in the upper right lung of subject Sil 2 across all acquired time points shown in the orange circle.

8.3 Results

Exposure animals were imaged for a total of 7 time points ranging from 12 to 51 months reviewed in Table 8-1. CT and MRI were acquired for all animals at 12, 14, 16, 18, and 27 months of age. CT was additionally acquired for all exposure animals and a single control animal at 21 months and prior to necropsy for exposure animals at 36 and 51 months of age. An example of longitudinal CT imaging showing disease progression is displayed in Figure 8-1. The effects of silica instillation on the right cranial lobe generated findings during serial imaging of this cohort. Increased ground glass opacities and multiply small nodules (2-3 mm) at 21 months of age in subject Sil 3 were noted from the structured reports. Overall, the cranial lobes in both exposure and control animals had a high number of reported findings with multiple minor transient changes as previously reported upon in CHAPTER 4: STRUCTURED REPORTING; however, minimal differences were observed across cohorts in the number and type of condition noted.

Quantitative CT based density and airway measures were obtained to objectively compare the severity and progression of structural changes in exposure versus control cohorts. Analyzed airways and parenchymal regions of interest are displayed in Figure 8-2. Similar trends were identified with both manually placed and propagated regions as displayed in Figure 8-3A-B. Over the course of the study, CT assessed lung density was very stable in the control group, as reflected in the minimal ($\pm 2\%$) percent change from baseline, seen in both regions. Silica exposure was performed at 14 months and confirmed via a 14.8% and 14.1% increase in mean CT lung attenuation in the manually placed and propagated regions, respectively, in the targeted right cranial lung lobe of the exposure group. This immediate increase in density was caused by fluid deposition in this target region (saline suspension and flush). At subsequent time points, CT assessed lung attenuation remained elevated from baseline for exposure animals compared to controls, ranging from an increase in 2.2% at 14 and 16 months to 7.1% at 36 months seen in the propagated regions. Similarly, manual regions showed an increase in 1.8% at 14 months to 3.6% at 51 months.

For the quantitative assessment of CT based airway measures, the wall area fraction was determined by dividing the airway wall area by the outer (total) airway area for each target airway branch. Measures acquired at 15 months post exposure (cohort 27 months of age) were compared to pre-exposure, baseline measures (cohort 12 months of age) to observe changes over time. Here,

evidence of airway wall thickening was observed in the cranial lobe segmental airways (RB1-5 and RB1-6) in the exposure group, but not in the control group as seen in Figure 8-3C.

Pathological confirmation of silica deposits with corresponding fibrosis in the upper right lung was obtained for subject Sil 3 at 36 months of age and displayed in Figure 8-2. Necropsy occurred immediately following the final imaging time point with CT. Prosection of the lung was guided by the previously acquired MRI and CT images through three plane viewing and volume rendering to gauge correspondence between and within structures.
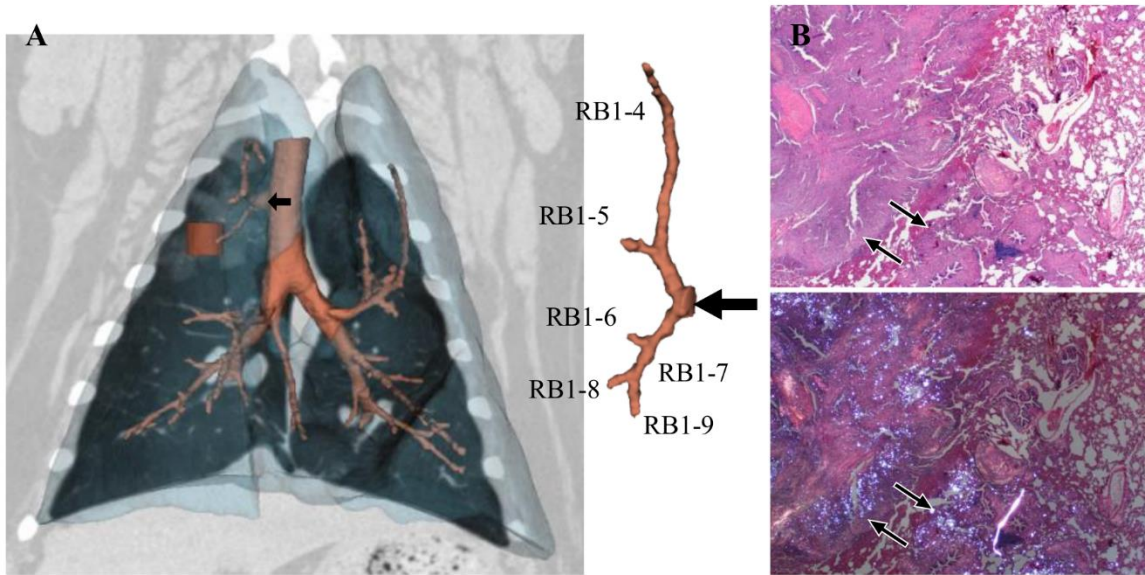
Figure 8-2: Silica deposition and pathology. (A) Volumetric rendering of the lungs (translucent blue) with the corresponding airway tree (peach). The red cylinder within the upper lung indicates the location of the volumetric region of interest used for CT attenuation analysis. The corresponding CT coronal-section shows the deposition of silica as noted by the increased attenuation in the surrounding area. The apical bronchus airway tree is shown to the right with the labeling system used to identify each branch. The black arrow shows the site of silica deposition with the bronchoscope corresponding to the black arrow in the coronal image. (B) Pathology obtained after the final time point showing locally extensive remodeling accentuated by fibrosis (arrows) and inflammation (HE stain, 2x) (top). Same section examined with polarized light noting white (refractive) silica granules (arrows) admixed with pulmonary remodeling (bottom).
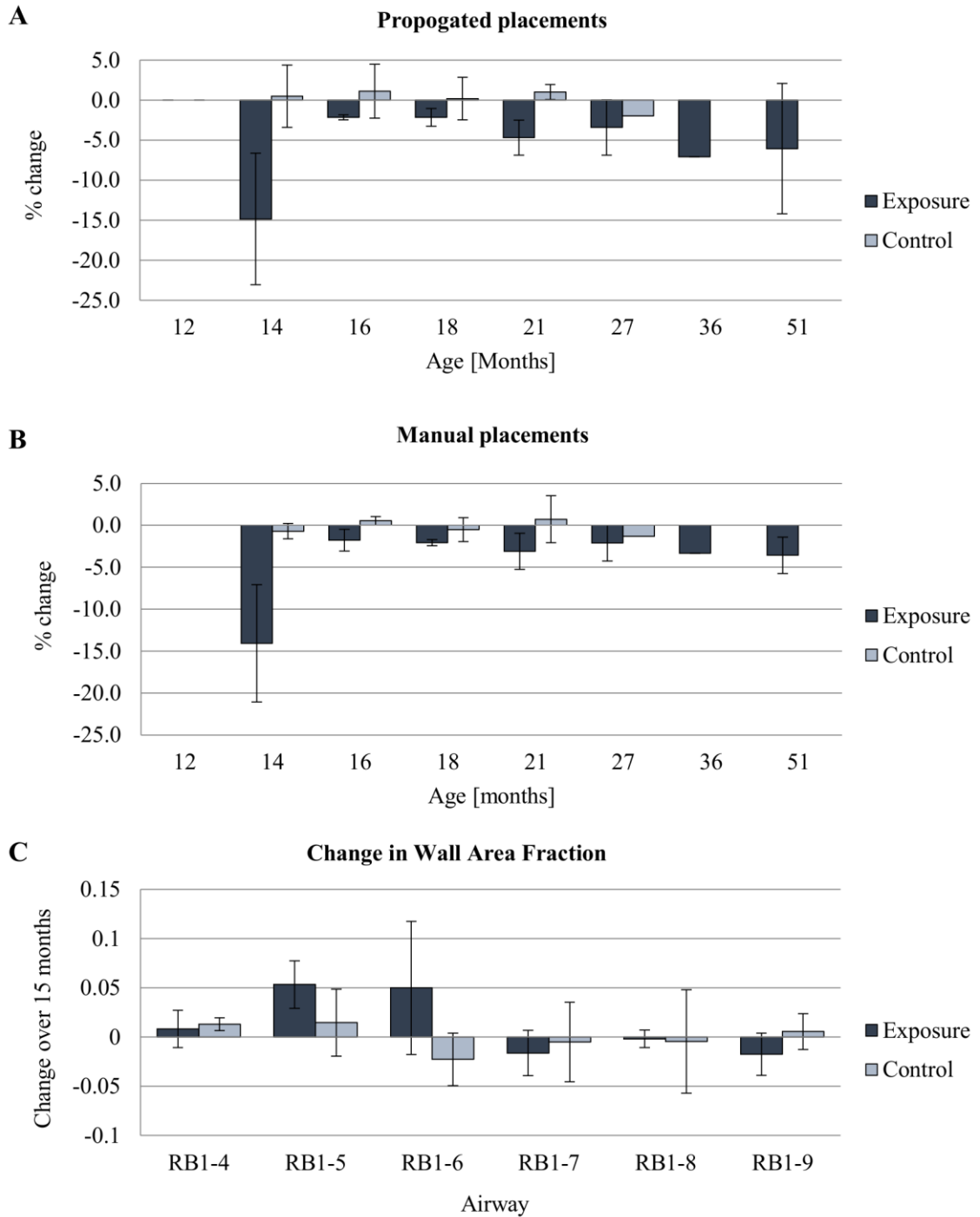
Figure 8-3: Quantitative trends. Percent change from baseline (at 12 months of age) of lung attenuation measured with (A) automatically propagated regions of interest from baseline and (B) manual placements for exposure and control animals. Due to the nature of CT in the lungs (negative Hounsfield Unit values), an increase in attenuation results in a negative percent change. Values were normalized to the mean whole lung intensity. (C) Change in wall area fraction in the peripheral airways of the apical bronchus tree. Change is determined as the difference between wall area fraction measured at 15 months post exposure (27 months of age) versus those acquired at baseline (12 months of age).

8.4 Discussion

We have presented an exposure animal model with crystalline silica showing quantitative measures of lung structural changes in the parenchyma and airways. We chose three exposure animals and three control animals for comparison with progression of disease seen in the exposure animals when compared with the control animals. The structural reporting mechanism aided in the comparison of findings between modalities and assisted in distinguishing transient from persistent structural changes within a modality, primarily reported upon in CHAPTER 4: STRUCTURED REPORTING. However, the structured reports did not capture the severity of a finding in a particular lobe and an approximately equal number of findings were reported in the right cranial lobes of exposure and control animals. Characterization was additionally aided by quantitative CT measures in the lung, showing density increase in the parenchyma and airway remodeling. Our findings support further exploration of these quantitative measures in a larger cohort to validate these biomarkers for the assessment of silicosis progression in pigs.

An advantage of CT data acquisition over MRI in this study was the ability to quantitatively assess the lung for airway wall structural changes over time using software developed for human CT pulmonary assessment. We demonstrated the use of software developed for human CT pulmonary assessment. These techniques have been established for characterization in human cohorts for comparison across subjects exhibiting chronic obstructive pulmonary disease (COPD) and other lung diseases [162, 163]. In addition to airway analysis, we demonstrated the utility of our longitudinal feature extraction extension for assessing density changes over time. A comparison was performed between manually placed regions versus regions automatically propagated from the first time point. Similar trends were observed with both regions. While subtle, this quantitative assessment reflects a progressive increase in lung density in the exposed region of the lung compared to the highly stable mean lung density in the control cohort. Greater standard deviations were observed among propagated regions compared to manual regions. During manual placement, the same voxel sized region was used during analysis across all lungs showing varying volumes depending on voxel size; however, propagated regions showed a more consistent volume with minor deviations depending on the amount of scaling, rotation, and translation included in the transform. This presented a greater opportunity for inclusion of voxels containing vessels and airway walls which would account for a larger standard deviation.

To capture and track longitudinal changes in pulmonary structure due to disease development using medical imaging, we selected to expose a subset of $TP53^{R167H/+}$ pigs to

crystalline silica. Silica exposure was selected for this study due to the progressive nature of silicosis formation that would provide an ideal model in which to compare longitudinal chest imaging techniques. In addition, crystalline silica is a carcinogen associated with lung cancer based on the study of occupational exposure [164-166] and supported by work in animals [156, 157]. Necropsy of one of the silica exposed pigs confirmed persistent silica deposition in the lung and localized fibrosis development; however, after 51 months of age, minimal changes were observed towards development of a lung cancer. This lack of tumor development suggests earlier exposure, prior to 14 months of age, and/or a more aggressive exposure delivered in one or multiple time points.

CHAPTER 9: RADIATION EXPOSURE MODEL

9.1 Introduction

Sarcomas have proved difficult with respect to the development of effective therapies due to their rare occurrence, minimal access to human samples, and limited adequate mouse models and in-vivo models. Spontaneous development of osteosarcoma was observed in the $TP53^{R176H/R176H}$ model described in CHAPTER 7: LI-FRAUMENI; however, the propensity for development in the cranium limits the utility of this model. Exposure to ionizing radiation is well known to increase the risk of cancer development with radiation-induced sarcomas seen in breast cancer patients and hereditary retinoblastoma patients treated with radiation therapy [167, 168]. In addition, Li-Fraumeni patients treated with radiation therapy have developed secondary cancers, including bone and soft tissue sarcomas, within a previous radiation field [169] with similar results seen in equivalent mouse models [170, 171]. Additionally, the most common site of metastasis seen with osteosarcoma patients is in the lung [172, 173], a site of interest for our group. With a known predisposition to sarcoma development, this chapter presents the development and characterization of $TP53^{R167H/+}$ and $TP53^{R167H/R167H}$ animals exposed to radiation aimed at accelerating and directing the development of sarcoma in the long bones.

9.2 Materials and methods

Model generation: A cohort of 4 animals (n = 2: $TP53^{R176H/R176H}$, n = 2: $TP53^{R176H/+}$) was irradiated to encourage osteosarcoma development in a peripheral location. A 3 cm x 3 cm window on the left hind leg corresponding to the tibia situated approximately 3 cm above the hock joint was chosen for targeted radiation exposure. The corresponding region on the right leg, not exposed to radiation, served as a contralateral control. A protocol delivering a cumulative maximum of 30 Gy at the skin surface was delivered through six 5 Gy fractions to the 9 cm^2 region at 200 kVp over a two-week time period. The left leg of the animal was propped up on an aluminum mounting frame to ensure consistent positioning and stability at each fraction. A 3 mm thick lead shielding isolating the radiation region of interest was placed on the leg and taped in place to limit any movement of the shield due to breathing of the animal. The calculated amount of total dose delivered to the bone is displayed in Table 9-1. All procedures were performed under anesthesia and approved by the Institutional Animal Care and Use Committees (IACUC) of the University of Iowa and Exemplar Genetics.

Table 9-1: Delivered radiation dose. The incident dose delivered to the bone in subjects Sar 1-4 given a cumulative 30 Gy at the skin surface through a 3 x 3 cm^2 field at 200 kVp with a 1 mm copper filter. Calculations were based on the TG-61 protocol with percentage depth dose (P_{dd}) values from BJR-25.

Subject	Proximal edge			Distal edge		
	Depth [cm]	P_{dd} [%]	Incident Dose [Gy]	Depth [cm]	P_{dd} [%]	Incident Dose [Gy]
Sar 1	1.9	79.2	58.4	2.3	74.6	55.0
Sar 2	1.7	81.5	60.0	2.1	79.1	58.3
Sar 3	2.0	78.0	57.5	2.3	74.6	55.0
Sar 4	2.4	73.4	54.1	2.8	68.8	50.7
Average			**57.5 ± 2.5**			**54.7 ± 3.1**

Table 9-2: CT imaging protocols for radiation exposure model. Parameters for CT imaging developed for a SOMATOM Force dual-source scanner. Chest protocols and whole-body imaging protocols were developed for assessment of metastasis and targeted hind leg protocols for assessment of radiation exposure area. Additional multi-planar reconstructions (MPR) were performed for the hind legs at slice thicknesses of 0.2 mm for quantitative imaging analysis.

	Chest		Whole-body	Hind legs
Scanner	Force	Force	Force	Force
Scan Type	Helical (SE)	Helical (SE)	Helical (SE)	Helical (SE)
Rotation time (s)	0.5	0.5	0.5	1.0
Det. Configuration	192 x 0.6	192 x 0.6	192 x 0.6	192 x 0.6
Eff. mAs	220	130	380	30
kV	120	120	120	120
Care Dose 4D	OFF	OFF	OFF	OFF
Pitch	1	1	1	0.3
Recon. Kernel	Qr40	Qr40	Br40	Ur77u, MPR
Iterative reconstruction	3	3	3	3
Slice Thickness (mm)	3, 0.75	3, 0.75	3, 0.75	0.2
Breath hold (cmH$_2$O)	20	5	20	None

Image acquisition: A cohort of 4 animals, 2 heterozygotes and 2 homozygotes, were imaged for disease characterization with protocols modeled after the image acquisition methods described in CHAPTER 3: LONGITUDINAL MEDICAL IMAGE ACQUISITION. Focus was placed on imaging the hind legs for disease development with whole-body screening of disease. Radiation exposure was non-targeted resulting in the desire for imaging with both CT and MRI for bone and soft tissue sarcoma screening.

Whole-body CT scans were obtained with a 128-multidetector dual-source scanner (SOMATOM Force, Siemens Healthcare, Forchheim, Germany) to assess for potential disease throughout the body, including metastatic disease. Additional inspiratory and expiratory chest scans were acquired to assess for metastatic disease in the lungs. Scans were acquired at an

inspiratory breath-hold of 20 cmH$_2$O and expiratory breath-hold of 5 cmH$_2$O following 2 minutes of pulmonary recruitment at an equivalent PEEP. Reconstructions were performed with a standard body kernel at slice thicknesses of 3 mm and 0.75 mm.

Following whole-body imaging, animals were positioned prone with hind legs extended in parallel. Targeted ultra-high resolution CT scans of the hind legs, corresponding to the region of radiation exposure, were obtained at each time point to evaluate the exposure region and contralateral control region. Multi-planar reconstructions were performed to align left and right tibias to the center of each image with an ultra-high resolution kernel at slice thickness of 0.2 mm. Similarly, targeted hind leg MRI scans were acquired with a 3-Tesla MRI system (TIM Trio 3T, Siemens Healthcare, Forchheim, Germany) with standard surface coils. High resolution T2 3D SPACE scans were acquired with 0.84 mm isotropic voxels and axial and coronal T1 scans were obtained with 3 mm slice thickness and 0.53 mm x 0.53 mm and 0.84 mm x 0.84 mm in-plane resolutions, respectively. Parameters for all acquired images are displayed in Table 9-2 and Table 9-3.

Table 9-3: MRI protocols for radiation exposure model. 3-Tesla TIM Trio MRI scanner parameters used to acquire targeted hind leg and mouth lesion images

	Hind leg			Neck		
	3D SPACE	**T1 (Axial)**	**T1 (Coronal)**	**T1 (Coronal)**	**T2 (Coronal)**	**STIR (Sagittal)**
Scanning sequence	Spin echo	Spin echo	Spin echo	Spin echo	Spin echo	Spin echo/Inversion recovery
Acquisition type	3D	2D	2D	2D	2D	2D
Repetition time (msec)	1630	550	653	418	5590	4960
Echo time (msec)	116	10	12	9.2	100	40
Flip angle (º)	120	150	90	148	143	160
Echo train length	137	3	1	3	13	7
Slice thickness (mm)	0.8	3	2.8	4	4	4
In-plane resolution (mm)	0.84 x 0.84	0.53 x 0.53	0.84 x 0.84	1.02 x 1.02	0.81 x 0.81	0.81 x 0.81
Acquisition matrix	320 x 161	512 x 192	320 x 224	256 x 256	320 x 240	320 x 224
Number of Slices	160	45	25	24	24	22
Approx. Scan time (min:sec)	12:25	4:45	4:20	1:15	3:20	2:45
Respiratory management	None	None	None	None	None	None

Structured reports: Structured reports were used to provide consistent and complete visual interpretation of the acquired scans. Each structured report included the assessment of the diagnostic quality of the scan and targeted anatomic structures of interest. Structures of interest included the skeletal system, specifically the hind legs, lungs, and brain. The RECIST diameter, imaging characteristics, and anatomic location were identified for each detected lesion. All scans were read by a radiologist and disease indications and development were recorded.

Registration: Multi-level registration was performed to align detected lesions in acquired longitudinal datasets. CT scans were registered to the second CT acquisition to account for increased growth rate observed in the young age of the animals at the first time point. Acquired MRI images were registered to CT scans obtained at the equivalent time point.

Feature extraction: Quantitative CT features focused on assessment of identified bone lesions and the exposure region in the hind leg compared to the control region. Features were extracted from bone lesions to compare their density and heterogeneity across datasets. For assessment of changes in the exposure versus control long bones, measurements were obtained over a defined region in the CT images. Cortical and trabecular bone were automatically segmented from the images to create individual masks for analysis. Quantitative measures of cortical bone material density (BMD) and thickness and trabecular BMD were obtained in each axial cross-section of the image in collaboration with Drs. Punam Saha and Dakai Jin [174], resulting in values distributed by slice number. Difference between the control leg and the exposure leg were used for analysis.

Table 9-4: Radiation exposure model imaging time points. The imaging time points acquired for characterization of the radiation exposure model. An X indicates imaging occurred, R indicates radiation exposure occurred immediately followed by imaging, a capital N indicates imaging occurring followed by necropsy within 24 hours, and a lowercase n indicates necropsy occurred without any imaging. Purple indicates that both CT and MRI were acquired.

Model	Subject	J	A	S	O	N	D	J	F	M	A	M	J	J	A	S	O	N	D	J	F	M	A	M	J	J	A	S	O	N	D	Necropsy Diagnosis
				2014									2015												2016							
$TP53^{M/M}$ + radiation	Sar$_{hom}$ 1					B							R	n																		Lymphoma
$TP53^{M/M}$ + radiation	Sar$_{hom}$ 2					B							R		X			X			N											Osteosarcoma
$TP53^{M/+}$ + radiation	Sar$_{het}$ 3					B							R		X			X														
$TP53^{M/+}$ + radiation	Sar$_{het}$ 4				B								R		X			X														

Figure 9-1: Targeted hind legs protocols. Protocols acquired in the hind leg from (A) CT and MRI (B) T1 coronal, (C) T1 axial, and (D) T2 SPACE.

Sar$_{hom}$ 1-2 and Sar$_{het}$ 3-4 were imaged with CT and MRI for a range of 1 to 4 time points as shown in Table 9-4. Following trends seen in CHAPTER 7: LI-FRAUMENI for *TP53* animals, disease was detected in both homozygote animals with minimal indicators detected in both heterozygote animals. Heterozygotes continue to be monitored for clinical signs. Upon imaging of subject Sar$_{hom}$ 1, early indications of lymphoma were detected with pathological confirmation shortly after imaging. Three imaging time points were acquired for the remaining animals with example images displayed in Figure 9-1. A final, fourth time point was acquired for subject Sar$_{hom}$ 2 upon clinical indications of an aggressively growing tumor in the mouth. Targeted scans of the lesion were additionally acquired in MRI for soft tissue characterization with parameters listed in Table 9-3.

Table 9-5: Structured reporting lesion tracking and characterization. Lesions identified in subject Sar 2 characterized by the RECIST diameter, largest perpendicular diameter, and imaging characteristic defined in comparison to the intensity of bone in the image.

Lesion name	Time point detected	RECIST diameter [mm]	Perpendicular diameter [mm]	Imaging characteristic (relative to bone)
Right metatarsal	1	5.3	3.4	Heterogeneous
	2	14.1	4.6	Heterogeneous
	3	6.4	4.2	Heterogeneous
	4	11.3	6.5	Heterogeneous
Proximal left femur	2	7.9	6.3	Hyper-intense
	3	14.0	9.5	Heterogeneous
	4	14.2	11.9	Heterogeneous
Distal left femur	2	4.9	4.7	Isointense
	3	5.5	4.5	Hypo-intense
Right humerus	3	19.4	7.0	Heterogeneous
	4	19.1	11.3	Heterogeneous
Mouth lesion	4	74.4	36.4	Hypo-intense

Structured reports led the assessment of disease in each set of scans. Enlarged lymph nodes (>3 cm) and a mildly enlarged liver and spleen were noted in subject Sar$_{hom}$ 1 as early indicators of lymphoma. Several bone lesions were detected in subject Sar$_{hom}$ 2 throughout the limbs beginning in the first time point listed in Table 9-5. Only one lesion, located in a right metatarsal, was present in the first imaging time point showing a RECIST of 5.3 mm. Growth of this lesion was shown to be variable with RECIST diameters of 14.1 mm, 6.4 mm, and 11.3 mm at time points 2, 3, and 4, respectively, with a heterogenous intensity pattern seen at all 4 time points. Two lesions were identified in the left femur. The distal lesion was initially noted as isointense with respect to bone and had a RECIST of 4.9 mm. The following imaging time point

showed minimal change in RECIST (5.5 mm); however, the intensity was noted as hypo-intense with respect to bone with no lesion noted in the final time point. The proximal femur lesion appeared in the second time point with a RECIST of 7.9 mm. Minimal growth was apparent between the last two time points with RECIST measurements of 14.0 mm and 14.2 mm, respectively; however, progression was seen from a solid, spherical, hyper-intense lesion at the second time point to increasing heterogeneity in subsequent time points. A final bone lesion was noted in the right humerus showing the development of a 19.4 mm lesion between the second and third time points. Growth showed relative stability according to a RECIST of 19.1 mm at the last time points. Lastly, a mouth lesion was noted in the final time point showing a large mass with a RECIST of 74.4 mm extending from the right mandible. Imaging characteristics showed a primarily soft-tissue lesions with a well-defined border and a bony matrix as seen in Figure 9-2C. No relevant disease findings were noted in subjects $Sar_{het}3$ or Sar_{het} 4 or in the radiation exposure region of all animals.

To quantitatively assess early changes in the bone exposed to radiation, regions of interest were placed on the hind tibias spanning the length of the bone from the growth plate of distal tibia to the entrance of the vessel foramen into the marrow. Cortical and trabecular bone were successfully segmented and bone density measures and cortical bone thickness were obtained. Results were subdivided into three regions within the region – the distal extremity, the distal shaft, and the middle shaft – with exposure directed at the distal shaft. Minimal differences were seen between the control and exposure tibia bones regarding cortical bone thickness and trabecular BMD. Differences were seen between cortical BMD measurements with a greater density seen in the exposure tibia (left) overall as seen in Figure 9-3. Subject Sar_{hom} 2 showed the largest differences at the second time point, six weeks post exposure protocol. Elevated differences remained in the distal extremity and distal shaft through the remaining time points with compared to the first time point. Subject Sar_{het} 3 showed increasing differences in the exposure leg throughout the region over time. Subject Sar_{het} 4 showed positive differences initially, prior to exposure, with smaller negative differences in consecutive time points. Overall, no clear trends were observed indicating the presence of tumor development.
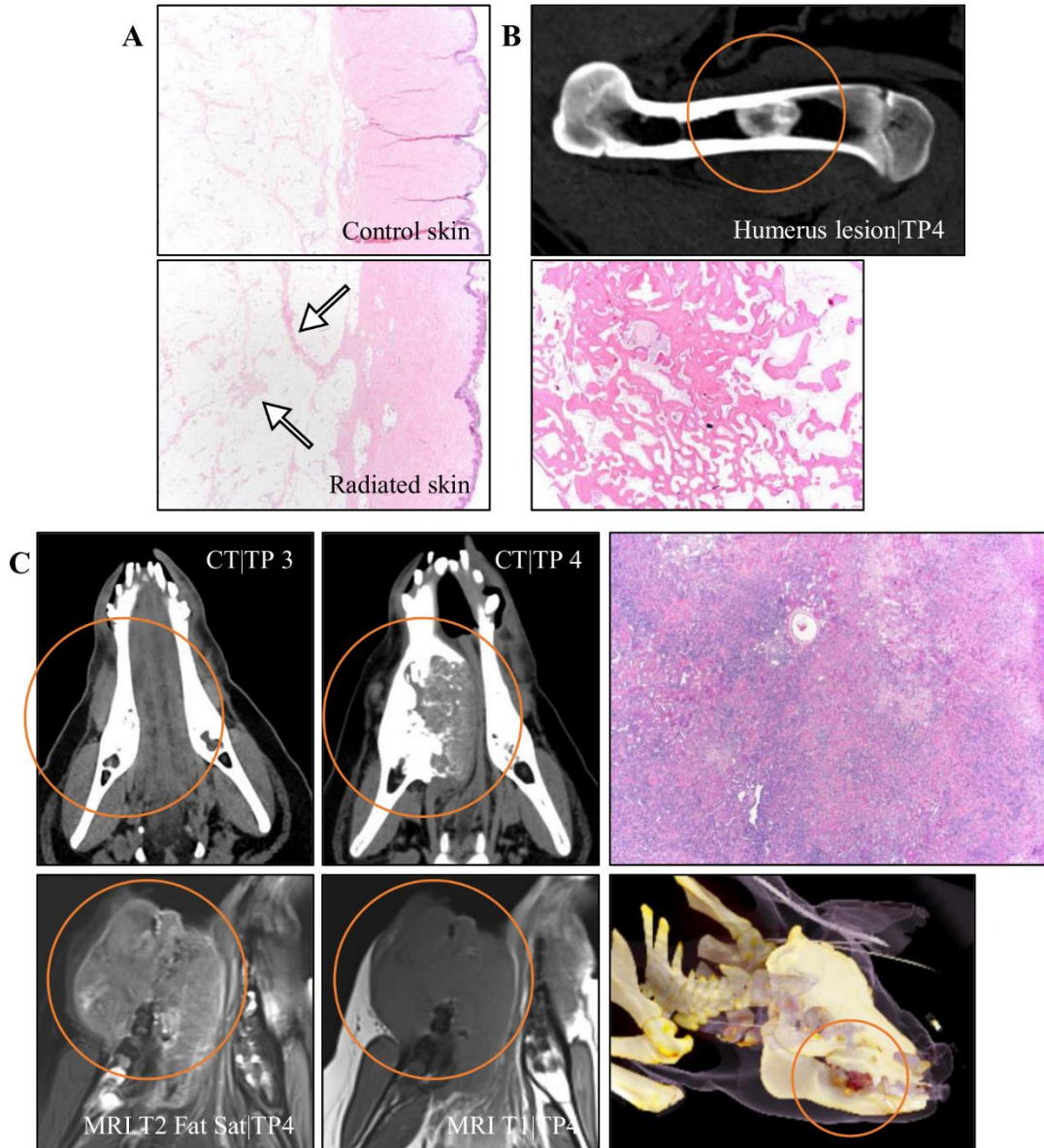
Figure 9-2: Pathology and other lesions. (A) Scarring process (arrows) seen at the radiated skin site through increased connective tissue (HE stain, 2x). (B) Right humerus lesion (orange circle) in CT showing increased density with corresponding pathology showing deposition of trabecular bone (HE stain, 2x). (C) Mouth lesion, highlighted by the orange circle, with no indications seen in time point 3 with an aggressive lesion seen in time point 4 on CT, MRI T2, and MRI T1. Rendering is seen in the head showing the location of the lesion (bottom right) with pathology displaying inflammation and necrosis with bony proliferation (top right).
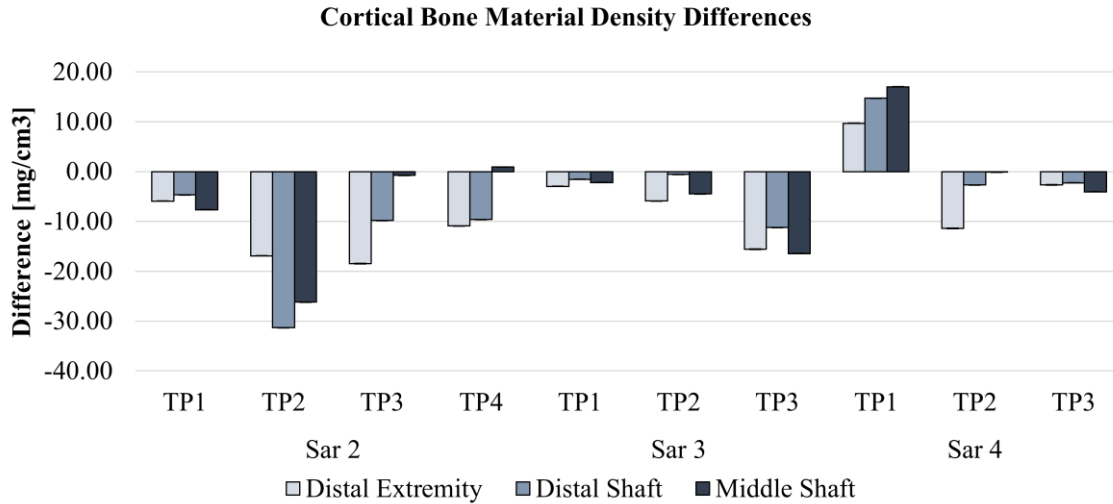
Figure 9-3: Cortical bone material density (BMD) analysis of tibia. Cortical BMD differences between the control (right) tibia and the exposure (left) tibia at each time point by bone location (distal extremity, distal shaft and middle shaft). A negative difference indicates that the radiation-exposed tibia (left) has a greater density than the control tibia (right).

Multi-level registration across all 4 time points of Sar$_{hom}$ 2 was focused on the lesion identified in the proximal left femur to illustrate its growth and change over time, seen in Figure 9-4. Due to large differences in positioning at the hind limbs during supine positioning, manual initialization was required following by one level of registration focused on a region of interest around the femur. Independent masks were created identifying regions within each lesion for quantitative feature extraction. Average intensity and standard deviation values matched visual trends with decreasing mean intensity and increasing heterogeneity over time. As seen in Table 9-6, the mean intensity decreased at each time point while the standard deviation increased over time. Time point 2 saw an average intensity of 772.76 (± 173.61) HU with 676.18 (± 206.02) HU and 516.18 (± 235.83) HU seen in time point 3 and 4, respectively.

Table 9-6: Automatic lesion tracking and characterization. Quantitative features extracted from the left proximal femur lesion. The RECIST measurement was obtained following imaging registration to align the lesion across time points. Quantitative features were acquired from individually placed regions across datasets.

Time point	RECIST	Minimum	Maximum	Mean	Standard deviation
2	9.78	173	1109	772.76	173.61
3	14.1	-116	1380	676.18	206.02
4	14.2	-91	1580	516.18	235.82
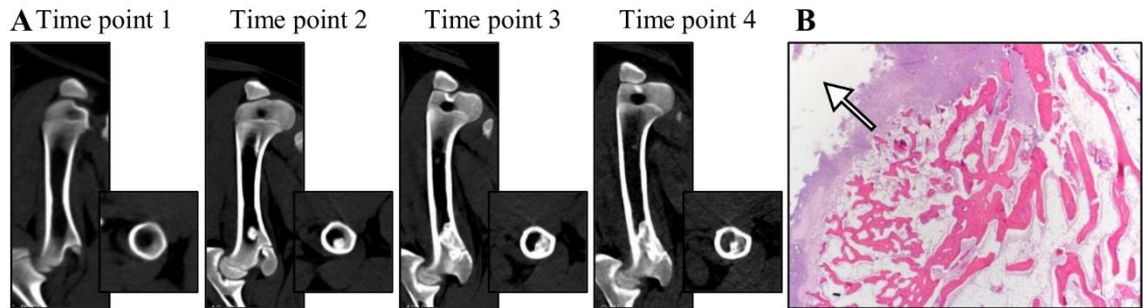
Figure 9-4: Proximal femur lesion. (A) The post-registration CT of the proximal femur lesion in the coronal and axial planes showing progression from no lesion (time point 1) to a heterogeneous lesion (time point 4) with (B) corresponding pathology obtained following time point 4 showing a lytic region (arrow) at the edge of the bone (HE stain, 2x).

Necropsy was performed on subject Sar_{hom} 2 immediately following the final imaging time point. Acquired images led targeted tissue collection and histopathology was acquired for the radiation exposure region and lesions in the femur, humerus, and mouth and displayed in Figure 9-2 and Figure 9-4. Increased connective tissue, denoting scarring, was seen in the skin of the radiation exposure region compared to the skin in the control region. The femur contained a lytic lesion; represented in the imaging and quantitative characteristics as a decreasing mean intensity and increasing heterogeneity. The humerus showed an increased density and deposition of trabecular bone as indicated by the heterogenous intensity pattern seen in the internal portion of the shaft. The mouth lesion was identified as an aggressive lesion composed of inflamed and necrotic tissue with bony proliferations.

9.4 Discussion

We have presented the development and characterization of a heterozygote and homozygote Li-Fraumeni animal model with additional radiation exposure to the hind leg aimed at targeted sarcoma development. We chose two heterozygotes and two homozygotes to build upon the tumor susceptible genetic background. Whole-body imaging and targeted lung imaging was performed with CT with additional targeted imaging protocols designed for soft tissue and bone characterization in the hind legs with CT and MRI. Several bone lesions were detected in a single homozygote subject. By assessment of RECIST, most lesions showed growth over time; however, the lesion in the right metatarsal did not, which was primarily noted due to differences in positioning of the hind legs further illustrating the limitations of the RECIST measurement. Quantitative CT methods were additionally developed for characterization showing minimal changes in cortical and trabecular bone between control and exposure legs. Our findings suggest

the need for continued monitoring of heterozygote animals with expectation of tumor development in the future.

Our developed methods were essential in characterizing this model. Whole-body, longitudinal screening was important for detection of peripheral bone lesions and tracking their progression together with structured reporting. Most lesions progressed from a bright, isointense lesion to a heterogenous intensity pattern as seen in the right metatarsal and left proximal femur suggesting progression of disease which cannot be identified by RECIST alone. A lesion was also noted in the distal femur; however, it progressed from isointense to bone to hypo-intense to resolution throughout imaging. The detected mouth lesion was characterized with both CT and MRI showing various levels of soft tissue and bone involvement. Previous studies have shown that MRI is superior to CT in evaluation of bone tumors due to the ability to effectively delineate the margins of the tumors with corresponding soft tissue involvement [175, 176]. In general, MRI imaging of the bone has challenges due to the short tissue relaxation times; however, protocols have been developed to overcome these challenges, including the development of ultra-short echo time (UTE) imaging [177] and fat suppression [178] which may aid in further characterization of detected lesions. MRI imaging was not acquired for any other lesions due to the limited field of view in the targeted acquisitions.

In addition, our registration algorithm was used for alignment of the peripheral femur lesion. For this model, the second time point image was chosen as the fixed image to minimize growth changes between the fixed image and all other images. Due to differences in positioning of the hind limbs during whole-body screening, significant manual alignment was required for initialization. While specialized, prone positioning was implemented for targeted hind leg scans, the field of view was isolated specifically to the tibia and did not extend up to the femur. Extending this field of view may present further opportunity for consistent positioning along the skeleton. We also demonstrated quantitative feature extraction on the targeted radiation region and the peripheral bone lesion. To account for growth in the long bones, we developed a normalization schema by isolating the same region of bone using physical indicators and normalizing measurements to the corresponding slice. This aided in comparison across exposure and control bones and across subjects. Quantitative analysis of the proximal femur lesion further aided characterization beyond notations in the structured reports. While a consistent RECIST measurement was obtained in the last two time points, quantitative measures showed a decreasing intensity with increasing heterogeneity suggesting progression of the lytic process.

Lastly, there are limitations associated with this model. Subject $Sar_{hom}1$ developed lymphoma shortly after radiation exposure. This animal was not replaced in the study due to the lack of available substitutions and scheduling limitations. Of the remaining animals, tumor development did not occur in the region of the limb exposed to radiation to date (20 months post exposure); however, tumors were detected in other areas of the body in subject Sar_{hom} 2. Other large animal studies in dogs have shown similar latency periods ranging from 1-5 years post radiation exposure [179, 180]. We expected an expedited tumor formation in these models due to the *TP53* mutant background as seen with the increased rate of sarcomas in Li-Fraumeni patients with radiation treatment [169]. External radiation exposure is advantageous as a carcinogen, over other potential methods, such as chemical exposure or internal radiation sources, as the animal itself is not hazardous post-exposure, eliminating the need for special containment of the animal. We used a conservative level of radiation exposure, adhering to skin limitation guidelines for humans, to avoid desquamation of the skin. While pathology did note some scarring at the radiation exposure site, no evidence of radiation damage to the skin was observed in these animals and a higher dose may be well tolerated in future studies. While no solid tumor was present in the exposure region, radiation may have triggered the formation of cancer-type cells that circulated in the blood and initiated the process for those lesions identified; similar to the metastatic process [181]. These findings suggest the potential utility of a more aggressive radiation exposure and/or exposure at an earlier age.

CHAPTER 10: CONDITIONALLY ACTIVATED KRAS MODEL

10.1 Introduction

Normal functioning *KRAS*, a member of the RAS protein family, is a primary regulator of cell division, including promoting cell survival, cell growth, cell cycle progression, and transcription [182]. In contrast, the p53 protein, encoded by the *TP53* gene, functions in tumor suppression by inhibiting angiogenesis and monitoring growth, DNA repair, and signaling for apoptosis. The specific combination of mutations in both *TP53* and *KRAS* are well established among human cancers and widely used in the development of mice models, including lung and pancreatic cancer [148, 183-187]. Among lung cancers, specifically adenocarcinoma, p53 mutations are seen in 50-70% of cases and *KRAS* mutations seen in 30-35% [188, 189]. For pancreatic cancer, *KRAS* mutations are observed in over 90% of tumors [190].

With the aim of enhancing temporal and spatial control of cancer development, a dual-targeted $KRAS^{G12D/+}/TP53^{R167H/+}$ model was created by Exemplar Genetics. Animals were confirmed to express one mutant allele of the *TP53* gene in all tissues in conjunction with Cre-inducible mutant *KRAS*. A cohort of animals (n=3) was designated for characterization with targeting in the lungs and pancreas. Activation of the *KRAS* mutation in the lungs occurred via bronchoscope injection of the Cre virus into the upper right lung (n=2) and the pancreas via direct injection following surgery (n=2). All procedures were performed under anesthesia and approved by the Institutional Animal Care and Use Committees (IACUC) of the University of Iowa and Exemplar Genetics.

This chapter presents the characterization of this model using the methods described in CHAPTER 3 – CHAPTER 6. Focus was placed on identifying tumor development in the lungs and pancreas with whole-body screening for metastasis.

10.2 Materials and methods

Image acquisition: A cohort of 3 animals were imaged for disease characterization modeled after the image acquisition methods described in CHAPTER 3: LONGITUDINAL MEDICAL IMAGE ACQUISITION. Focus was placed on chest and pancreas imaging with low dose whole-body screening. CT scans were obtained with a 128-multidetector dual-source scanner (SOMATOM Force, Siemens Healthcare, Forchheim, Germany) to assess for potential

disease, including metastatic disease. Inspiratory and expiratory chest scans were acquired to assess for disease development in the lungs. Scans were acquired at an inspiratory breath-hold of 20 cmH_2O and expiratory breath-hold of 5 cmH_2O following 2 minutes of pulmonary recruitment at an equivalent PEEP. A contrast enhanced pancreas protocol modeled after standard clinical practice, was developed to acquire abdominal scans following injection of contrast (50% saline/50% contrast) at 5cc/sec. Arterial scans were automatically triggered at a value of 100 HU detected in a region monitored in the abdominal aorta beginning 5 seconds post injection. A pancreatic phase scan was then acquired at 40 seconds post contrast and a final scan was obtained 70 seconds post contrast for portal venous phase assessment. Reconstructions were performed with a standard quantitative kernel with level 3 iterative reconstruction at slice thicknesses of 3 mm and 1 mm. A final, low-dose, whole-body scan was acquired to assess for metastatic disease and reconstructed with a standard quantitative kernel with level 5 iterative reconstruction at slice thickness of 3 mm. Parameters for all images are listed in Table 10-1.

Table 10-1: CT imaging protocols for KRAS activation model. Parameters for CT imaging developed for a SOMATOM Force dual-source scanner.

	Chest		Whole-body	Contrast-enhanced		
Scanner	Force	Force	Force	Force	Force	Force
Scan Type	Helical (SE)	Helical (SE)	Helical (SE)	Helical (DE)	Helical (SE)	
Rotation time (s)						
Det. Configuration	192 x 0.6	192 x 0.6	192 x 0.6	192 x 0.6	192 x 0.6	192 x 0.6
Eff. mAs (reference)	200	200	20	200	200	200
kV (reference)	120	120	100	120	120	120
Care Dose 4D	ON	ON	ON	ON	ON	ON
Care kV	OFF	OFF	ON	OFF	OFF	OFF
Pitch	1	1	1	1	1	1
Recon. Kernel	Qr40	Qr40	Qr40	Qr40	Qr40	Qr40
Iterative reconstruction	3	3	5	3	3	3
Slice Thickness (mm)	1	1	3	1	1	1
Breath hold (cmH_2O)	20	5	20	20	20	20
Contrast delay (seconds)	None	None	None	20	40	70

Structured reports: Structured reports were used to provide consistent and complete visual interpretation of the acquired scans. Each structured report included the assessment of the diagnostic quality of the scan and targeted anatomic structures of interest. The anatomic

structures of interest included the lungs, pancreas, and the liver. The RECIST diameter, imaging characteristics, and anatomic location were identified for each detected lesion. All scans were read by a radiologist and disease indicators and development across time points was recorded.

Registration and feature extraction: Multi-level registration was performed to align longitudinal CT datasets of the lungs. Several regions of interest were identified in the lung corresponding to disease, such as nodules and ground glass opacities, and normal lung and automatically identified in all subsequent images. Acquired measures were normalized to the mean intensity of the entire lung with a value greater than 1 indicating less dense tissue and less than 1 indicating increased density relative to the entire lung. Whole lung masks and mean intensity were acquired via the methods described in CHAPTER 5: MULTI-LEVEL REGISTRATION. Trends were observed to identify progression of disease over time. For the pancreas, contrast enhancement patterns were quantitatively identified with a region of interest placed in the tail of the pancreas in the arterial phase of the image. The corresponding region was then automatically propagated to the pancreatic and portal venous phase images and features were extracted. Trends were observed to determine irregular contrast uptake patterns.

Table 10-2: KRAS activation model imaging time points. The imaging time points acquired for characterization of the radiation exposure model. An X indicates imaging occurred and e indicates KRAS activation occurred. Blue indicates that only CT was acquired.

Model	Subject	J	A	S	O	N	D	J-D	J-J	J	A	S	O	N	D	J	F	M	A	Necropsy Diagnosis
		2014						2015	2016							2017				
$TP53^{M/+} + KRAS^{M/+}$ (Lung)	Ras 1		B							e				X			X				
$TP53^{M/+} + KRAS^{M/+}$ (Pancreas)	Ras 2		B							e			X				X				
$TP53^{M/+} + KRAS^{M/+}$ (Lung/Pancreas)	Ras 3		B							e			X				X				

Figure 10-1: Contrast enhanced CT protocol. Abdominal scans acquired 20 seconds post contrast in the arterial phase, 40 seconds post contrast in the pancreas phase, and 70 seconds post contrast in the venous phase. The tail of the pancreas is identified by the orange circle in all images.
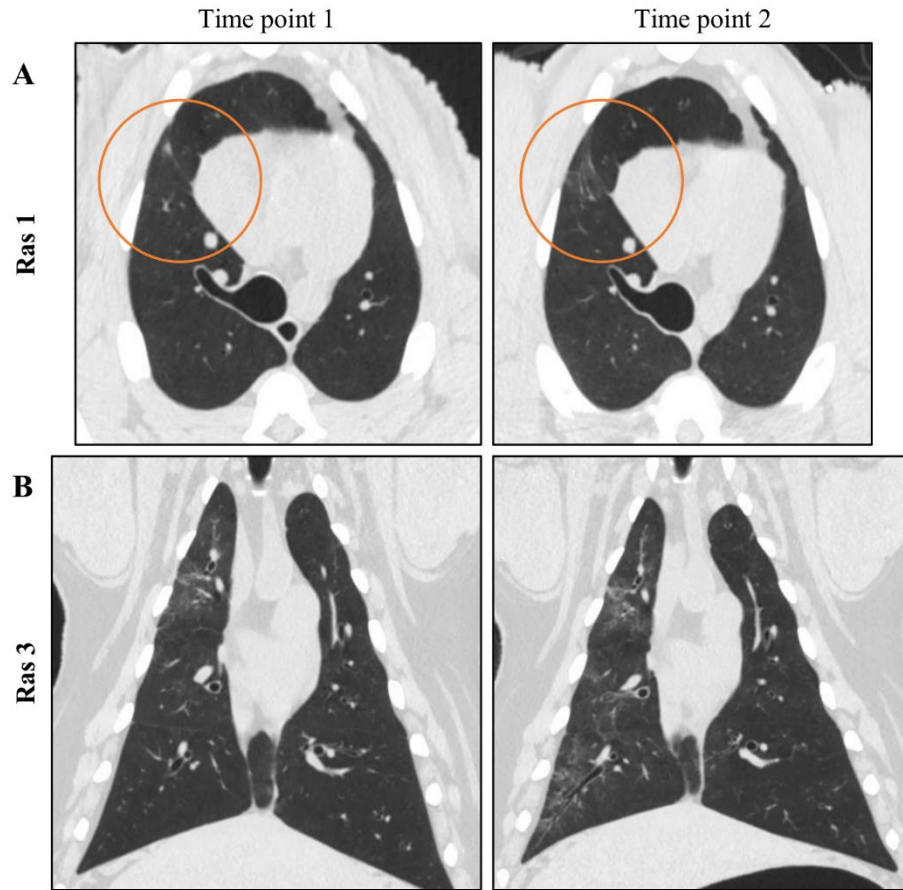
Figure 10-2: Ground glass opacities. (A) Development of ground glass opacities observed via CT, indicated by the orange circle, in the lungs of subject Ras 1. (B) Progression of ground glass opacities throughout the right lung of subject Ras 3.

10.3 Results

All imaging protocols were acquired for subjects Ras 1-3 for a total of two time points listed in Table 10-2. Imaging occurred 3 and 6 months following exposure corresponding to 26 and 29 months of age. Imaging was successfully performed on all animals with example contrast enhanced sequence seen in Figure 10-1 and example lung images seen in Figure 10-2. Whole-body, low-dose protocols were successfully obtained with a CT dose index (CTDI) of 0.84 ($\pm$ 0.26) mGy and were useful in further identifying structures that continued outside of the chest and abdominal field of view, specifically in the abdomen.

Structured reports led the qualitative assessment of disease in all three animals. A single nodule was noted along the fissure between the right middle and upper lobe in subject Ras_{lung} 1 at the first imaging time point. Subsequent imaging showed nodule stability, according to RECIST assessment, with increased ground glass opacities surrounding the nodule. Chronic right lung

disease was noted in subject Ras$_{pan}$ 2 characterized by consolidation and bronchiectasis seen in both time points with no pancreatic abnormalities observed. Lastly, subject Ras$_{lung/pan}$ 3 showed ground glass airspace disease in the right lung with predominance in the upper lobes noted in both time points. Small nodules ($<$ 3mm) in the right upper lobe and left upper lobe were detected in the first time point; however, were resolved by the second time point. In the abdomen, a hypodense region was noted in the pancreas at both time points and free fluid was additionally observed in the mesentery.

Quantitative assessment of contrast enhancement showed increasing uptake of contrast throughout all three phases, except for subject Ras$_{lung/pan}$ 3 in the first imaging time point where a quick washout of contrast was observed in the portal venous phase image as seen in Figure 10-3.
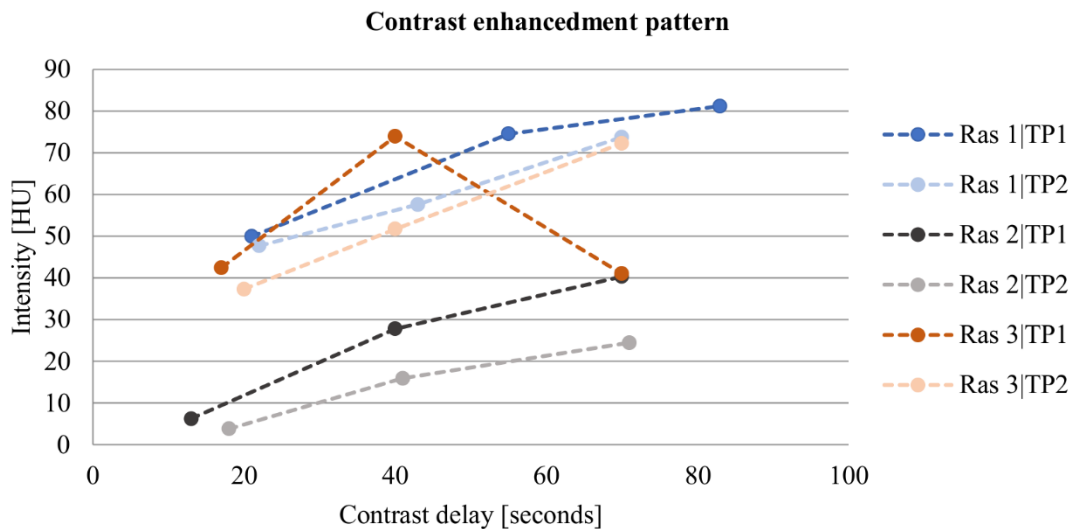
Figure 10-3: Quantitative contrast enhancement patterns. Measures obtained from the pancreas region of interest showing average intensity values where each dot represents an image taken at a specific contrast delay corresponding to the arterial, pancreatic, and venous phase.

Quantitative features were extracted from the right and left lung in subjects that received exposure in the lungs, displayed in Figure 10-4. Subject Ras$_{lung}$ 1 showed quantitative progression of a ground glass opacity in the upper right lung. A region of interest was placed in the second time point corresponding to the opacity and automatically identified in the first time point. Normalized mean intensity showed an increase in density over time with values of 0.98 and 0.92 in the first and second time point, respectively. In comparison, three comparative regions were placed in the left lung representing normal tissue and showed minimal deviation from the average whole lung intensity at normalized values of 1.02 ($\pm$ 0.02) and 1.03 ($\pm$ 0.005) for time point 1 and 2, respectively.

101

Subject Ras$_{lung/pan}$ 3 showed more diffuse ground glass opacities, noted as airspace disease, in the right lung. Four regions were placed in the right lung (two upper lung, two lower lung) and two regions in the left lung for comparison. Both right lung regions showed an increased density at the first time point with normalized values of 0.89 ($\pm$ 0.02) and 0.96 ($\pm$ 0.04) in the upper and lower regions, respectively. Progressive increased density was observed at the second time point with corresponding normalized values of 0.77 ($\pm$ 0.03) and 0.92 ($\pm$ 0.02). Additionally, increased density was seen in the upper regions versus the lower regions of the right lung with a more increased progression between time points observed in the upper regions. In comparison, left lung regions showed a lower density at both time points compared to the whole lung with values of 1.05 ($\pm$ 0.03) and 1.09 ($\pm$ 0.04) for time point 1 and 2, respectively. Similar measures were obtained from subject Het 3 (27 months of age), described in CHAPTER 8: CRYSTALLINE SILICA EXPOSURE MODEL, for comparative measures. Results showed minimal differences between values obtained from three regions in the right lung and three regions in the left lung as seen in Figure 10-4 with normalized values of 1.03 ($\pm$ 0.005) and 1.02 ($\pm$ 0.01), respectively.
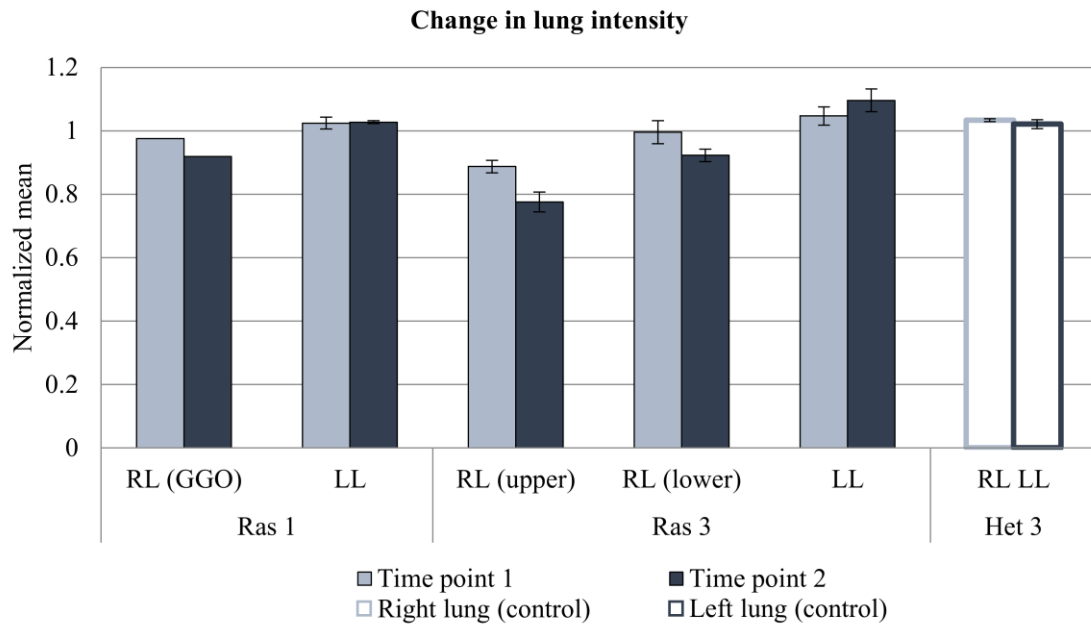
Figure 10-4: Quantitative lung measures. Measures obtained from regions placed throughout the lung of subjects Ras 1 and Ras 2. For subject Ras 1, the right lung (RL) measures were obtained from one region corresponding to the noted ground glass opacities (GGO) compared to three regions placed in the left lung (LL). For subject Ras 2, four regions were placed in the RL (two upper and two lower) and two regions were placed in the LL. For comparison, similar measures were obtained from a control subject showing no lung disease indicators in the RL and LL. All measures were normalized to the mean intensity value obtained from the entire lung.

10.4 Discussion

We reported on the non-invasive characterization of an animal model with dual-targeted mutations associated with *TP53* and *KRAS*. A total of three animals were used such that exposure occurred in the lungs, pancreas, and both organs. The animal without targeted organ specific activation of the *KRAS* mutation was used as a control. Unfortunately, chronic lung disease was detected in subject Ras_{pan} 2, potentially due to post-surgical aspiration, limiting its utility as a control for the lung-activated models; rather, an animal from the Li-Fraumeni cohort, described in CHAPTER 8: CRYSTALLINE SILICA EXPOSURE MODEL at an age matched time point, was used as a non-lung exposure control for quantitative comparison.

CT was chosen as the imaging modality of choice due to its ability to acquire fast, whole-body images, and current clinical standard in assessing lung and pancreatic cancers. Targeted protocols were developed for specific organ assessment. Lung protocols were similar to those used in CHAPTER 9: RADIATION EXPOSURE MODEL for metastatic assessment. CT is also the most commonly used modality for pancreatic cancer assessment with a tri-phasic protocol, with the pancreatic phase being the most sensitive to pancreatic parenchymal assessment and the portal venous phase used for liver assessment [191]. MRI is also highly sensitive to pancreatic lesions due to its superior soft tissue contrast resolution and may be included for future assessment of detected lesions. Additionally, whole-body screening was performed with low dose CT incorporating automatic adjustment of both the tube current and tube voltage for dose modulation and iterative reconstruction techniques to achieve an acceptable diagnostic quality image with minimal artifacts at such a low dose. These techniques have previously shown maintenance of qualitative integrity of acquired images [3-5, 7, 80]. Recent studies by Hammond, et. al [192] have also shown comparable quantitative integrity among lung measures extracted from images acquired with several low dose techniques, including tube current modulation and iterative reconstruction.

We also presented the use of quantitative measures for characterization in the pancreas and the lungs. Acquired lung images were registered using the multi-level registration algorithm; however, the acquisition of targeted scans focused on the lungs with diffuse disease identified throughout the organ prevented the need for multiple registration levels. Specific alignment of a region within the lungs, i.e. upper right lung, may require the use of multiple levels for better alignment even with the acquisition of targeted scans.

Quantitative features were extracted from multiple propagated regions through both time points demonstrating an increase in density in the ground glass regions detected in the right lung. Structured reports indicated the presence of stable disease in these regions; however, quantitative characterization showed progression of increased density in measures. In comparison with an animal of approximate matched age (27 months) and similar genetic background ($TP53^{R167H/+}$) with no genetic alteration in *KRAS*, these results suggest that progression of disease in the right lung is resultant from the methods described. However, pathological confirmation is still required to determine if this is due to the presence of the *KRAS* mutation or presence of normal aspirate events displaying increased inflammation.

Similar trends were observed across quantitative measures obtained from contrast enhancement through the tail of the pancreas. Subject Ras$_{lung/pan}$ 3 showed an abnormal enhancement pattern in the first imaging time point. Abdominal indicators of disease were noted in this subject including a hypodense region in the pancreas; however, a normal enhancement pattern was observed at time point 2. Further monitoring of this cohort may give insight into these markers for potential predictors of disease.

After two imaging time points (3 and 6 months post activation of the *KRAS* mutation), no overt tumors were identified in the animals; however, several findings were noted for continued monitoring in the lungs and the pancreas. Mutant *KRAS* activation of these animals did not occur until approximately 2 years of age due to availability of animals and scheduling. Activation at a younger age may increase the temporal control of observed disease. Other pig models exhibiting *KRAS* mutations have been developed with [65] and without inclusion of *TP53* mutations [64]. In these animals, only tumors of mesenchymal origin have been observed [65]. In comparison, mouse models exhibiting a *KRAS* mutation in conjunction with a *TP53* mutation show spontaneous development of lung cancer and pancreatic cancer [185, 193]. Continued monitoring of this cohort is occurring with the expectation of continued disease progression in the lungs and abdomen with tumor formation.

CHAPTER 11: CONCLUSION

The goals of this research were to effectively characterize porcine disease models using clinical imaging systems and post-acquisition processing techniques. We have presented three aims to accomplish this goal through the characterization of four disease models targeted for cancer development: Li-Fraumeni heterozygote and homozygote base models, crystalline silica exposure model, radiation exposure model, and a conditionally activated *KRAS* mutation model.

Aim 1: Develop imaging protocols for the characterization of the phenotype to genotype relationship in novel porcine disease models. We have shown the ability to longitudinally monitor animals for disease screening with CT and MRI. Whole-body protocols were acquired on all animals with targeted acquisitions developed corresponding to the specific model. These methods provided non-invasive assessment of each animal to guide characterization.

Aim 2: Develop longitudinal post-acquisition image analysis methods for monitoring disease progression. We have presented image analysis methods for tracking disease progression. Structured reporting was used to provide consistent and systematic qualitative interpretation of acquired datasets. Multi-level registration was shown to provide alignment of anatomies of interest in longitudinal datasets. Lastly, we developed a tool to extract features from desired regions of interest extending the registration algorithm to quantitatively track disease.

Aim 3: Utilize the developed medical imaging techniques to characterize tumorigenesis in a variety of genetically modified, cancer prone, pig models. Changes in features were seen in the parenchyma and airways of the lungs in the crystalline exposure model and conditionally activated *KRAS* model. Lymphoma was quantitatively characterized through analysis of the liver and spleen. Similarly, osteosarcomas and renal tumors were quantitatively assessed.

The developed methods lay a foundation for the use of porcine disease models as surrogates of human disease. For all models, small cohorts (n = 3 – 6) were characterized due to animal availability and model generation methods further enforcing the desire to develop non-invasive methods for characterization. With regards to the advancement of medical imaging, this work specifically addresses areas of cross modality comparison for identifying and justifying optimal protocols and exploration of imaging biomarkers. This is performed in an animal model system which permits access to complete, validating tissue samples for histopathological, immunohistochemical, and/or molecular correlative studies.

CHAPTER 12: FUTURE WORK

Several projects are planned in continuing the work described. These included incorporating PET imaging as an additional imaging modality, additions to the multi-level registration framework, and extending the feature extraction methods.

12.1 PET imaging

Recently, approval has been obtained through the University of Iowa IACUC for 18F-FDG and 18F-FLT PET/CT imaging to be performed on these animal models. Previous PET imaging was not performed in these animals due to the lack of a research dedicated scanner at our institution resulting in logistical and scheduling challenges. In addition, the use of a radioactive tracer results in a radioactive animal for up to 20 hours after injection depending on the initial dosage requiring specialized housing and husbandry. The installation of a research dedicated PET/CT scanner, scheduled for April 2017, provides more scheduling and logistical flexibility for large animal research. This addition will allow for further characterization of identified tumors and allow for the testing and validation of novel and current radioactive tracers.

12.2 Registration

We designed the multi-level registration algorithm to be modular, allowing for individuals to add additional preprocessing, initialization, or registration algorithms while still maintaining the integrity of the multi-level idea. In the future, we plan to explore improvements aimed at initialization and additional registration options.

One of the limitations for the developed multi-level registration algorithm was the wide variety of initialization techniques used depending on the differences in image coverage. Algorithms have been previously designed to identify similar features in two images and use identified features for landmark based registration. These algorithms have been previously used for multimodal medical image registrations and stitching of MRI images [119, 121]. Future work incorporating these algorithms may provide a more robust initialization of images given a large disparity in image coverage.

The current multi-level registration algorithm utilizes a rigid transform allowing for rotation, translation, and anisotropic scaling. While this has proved well for alignment of longitudinal datasets, the inclusion of an additional non-rigid transform following rigid alignment

is of interest to further improve the overlap of desired structures. Considerations for this algorithm include limitations on the amount of deformation allowed depending on the identified change in disease between time points and the need for it to be inverse consistent for desired use with the longitudinal feature extraction tool.

12.3 Correlation with pathology

We presented the development of a tool for longitudinal feature extraction using the results from the multi-level registration algorithm. Future work includes incorporating the ability to extract additional features from regions of interest in all datasets with regional matching to occur [49]. In addition, we plan to integrate automatic segmentation of structures using an initial identified region propagated through each image. This will expand our ability to analyze change in tumor shape over time. With longitudinal monitoring of tumor progression of models, these quantitative imaging features and characteristics can then be correlated with pathology results for identification and verification of imaging biomarkers [63]. Work has previously been done by Sieren, et al, specifically in lung cancer, focusing on the correlation between CT and histopathology. These developed techniques incorporate a multi-scale imaging approach of complete bio-specimens to understand the representation of tumor heterogeneity in CT through registration with ground truth histopathology [133, 194, 195]. These models present the opportunity to combine longitudinal growth and feature extraction, including regional, analysis with complete bio-specimen histopathology confirmation.

12.4 Additional models

Lastly, continued monitoring is being performed for the radiation exposure heterozygote animals and the conditionally activated *KRAS* animals with the methods described. Additional genetically modified large animal models have been developed by Exemplar Genetics, such as neurofibromatosis 1 (NF1), that are being characterized using these methods with additional models being developed.

REFERENCES

[1]   M. A. Dinan, L. H. Curtis, B. G. Hammill, E. F. Patz, A. P. Abernethy, A. M. Shea, and K. A. Schulman, "Changes in the use and costs of diagnostic imaging among medicare beneficiaries with cancer, 1999-2006," *JAMA,* vol. 303, no. 16, pp. 1625-1631, 2010.

[2]   L. Fass, "Imaging and cancer: A review," *Molecular Oncology,* vol. 2, no. 2, pp. 115-152, 2008.

[3]   M. K. Kalra, M. M. Maher, T. L. Toth, B. Schmidt, B. L. Westerman, H. T. Morgan, and S. Saini, "Techniques and Applications of Automatic Tube Current Modulation for CT," *Radiology,* vol. 233, no. 3, pp. 649-657, 2004.

[4]   C. H. McCollough, M. R. Bruesewitz, and J. M. Kofler, "CT Dose Reduction and Dose Management Tools: Overview of Available Options," *RadioGraphics,* vol. 26, no. 2, pp. 503-512, 2006.

[5]   A. K. Hara, R. G. Paden, A. C. Silva, J. L. Kujak, H. J. Lawder, and W. Pavlicek, "Iterative Reconstruction Technique for Reducing Body Radiation Dose at CT: Feasibility Study," *American Journal of Roentgenology,* vol. 193, no. 3, pp. 764-771, 2009.

[6]   O. M. Mets, M. J. Willemink, and F. P. de Kort, "The effect of iterative reconstruction on computed tomography assessment of emphysema, air trapping and airway dimensions," *Eur Radiol,* vol. 22, pp. 2103-9, 2012.

[7]   M. Beister, D. Kolditz, and W. A. Kalender, "Iterative reconstruction methods in X-ray CT," *Physica Medica,* vol. 28, no. 2, pp. 94-108, 2012.

[8]   U. S. P. S. T. Force, "Screening for breast cancer: U.S. Preventive Services Task Force recommendation statement," *Ann Intern Med,* vol. 151, no. 10, pp. 716-26, W-236, 2009.

[9]   V. A. Moyer, "Screening for Lung Cancer: U.S. Preventive Services Task Force Recommendation Statement," *Annals of Internal Medicine,* vol. 160, no. 5, pp. 330-338, 2014.

[10]   D. R. Aberle, A. M. Adams, C. D. Berg, W. C. Black, J. D. Clapp, R. M. Fagerstrom, I. F. Gareen, C. Gatsonis, P. M. Marcus, and J. D. Sicks, "Reduced lung-cancer mortality with low-dose computed tomographic screening," *N Engl J Med,* vol. 365, no. 5, pp. 395-409, 2011.

[11]   U. S. P. S. T. Force, "Screening for colorectal cancer: Us preventive services task force recommendation statement," *JAMA,* vol. 315, no. 23, pp. 2564-2575, 2016.

[12]   T. Xiong, M. Richardson, R. Woodroffe, S. Halligan, D. Morton, and R. J. Lilford, "Incidental lesions found on CT colonography: their nature and frequency," *Br J Radiol,* vol. 78, no. 925, pp. 22-9, 2005.

[13]   R. Damadian, "Tumor detection by nuclear magnetic resonance," *Science,* vol. 171, no. 976, pp. 1151-1153, 1971.

[14]   A. G. Filler, "The history, development and impact of computed imaging in neurological diagnosis and neurosurgery: CT, MRI, and DTI," *Internet Journal of Neurosurgery,* vol. 7, no. 1, p. 5, 2010.

[15]   M. B. Mainiero, A. Lourenco, M. C. Mahoney, M. S. Newell, L. Bailey, L. D. Barke, C. D'Orsi, J. A. Harvey, M. K. Hayes, P. T. Huynh, P. M. Jokich, S.-J. Lee, C. D. Lehman, D. A. Mankoff, J. A. Nepute, S. B. Patel, H. E. Reynolds, M. L. Sutherland, and B. G. Haffty, "ACR Appropriateness Criteria Breast Cancer Screening," *Journal of the American College of Radiology,* vol. 13, no. 11, Supplement, pp. R45-R49, 2016.

[16]   G. Petralia, L. Bonello, S. Viotti, L. Preda, G. d'Andrea, and M. Bellomi, "CT perfusion in oncology: how to do it," *Cancer Imaging,* vol. 10, no. 1, pp. 8-19, 2010.

[17]   K. A. Miles and M. R. Griffiths, "Perfusion CT: a worthwhile enhancement?," *The British Journal of Radiology,* vol. 76, no. 904, pp. 220-231, 2003.

[18] A. R. Padhani, "Dynamic contrast-enhanced MRI in clinical oncology: Current status and future directions," *Journal of Magnetic Resonance Imaging,* vol. 16, no. 4, pp. 407-422, 2002.

[19] J. P. B. O'Connor, A. Jackson, G. J. M. Parker, C. Roberts, and G. C. Jayson, "Dynamic contrast-enhanced MRI in clinical trials of antivascular therapies," *Nat Rev Clin Oncol,* vol. 9, no. 3, pp. 167-177, 2012.

[20] M. A. Vermoolen, T. C. Kwee, and R. A. Nievelstein, "Apparent diffusion coefficient measurements in the differentiation between benign and malignant lesions: a systematic review," *Insights Imaging,* vol. 3, no. 4, pp. 395-409, 2012.

[21] S. Ben-Haim and P. Ell, "18F-FDG PET and PET/CT in the evaluation of cancer treatment response," *Journal of Nuclear Medicine,* vol. 50, no. 1, pp. 88-99, 2009.

[22] K. Chen and X. Chen, "Positron Emission Tomography Imaging of Cancer Biology: Current Status and Future Prospects," *Seminars in Oncology,* vol. 38, no. 1, pp. 70-86, 2011.

[23] C. Spick, K. Herrmann, and J. Czernin, "18F-FDG PET/CT and PET/MRI perform equally well in cancer: evidence from studies on more than 2,300 patients," *Journal of Nuclear Medicine,* vol. 57, no. 3, pp. 420-430, 2016.

[24] S. B. Edge, D. R. Byrd, C. C. Compton, A. G. Fritz, F. L. Greene, and A. Trotti, *AJCC cancer staging manual*, 2010.

[25] A. Hamamci, N. Kucuk, K. Karaman, K. Engin, and G. Unal, "Tumor-Cut: Segmentation of Brain Tumors on Contrast Enhanced MR Images for Radiosurgery Applications," *Medical Imaging, IEEE Transactions on,* vol. 31, no. 3, pp. 790-804, 2012.

[26] W. Huang, N. Li, Z. Lin, G. B. Huang, W. Zong, J. Zhou, and Y. Duan, "Liver tumor detection and segmentation using kernel-based extreme learning machine," in *2013 35th Annual International Conference of the IEEE Engineering in Medicine and Biology Society (EMBC)*, 2013, pp. 3662-3665.

[27] X. Yang, N. Wu, G. Cheng, Z. Zhou, D. S. Yu, J. J. Beitler, W. J. Curran, and T. Liu, "Automated segmentation of the parotid gland based on atlas registration and machine learning: a longitudinal MRI study in head-and-neck radiation therapy," *Int J Radiat Oncol Biol Phys,* vol. 90, no. 5, pp. 1225-33, 2014.

[28] R. Vivanti, L. Joskowicz, O. A. Karaaslan, and J. Sosna, "Automatic lung tumor segmentation with leaks removal in follow-up CT studies," *International Journal of Computer Assisted Radiology and Surgery,* vol. 10, no. 9, pp. 1505-1514, 2015.

[29] A. P. James and B. V. Dasarathy, "Medical image fusion: A survey of the state of the art," *Information Fusion,* vol. 19, pp. 4-19, 2014.

[30] J. Li, A. Harrison, Y. Yu, Y. Xiao, M. Werner-Wasik, and B. Lu, "Evaluation of Elekta 4D cone beam CT-based automatic image registration for radiation treatment of lung cancer," *Br J Radiol,* vol. 88, no. 1053, p. 20140620, 2015.

[31] G. Cazoulat, D. Owen, M. M. Matuszak, J. M. Balter, and K. K. Brock, "Biomechanical deformable image registration of longitudinal lung CT images using vessel information," *Phys Med Biol,* vol. 61, no. 13, pp. 4826-39, 2016.

[32] W. H. Organization, "WHO handbook for reporting results of cancer treatment," 1979.

[33] E. A. Eisenhauer, P. Therasse, J. Bogaerts, L. H. Schwartz, D. Sargent, R. Ford, J. Dancey, S. Arbuck, S. Gwyther, M. Mooney, L. Rubinstein, L. Shankar, L. Dodd, R. Kaplan, D. Lacombe, and J. Verweij, "New response evaluation criteria in solid tumours: revised RECIST guideline (version 1.1)," *Eur J Cancer,* vol. 45, no. 2, pp. 228-47, 2009.

[34] P. Therasse, S. G. Arbuck, E. A. Eisenhauer, J. Wanders, R. S. Kaplan, L. Rubinstein, J. Verweij, M. Van Glabbeke, A. T. van Oosterom, M. C. Christian, and S. G. Gwyther, "New guidelines to evaluate the response to treatment in solid tumors.," *J Natl Cancer Inst,* vol. 92, no. 3, pp. 205-16, 2000.

[35] T. Tirkes, M. A. Hollar, M. Tann, M. D. Kohli, F. Akisik, and K. Sandrasegaran, "Response Criteria in Oncologic Imaging: Review of Traditional and New Criteria," *RadioGraphics,* vol. 33, no. 5, pp. 1323-1341, 2013.

[36] S. R. Prasad and S. Saini, "Radiological evaluation of oncologic treatment response: current update," *Cancer Imaging,* vol. 3, no. 2, pp. 93-95, 2003.

[37] E. Namati, J. Thiesse, J. C. Sieren, A. Ross, E. A. Hoffman, and G. McLennan, "Longitudinal assessment of lung cancer progression in the mouse using in vivo micro-CT imaging," *Medical Physics,* vol. 37, no. 9, p. 4793, 2010.

[38] S. A. Hayes, M. C. Pietanza, D. O'Driscoll, J. Zheng, C. S. Moskowitz, M. G. Kris, and M. S. Ginsberg, "Comparison of CT volumetric measurement with RECIST response in patients with lung cancer," *European Journal of Radiology,* vol. 85, no. 3, pp. 524-533, 2016.

[39] L. N. Tran, M. S. Brown, J. G. Goldin, X. Yan, R. C. Pais, M. F. McNitt-Gray, D. Gjertson, S. R. Rogers, and D. R. Aberle, "Comparison of treatment response classifications between unidimensional, bidimensional, and volumetric measurements of metastatic lung lesions on chest computed tomography," *Acad Radiol,* vol. 11, no. 12, pp. 1355-60, 2004.

[40] J. H. Rothe, C. Grieser, L. Lehmkuhl, D. Schnapauff, C. P. Fernandez, M. H. Maurer, A. Mussler, B. Hamm, T. Denecke, and I. G. Steffen, "Size determination and response assessment of liver metastases with computed tomography—Comparison of RECIST and volumetric algorithms," *European Journal of Radiology,* vol. 82, no. 11, pp. 1831-1839, 2013.

[41] G. Niculescu, J. L. Nosher, M. D. Schneider, and D. J. Foran, "A deformable model for tracking tumors across consecutive imaging studies," *Int J Comput Assist Radiol Surg,* vol. 4, no. 4, pp. 337-47, 2009.

[42] B. Stefan, W. Roland, P. N. Lutz, and R. Mauricio, "A survey of MRI-based medical image analysis for brain tumor studies," *Physics in Medicine and Biology,* vol. 58, no. 13, p. R97, 2013.

[43] X. Li, R. G. Abramson, L. R. Arlinghaus, A. B. Chakravarthy, V. Abramson, I. Mayer, J. Farley, D. Delbeke, and T. E. Yankeelov, "An algorithm for longitudinal registration of PET/CT images acquired during neoadjuvant chemotherapy in breast cancer: preliminary results," *EJNMMI research,* vol. 2, no. 1, p. 1, 2012.

[44] Y. Ou, S. P. Weinstein, E. F. Conant, S. Englander, X. Da, B. Gaonkar, M. K. Hsieh, M. Rosen, A. DeMichele, C. Davatzikos, and D. Kontos, "Deformable registration for quantifying longitudinal tumor changes during neoadjuvant chemotherapy," *Magn Reson Med,* vol. 73, no. 6, pp. 2343-56, 2015.

[45] A. Salhi, N. Melouah, F. M. Hayet, S. Layachi, and A. Bouguettaya, "Neoadjuvant chemotherapy response evaluation in breast cancer based on mammogram registration and tumor segmentation," *Pattern Recognition and Image Analysis,* vol. 27, no. 1, pp. 122-130, 2017.

[46] K. K. Brock, L. A. Dawson, M. B. Sharpe, D. J. Moseley, and D. A. Jaffray, "Feasibility of a novel deformable image registration technique to facilitate classification, targeting, and monitoring of tumor and normal tissue," *International Journal of Radiation Oncology*Biology*Physics,* vol. 64, no. 4, pp. 1245-1254, 2006.

[47] K. Doi, "Computer-Aided Diagnosis in Medical Imaging: Historical Review, Current Status and Future Potential," *Computerized medical imaging and graphics : the official journal of the Computerized Medical Imaging Society,* vol. 31, no. 4-5, pp. 198-211, 2007.

[48] F. Ng, B. Ganeshan, R. Kozarski, K. A. Miles, and V. Goh, "Assessment of Primary Colorectal Cancer Heterogeneity by Using Whole-Tumor Texture Analysis: Contrast-

enhanced CT Texture as a Biomarker of 5-year Survival," *Radiology,* vol. 266, no. 1, pp. 177-184, 2013.

[49]   S. K. N. Dilger, J. Uthoff, A. Judisch, E. Hammond, S. L. Mott, B. J. Smith, J. J. D. Newell, E. A. Hoffman, and J. C. Sieren, "Improved pulmonary nodule classification utilizing quantitative lung parenchyma features," *Journal of Medical Imaging,* vol. 2, no. 4, pp. 041004-041004, 2015.

[50]   R. A. Gatenby, O. Grove, and R. J. Gillies, "Quantitative Imaging in Cancer Evolution and Ecology," *Radiology,* vol. 269, no. 1, pp. 8-14, 2013.

[51]   P. Lambin, E. Rios-Velazquez, R. Leijenaar, S. Carvalho, R. G. P. M. van Stiphout, P. Granton, C. M. L. Zegers, R. Gillies, R. Boellard, A. Dekker, and H. J. W. L. Aerts, "Radiomics: Extracting more information from medical images using advanced feature analysis," *European Journal of Cancer,* vol. 48, no. 4, pp. 441-446, 2012.

[52]   R. J. Gillies, P. E. Kinahan, and H. Hricak, "Radiomics: Images Are More than Pictures, They Are Data," *Radiology,* vol. 278, no. 2, pp. 563-577, 2015.

[53]   B. F. Kurland, E. R. Gerstner, J. M. Mountz, L. H. Schwartz, C. W. Ryan, M. M. Graham, J. M. Buatti, F. M. Fennessy, E. A. Eikman, V. Kumar, K. M. Forster, R. L. Wahl, and F. S. Lieberman, "Promise and pitfalls of quantitative imaging in oncology clinical trials," *Magnetic Resonance Imaging,* vol. 30, no. 9, pp. 1301-1312, 2012.

[54]   G. C. Kagadis, G. Loudos, K. Katsanos, S. G. Langer, and G. C. Nikiforidis, "In vivo small animal imaging: current status and future prospects," *Medical physics,* vol. 37, no. 12, pp. 6421-6442, 2010.

[55]   M. de Jong, J. Essers, and W. M. van Weerden, "Imaging preclinical tumour models: improving translational power," *Nature Reviews Cancer,* vol. 14, no. 7, pp. 481-493, 2014.

[56]   M. M. Swindle, A. C. Smith, K. Laber-Laird, and L. Dungan, "Swine in biomedical research: management and models," *ILAR Journal,* vol. 36, no. 1, pp. 1-5, 1994.

[57]   P. Vodicka, K. Smetana, B. Dvorankova, T. Emerick, Y. Z. Xu, J. Ourednik, V. Ourednik, and J. Motlík, "The miniature pig as an animal model in biomedical research," *Annals of the New York Academy of Sciences,* vol. 1049, no. 1, pp. 161-171, 2005.

[58]   O. Svendsen, "The minipig in toxicology," *Experimental and Toxicologic Pathology,* vol. 57, no. 5–6, pp. 335-339, 2006.

[59]   M. Swindle, A. Makin, A. Herron, F. Clubb, and K. Frazier, "Swine as models in biomedical research and toxicology testing," *Veterinary Pathology,* vol. 49, no. 2, pp. 344-356, 2012.

[60]   A. L. Watson, D. F. Carlson, D. A. Largaespada, P. B. Hackett, and S. C. Fahrenkrug, "Engineered Swine Models of Cancer," *Frontiers in genetics,* vol. 7, p. 78, 2016.

[61]   T. Flisikowska, C. Merkl, M. Landmann, S. Eser, N. Rezaei, X. Cui, M. Kurome, V. Zakhartchenko, B. Kessler, and H. Wieland, "A porcine model of familial adenomatous polyposis," *Gastroenterology,* vol. 143, no. 5, pp. 1173-1175. e7, 2012.

[62]   S. Leuchs, A. Saalfrank, C. Merkl, T. Flisikowska, M. Edlinger, M. Durkovic, N. Rezaei, M. Kurome, V. Zakhartchenko, B. Kessler, K. Flisikowski, A. Kind, E. Wolf, and A. Schnieke, "Inactivation and inducible oncogenic mutation of p53 in gene targeted pigs," *PLoS One,* vol. 7, no. 10, p. e43323, 2012.

[63]   J. C. Sieren, D. K. Meyerholz, X.-J. Wang, B. T. Davis, J. D. Newell, Jr., E. Hammond, J. A. Rohret, F. A. Rohret, J. T. Struzynski, J. A. Goeken, P. W. Naumann, M. R. Leidinger, A. Taghiyev, R. Van Rheeden, J. Hagen, B. W. Darbro, D. E. Quelle, and C. S. Rogers, "Development and translational imaging of a TP53 porcine tumorigenesis model," *The Journal of Clinical Investigation,* vol. 124, no. 9, pp. 4052-4066, 2014.

[64]   S. Li, M. Edlinger, A. Saalfrank, K. Flisikowski, A. Tschukes, M. Kurome, V. Zakhartchenko, B. Kessler, D. Saur, A. Kind, E. Wolf, A. Schnieke, and T. Flisikowska,

"Viable pigs with a conditionally-activated oncogenic KRAS mutation," *Transgenic Research,* vol. 24, no. 3, pp. 509-517, 2015.

[65] L. B. Schook, T. V. Collares, W. Hu, Y. Liang, F. M. Rodrigues, L. A. Rund, K. M. Schachtschneider, F. K. Seixas, K. Singh, K. D. Wells, E. M. Walters, R. S. Prather, and C. M. Counter, "A Genetic Porcine Model of Cancer," *PLOS ONE,* vol. 10, no. 7, p. e0128864, 2015.

[66] T. Flisikowska, A. Kind, and A. Schnieke, "Pigs as models of human cancers," *Theriogenology,* vol. 86, no. 1, pp. 433-437, 2016.

[67] C. Won, D. Chon, J. Tajik, B. Q. Tran, G. B. Robinswood, K. C. Beck, and E. A. Hoffman, "CT-based assessment of regional pulmonary microvascular blood flow parameters," *Journal of Applied Physiology,* vol. 94, no. 6, pp. 2483-2493, 2003.

[68] S. K. Alford, E. J. van Beek, G. McLennan, and E. A. Hoffman, "Heterogeneity of pulmonary perfusion as a mechanistic image-based phenotype in emphysema susceptible smokers," *Proceedings of the National Academy of Sciences,* vol. 107, no. 16, pp. 7485-7490, 2010.

[69] J. H. Dakin, T. W. Evans, D. M. Hansell, and E. A. Hoffman, "Regional pulmonary blood flow in humans and dogs by 4D computed tomography," *Academic radiology,* vol. 15, no. 7, pp. 844-852, 2008.

[70] G. Dougherty, *Medical Image Processing*, 2011.

[71] B. P. Lelieveldt, C. P. Botha, E. L. Kaijzel, E. A. Hendriks, J. H. Reiber, C. W. Löwik, and J. Dijkstra, "Towards integrated analysis of longitudinal whole-body small animal imaging studies," in *International Conference on Acoustics, Speech, and Signal Processing (ICASSP)*, 2011, pp. 5768-5771.

[72] P. L. Chow, D. B. Stout, E. Komisopoulou, and A. F. Chatziioannou, "A method of image registration for small animal, multi-modality imaging," *Physics in medicine and biology,* vol. 51, no. 2, p. 379, 2006.

[73] D. Mattes, D. R. Haynor, H. Vesselle, T. K. Lewellen, and W. Eubank, "PET-CT image registration in the chest using free-form deformations," *Medical Imaging, IEEE Transactions on,* vol. 22, no. 1, pp. 120-128, 2003.

[74] A. Fedorov, R. Beichel, J. Kalpathy-Cramer, J. Finet, J.-C. Fillion-Robin, S. Pujol, C. Bauer, D. Jennings, F. Fennessy, and M. Sonka, "3D Slicer as an image computing platform for the Quantitative Imaging Network," *Magnetic resonance imaging,* vol. 30, no. 9, pp. 1323-1341, 2012.

[75] N. Aucoin, R. Kikinis, and B. Lorensen. (2014, January 8, 2015). *Model Maker*. Available: http://www.slicer.org/slicerWiki/index.php/Documentation/4.4/Modules/ModelMaker#References

[76] N. M. Ellinwood and C. M. Clay, "Large animal models of genetic disease: pertinent IACUC issues," *ILAR Journal* vol. 50, no. 2, pp. 225-8, 2009.

[77] G. Bode, P. Clausing, F. Gervais, J. Loegsted, J. Luft, V. Nogues, and J. Sims, "The utility of the minipig as an animal model in regulatory toxicology," *Journal of pharmacological and toxicological methods,* vol. 62, no. 3, pp. 196-220, 2010.

[78] J. P. Sieren, E. A. Hoffman, M. K. Fuld, K. S. Chan, J. Guo, and J. D. Newell, "Sinogram Affirmed Iterative Reconstruction (SAFIRE) versus weighted filtered back projection (WFBP) effects on quantitative measure in the COPDGene 2 test object," *Medical Physics,* vol. 41, no. 9, p. 091910, 2014.

[79] S. D. Mobberley, M. K. Fuld, J. P. Sieren, A. N. Primak, and E. A. Hoffman, "Scatter Correction Associated with Dedicated Dual-source CT Hardware Improves Accuracy of Lung Air Measures," *Academic Radiology,* vol. 20, no. 11, pp. 1334-1343, 2013.

[80]   O. M. Mets, M. J. Willemink, and F. P. de Kort, "The effect of iterative reconstruction on computed tomography assessment of emphysema, air trapping and airway dimensions," *Eur Radiol,* vol. 22, no. 10, pp. 2103-9, 2012.

[81]   S. D. Ganz, "Presurgical Planning With CT-Derived Fabrication of Surgical Guides," *Journal of Oral and Maxillofacial Surgery,* vol. 63, no. 9, Supplement, pp. 59-71, 2005.

[82]   L. Moy, M. E. Noz, G. Q. Maguire, Jr., F. Ponzo, A. E. Deans, A. D. Murphy-Walcott, and E. L. Kramer, "Prone mammoPET acquisition improves the ability to fuse MRI and PET breast scans," *Clin Nucl Med,* vol. 32, no. 3, pp. 194-8, 2007.

[83]   L. M. Panepinto, R. W. Phillips, L. R. Wheeler, and D. H. Will, "The Yucatan minature pig as a laboratory animal," *Lab Anim Sci,* vol. 28, no. 3, pp. 308-13, 1978.

[84]   A. M. P. Association. (3/14/2017). *Owner Mini Pig Size Classifications.* Available: http://americanminipigassociation.com/owners/mini-pig-size-classifications/

[85]   C. E. Kahn, Jr., M. E. Heilbrun, and K. E. Applegate, "From Guidelines to Practice: How Reporting Templates Promote the Use of Radiology Practice Guidelines," *Journal of the American College of Radiology,* vol. 10, no. 4, pp. 268-273.

[86]   E. S. Burnside, E. A. Sickles, L. W. Bassett, D. L. Rubin, C. H. Lee, D. M. Ikeda, E. B. Mendelson, P. A. Wilcox, P. F. Butler, and C. J. D'Orsi, "The ACR BI-RADS experience: learning from history," *J Am Coll Radiol,* vol. 6, no. 12, pp. 851-60, 2009.

[87]   A. C. o. R. B.-R. Committee and A. C. o. Radiology, *Breast imaging reporting and data system,* 1998.

[88]   D. B. Kopans, "Standardized mammography reporting," *Radiol Clin North Am,* vol. 30, no. 1, pp. 257-64, 1992.

[89]   A. C. o. Radiology and A. C. o. Radiology, "Breast imaging reporting and data system atlas (BI-RADS atlas)," *Reston, VA: American College of Radiology,* vol. 98, 2003.

[90]   C. M. Hawkins, S. Hall, B. Zhang, and A. J. Towbin, "Creation and Implementation of Department-Wide Structured Reports: An Analysis of the Impact on Error Rate in Radiology Reports," *Journal of Digital Imaging,* vol. 27, no. 5, pp. 581-587, 2014.

[91]   D. B. Larson, A. J. Towbin, R. M. Pryor, and L. F. Donnelly, "Improving Consistency in Radiology Reporting through the Use of Department-wide Standardized Structured Reporting," *Radiology,* vol. 267, no. 1, pp. 240-250, 2013.

[92]   J. M. L. Bosmans, J. J. Weyler, A. M. D. Schepper, and P. M. Parizel, "The Radiology Report as Seen by Radiologists and Referring Clinicians: Results of the COVER and ROVER Surveys," *Radiology,* vol. 259, no. 1, pp. 184-195, 2011.

[93]   L. H. Schwartz, D. M. Panicek, A. R. Berk, Y. Li, and H. Hricak, "Improving communication of diagnostic radiology findings through structured reporting," *Radiology,* vol. 260, no. 1, pp. 174-81, 2011.

[94]   P. A. Marcovici and G. A. Taylor, "JOURNAL CLUB: Structured Radiology Reports Are More Complete and More Effective Than Unstructured Reports," *American Journal of Roentgenology,* vol. 203, no. 6, pp. 1265-1271, 2014.

[95]   A. J. Johnson, M. Y. M. Chen, M. E. Zapadka, E. M. Lyders, and B. Littenberg, "Radiology Report Clarity: A Cohort Study of Structured Reporting Compared With Conventional Dictation," *Journal of the American College of Radiology,* vol. 7, no. 7, pp. 501-506, 2010.

[96]   M. Meyer, H. Haubenreisser, U. J. Schoepf, R. Vliegenthart, C. Leidecker, T. Allmendinger, R. Lehmann, S. Sudarski, M. Borggrefe, S. O. Schoenberg, and T. Henzler, "Closing in on the K Edge: Coronary CT Angiography at 100, 80, and 70 kV— Initial Comparison of a Second- versus a Third-Generation Dual-Source CT System," *Radiology,* vol. 273, no. 2, pp. 373-382, 2014.

[97]   J. C. v. Rijn, N. Klemetso, J. B. Reitsma, P. M. Bossuyt, F. J. Hulsmans, W. C. Peul, G. J. d. Heeten, J. Stam, and C. B. L. M. Majoie, "Observer variation in the evaluation of

lumbar herniated discs and root compression: spiral CT compared with MRI," *The British Journal of Radiology,* vol. 79, no. 941, pp. 372-377, 2006.

[98] C. K. Kuhl, S. Schrading, C. C. Leutner, N. Morakkabati-Spitz, E. Wardelmann, R. Fimmers, W. Kuhn, and H. H. Schild, "Mammography, Breast Ultrasound, and Magnetic Resonance Imaging for Surveillance of Women at High Familial Risk for Breast Cancer," *Journal of Clinical Oncology,* vol. 23, no. 33, pp. 8469-8476, 2005.

[99] E. Hammond, J. D. Newell, S. K. N. Dilger, N. Stoyles, J. Morgan, J. P. Sieren, D. R. Thedens, E. A. Hoffman, D. K. Meyerholz, and J. C. Sieren, "Computed Tomography and Magnetic Resonance Imaging for Longitudinal Characterization of Lung Structure Changes in a Yucatan Miniature Pig Silicosis Model," *Toxicologic Pathology,* vol. 44, no. 3, pp. 373 - 381, 2016.

[100] C. E. Kahn Jr, C. P. Langlotz, E. S. Burnside, J. A. Carrino, D. S. Channin, D. M. Hovsepian, and D. L. Rubin, "Toward Best Practices in Radiology Reporting 1," *Radiology,* vol. 252, no. 3, pp. 852-856, 2009.

[101] A. L. Alexander, J. E. Lee, M. Lazar, and A. S. Field, "Diffusion Tensor Imaging of the Brain," *Neurotherapeutics : the journal of the American Society for Experimental NeuroTherapeutics,* vol. 4, no. 3, pp. 316-329, 2007.

[102] D. M. Hansell, A. A. Bankier, H. MacMahon, T. C. McLoud, N. L. Muller, and J. Remy, "Fleischner society: glossary of terms for thoracic imaging 1," *Radiology,* vol. 246, no. 3, pp. 697-722, 2008.

[103] K. M. Johnson, S. B. Fain, M. L. Schiebler, and S. Nagle, "Optimized 3D ultrashort echo time pulmonary MRI," *Magnetic Resonance in Medicine,* vol. 70, no. 5, pp. 1241-1250, 2013.

[104] L. C. Bell, K. M. Johnson, S. B. Fain, A. Wentland, R. Drees, R. A. Johnson, G. Bauman, C. J. Francois, and S. K. Nagle, "Simultaneous MRI of lung structure and perfusion in a single breathhold," *Journal of Magnetic Resonance Imaging,* vol. 41, no. 1, pp. 52-59, 2015.

[105] G. Antoch, F. M. Vogt, L. S. Freudenberg, F. Nazaradeh, S. C. Goehde, J. Barkhausen, G. Dahmen, A. Bockisch, J. F. Debatin, and S. G. Ruehm, "Whole-body dual-modality pet/ct and whole-body mri for tumor staging in oncology," *JAMA,* vol. 290, no. 24, pp. 3199-3206, 2003.

[106] D. Takenaka, Y. Ohno, K. Matsumoto, N. Aoyama, Y. Onishi, H. Koyama, M. Nogami, T. Yoshikawa, S. Matsumoto, and K. Sugimura, "Detection of bone metastases in non-small cell lung cancer patients: Comparison of whole-body diffusion-weighted imaging (DWI), whole-body MR imaging without and with DWI, whole-body FDG-PET/CT, and bone scintigraphy," *Journal of Magnetic Resonance Imaging,* vol. 30, no. 2, pp. 298-308, 2009.

[107] R. C. Semelka, D. M. Armao, J. Elias, and W. Huda, "Imaging strategies to reduce the risk of radiation in CT studies, including selective substitution with MRI," *Journal of Magnetic Resonance Imaging,* vol. 25, no. 5, pp. 900-909, 2007.

[108] M. Puderbach, M. Eichinger, J. Gahr, S. Ley, S. Tuengerthal, A. Schmähl, C. Fink, C. Plathow, M. Wiebel, F.-M. Müller, and H.-U. Kauczor, "Proton MRI appearance of cystic fibrosis: Comparison to CT," *European Radiology,* vol. 17, no. 3, pp. 716-724, 2007.

[109] M. Puderbach, M. Eichinger, J. Haeselbarth, S. Ley, A. Kopp-Schneider, S. Tuengerthal, A. Schmaehl, C. Fink, C. Plathow, M. Wiebel, S. Demirakca, F.-M. Müller, and H.-U. Kauczor, "Assessment of Morphological MRI for Pulmonary Changes in Cystic Fibrosis (CF) Patients: Comparison to Thin-Section CT and Chest X-ray," *Investigative Radiology,* vol. 42, no. 10, pp. 715-724, 2007.

[110] P. Ciet, G. Serra, S. Bertolo, S. Spronk, M. Ros, F. Fraioli, S. Quattrucci, M. B. Assael, C. Catalano, and F. Pomerri, "Assessment of CF lung disease using motion corrected

PROPELLER MRI: a comparison with CT," *European radiology,* vol. 26, no. 3, pp. 780-787, 2016.

[111]   T. D. Cannon, Y. Chung, G. He, D. Sun, A. Jacobson, T. G. M. van Erp, S. McEwen, J. Addington, C. E. Bearden, K. Cadenhead, B. Cornblatt, D. H. Mathalon, T. McGlashan, D. Perkins, C. Jeffries, L. J. Seidman, M. Tsuang, E. Walker, S. W. Woods, and R. Heinssen, "Progressive Reduction in Cortical Thickness as Psychosis Develops: A Multisite Longitudinal Neuroimaging Study of Youth at Elevated Clinical Risk," *Biological psychiatry,* vol. 77, no. 2, pp. 147-157, 2015.

[112]   H. D. Nelson, K. Tyne, A. Naik, C. Bougatsos, B. K. Chan, and L. Humphrey, "Screening for breast cancer: An update for the u.s. preventive services task force," *Annals of Internal Medicine,* vol. 151, no. 10, pp. 727-737, 2009.

[113]   J. J. Kwak, S. H. Tirumani, A. D. V. d. Abbeele, P. J. Koo, and H. A. Jacene, "Cancer Immunotherapy: Imaging Assessment of Novel Treatment Response Patterns and Immune-related Adverse Events," *RadioGraphics,* vol. 35, no. 2, pp. 424-437, 2015.

[114]   J. Tian, Y. Wang, X. Dai, and X. Zhang, "Medical Image Processing and Analysis," in *Molecular Imaging: Fundamentals and Applications*, 2013, pp. 415-469.

[115]   J. Guo, M. Fuld, S. Alford, J. Reinhardt, and E. Hoffman, "Pulmonary Analysis Software Suite 9.0: Integrating quantitative measures of function with structural analyses," *Proceedings of the First International Workshop on Pulmonary Image Analysis,* pp. 283-292, 2008.

[116]   A. Klein, J. Andersson, B. A. Ardekani, J. Ashburner, B. Avants, M. C. Chiang, G. E. Christensen, D. L. Collins, J. Gee, P. Hellier, J. H. Song, M. Jenkinson, C. Lepage, D. Rueckert, P. Thompson, T. Vercauteren, R. P. Woods, J. J. Mann, and R. V. Parsey, "Evaluation of 14 nonlinear deformation algorithms applied to human brain MRI registration," *Neuroimage,* vol. 46, no. 3, pp. 786-802, 2009.

[117]   N. C. Atuegwu, X. Li, L. R. Arlinghaus, R. G. Abramson, J. M. Williams, A. B. Chakravarthy, V. G. Abramson, and T. E. Yankeelov, "Longitudinal, intermodality registration of quantitative breast PET and MRI data acquired before and during neoadjuvant chemotherapy: preliminary results," *Med Phys,* vol. 41, no. 5, p. 052302, 2014.

[118]   G. M. Fleishman, B. A. Gutman, P. T. Fletcher, and P. M. Thompson, "Simultaneous Longitudinal Registration with Group-Wise Similarity Prior," *Inf Process Med Imaging,* vol. 24, pp. 746-57, 2015.

[119]   W. Cheung and G. Hamarneh, "N-sift: N-dimensional scale invariant feature transform for matching medical images," in *Biomedical Imaging: From Nano to Macro, 2007. ISBI 2007. 4th IEEE International Symposium on*, 2007, pp. 720-723.

[120]   D. Zhao, Y. Yang, Z. Ji, and X. Hu, "Rapid multimodality registration based on MM-SURF," *Neurocomputing,* vol. 131, pp. 87-97, 2014.

[121]   D.-H. Lee, D.-W. Lee, and B.-S. Han, "Possibility Study of Scale Invariant Feature Transform (SIFT) Algorithm Application to Spine Magnetic Resonance Imaging," *PloS one,* vol. 11, no. 4, p. e0153043, 2016.

[122]   H. Lester and S. R. Arridge, "A survey of hierarchical non-linear medical image registration," *Pattern recognition,* vol. 32, no. 1, pp. 129-149, 1999.

[123]   S. Somayajula, A. A. Joshi, and R. M. Leahy, "Mutual information based non-rigidmouse registration using a scale-space approach," in *2008 5th IEEE International Symposium on Biomedical Imaging: From Nano to Macro*, 2008, pp. 1147-1150.

[124]   M. R. Bernsen, K. Kooiman, M. Segbers, F. W. van Leeuwen, and M. de Jong, "Biomarkers in preclinical cancer imaging," *Eur J Nucl Med Mol Imaging,* vol. 42, no. 4, pp. 579-96, 2015.

[125]   C. Plathow, M. Klopp, C. Thieke, F. Herth, A. Thomas, A. Schmaehl, I. Zuna, and H. U. Kauczor, "Therapy response in malignant pleural mesothelioma-role of MRI using

RECIST, modified RECIST and volumetric approaches in comparison with CT," *Eur Radiol,* vol. 18, no. 8, pp. 1635-43, 2008.

[126] K. Marten, F. Auer, S. Schmidt, G. Kohl, E. J. Rummeny, and C. Engelke, "Inadequacy of manual measurements compared to automated CT volumetry in assessment of treatment response of pulmonary metastases using RECIST criteria," *European Radiology,* vol. 16, no. 4, pp. 781-790, 2006.

[127] Ç. Öztürk, T. Velleman, A. H. Bongaerts, L. Bergman, R. J. van Ginkel, J. A. Gietema, and H. J. Hoekstra, "Assessment of Volumetric versus Manual Measurement in Disseminated Testicular Cancer; No Difference in Assessment between Non-Radiologists and Genitourinary Radiologist," *PLOS ONE,* vol. 12, no. 1, p. e0168977, 2017.

[128] K. Doi, "Computer-aided diagnosis in medical imaging: Historical review, current status and future potential," *Computerized Medical Imaging and Graphics,* vol. 31, no. 4–5, pp. 198-211, 2007.

[129] S. Takashima, Y. Maruyama, M. Hasegawa, T. Yamanda, T. Honda, M. Kadoya, and S. Sone, "CT Findings and Progression of Small Peripheral Lung Neoplasms Having a Replacement Growth Pattern," *American Journal of Roentgenology,* vol. 180, no. 3, pp. 817-826, 2003.

[130] T. Aoki, H. Nakata, H. Watanabe, K. Nakamura, T. Kasai, H. Hashimoto, K. Yasumoto, and M. Kido, "Evolution of Peripheral Lung Adenocarcinomas," *American Journal of Roentgenology,* vol. 174, no. 3, pp. 763-768, 2000.

[131] R. L. Siegel, K. D. Miller, and A. Jemal, "Cancer statistics, 2015," *CA: a cancer journal for clinicians,* vol. 65, no. 1, pp. 5-29, 2015.

[132] A. Marusyk and K. Polyak, "Tumor heterogeneity: causes and consequences," *Biochimica et biophysica acta,* vol. 1805, no. 1, p. 105, 2010.

[133] J. C. Sieren, A. R. Smith, J. Thiesse, E. Namati, E. A. Hoffman, J. Kline, and G. McLennan, "Exploration of the Volumetric Composition of Human Lung Cancer Nodules in Correlated Histopathology and Computed Tomography," *Lung cancer (Amsterdam, Netherlands),* vol. 74, no. 1, pp. 61-68, 2011.

[134] A. Karahaliou, S. Skiadopoulos, I. Boniatis, P. Sakellaropoulos, E. Likaki, G. Panayiotakis, and L. Costaridou, "Texture analysis of tissue surrounding microcalcifications on mammograms for breast cancer diagnosis," *The British Journal of Radiology,* vol. 80, no. 956, pp. 648-656, 2007.

[135] G. E. Christensen and H. J. Johnson, "Consistent image registration," *IEEE transactions on medical imaging,* vol. 20, no. 7, pp. 568-582, 2001.

[136] (October 26, 2016). http://www.slicer.org.

[137] R. Kandwal, A. Kumar, and S. Bhargava, "Review: existing image segmentation techniques," *International Journal of Advanced Research in Computer Science and Software Engineering,* vol. 4, no. 4, pp. 153-156, 2014.

[138] C. C. Jaffe, "Measures of Response: RECIST, WHO, and New Alternatives," *Journal of Clinical Oncology,* vol. 24, no. 20, pp. 3245-3251, 2006.

[139] K. E. Nichols, D. Malkin, J. E. Garber, J. F. Fraumeni, and F. P. Li, "Germ-line p53 mutations predispose to a wide spectrum of early-onset cancers," *Cancer Epidemiology Biomarkers & Prevention,* vol. 10, no. 2, pp. 83-87, 2001.

[140] A. J. Levine and M. Oren, "The first 30 years of p53: growing ever more complex," *Nature Reviews Cancer,* vol. 9, no. 10, pp. 749-758, 2009.

[141] K. P. Olive, D. A. Tuveson, Z. C. Ruhe, B. Yin, N. A. Willis, R. T. Bronson, D. Crowley, and T. Jacks, "Mutant p53 gain of function in two mouse models of Li-Fraumeni syndrome," *Cell,* vol. 119, no. 6, pp. 847-860, 2004.

[142] C. Kuperwasser, G. D. Hurlbut, F. S. Kittrell, E. S. Dickinson, R. Laucirica, D. Medina, S. P. Naber, and D. J. Jerry, "Development of spontaneous mammary tumors in BALB/c

p53 heterozygous mice: a model for Li-Fraumeni syndrome," *The American journal of pathology,* vol. 157, no. 6, pp. 2151-2159, 2000.

[143] G. A. Lang, T. Iwakuma, Y.-A. Suh, G. Liu, V. A. Rao, J. M. Parant, Y. A. Valentin-Vega, T. Terzian, L. C. Caldwell, and L. C. Strong, "Gain of function of a p53 hot spot mutation in a mouse model of Li-Fraumeni syndrome," *Cell,* vol. 119, no. 6, pp. 861-872, 2004.

[144] K. A. Hill, V. L. Buettner, A. Heidt, L.-L. Chen, W. Li, K. D. Gonzalez, J.-C. Wang, W. A. Scaringe, and S. S. Sommer, "Most spontaneous tumors in a mouse model of Li-Fraumeni syndrome do not have a mutator phenotype," *Carcinogenesis,* vol. 27, no. 9, pp. 1860-1866, 2006.

[145] J. M. Henderson, S. B. Heymsfield, J. Horowitz, and M. H. Kutner, "Measurement of liver and spleen volume by computed tomography. Assessment of reproducibility and changes found following a selective distal splenorenal shunt," *Radiology,* vol. 141, no. 2, pp. 525-527, 1981.

[146] O. W. Hamer, D. A. Aguirre, G. Casola, J. E. Lavine, M. Woenckhaus, and C. B. Sirlin, "Fatty Liver: Imaging Patterns and Pitfalls," *RadioGraphics,* vol. 26, no. 6, pp. 1637-1653, 2006.

[147] A. S. Bezerra, G. D'Ippolito, S. Faintuch, J. Szejnfeld, and M. Ahmed, "Determination of Splenomegaly by CT: Is There a Place for a Single Measurement?," *American Journal of Roentgenology,* vol. 184, no. 5, pp. 1510-1513, 2005.

[148] S. Surget, M. P. Khoury, and J.-C. Bourdon, "Uncovering the role of p53 splice variants in human malignancy: a clinical perspective," *OncoTargets and therapy,* vol. 7, pp. 57-68, 2013.

[149] T. Jacks, L. Remington, B. O. Williams, E. M. Schmitt, S. Halachmi, R. T. Bronson, and R. A. Weinberg, "Tumor spectrum analysis in p53-mutant mice," *Current Biology,* vol. 4, no. 1, pp. 1-7, 1994.

[150] M. Olivier, D. E. Goldgar, N. Sodha, H. Ohgaki, P. Kleihues, P. Hainaut, and R. A. Eeles, "Li-Fraumeni and Related Syndromes: Correlation between Tumor Type, Family Structure, and TP53 Genotype," *Cancer Research,* vol. 63, no. 20, pp. 6643-6650, 2003.

[151] V. Gylys-Morin, F. Hoffer, H. Kozakewich, and R. Shamberger, "Wilms tumor and nephroblastomatosis: imaging characteristics at gadolinium-enhanced MR imaging," *Radiology,* vol. 188, no. 2, pp. 517-521, 1993.

[152] J. O'Neill, N. Schuff, W. J. Marks, R. Feiwell, M. J. Aminoff, and M. W. Weiner, "Quantitative 1H magnetic resonance spectroscopy and MRI of Parkinson's disease," *Movement Disorders,* vol. 17, no. 5, pp. 917-927, 2002.

[153] S. M. Galbraith, M. A. Lodge, N. J. Taylor, G. J. S. Rustin, S. Bentzen, J. J. Stirling, and A. R. Padhani, "Reproducibility of dynamic contrast-enhanced MRI in human muscle and tumours: comparison of quantitative and semi-quantitative analysis," *NMR in Biomedicine,* vol. 15, no. 2, pp. 132-142, 2002.

[154] N. Howlader, A. Noone, M. Krapcho, J. Garshell, D. Miller, S. Altekruse, C. Kosary, M. Yu, J. Ruhl, and Z. Tatalovich, "SEER Cancer Statistics Review, 1975–2011. Bethesda, MD: National Cancer Institute," ed, 2014.

[155] C. Scoccianti, A. Vesin, G. Martel, M. Olivier, E. Brambilla, J.-F. Timsit, L. Tavecchio, C. Brambilla, J. K. Field, and P. Hainaut, "Prognostic value of TP53, KRAS and EGFR mutations in nonsmall cell lung cancer: the EUELC cohort," *European Respiratory Journal,* vol. 40, no. 1, pp. 177-184, 2012.

[156] U. Saffiotti, "Lung cancer induction by crystalline silica," *Progress in clinical and biological research,* vol. 374, pp. 51-69, 1991.

[157] H. Muhle, B. Kittel, H. Ernst, U. Mohr, and R. Mermelstein, "Neoplastic lung lesions in rat after chronic exposure to crystalline silica," *Scandinavian journal of work, environment & health,* vol. 21 Suppl. 2, pp. 27-29, 1995.

[158] C. Pelucchi, E. Pira, G. Piolatto, M. Coggiola, P. Carta, and C. La Vecchia, "Occupational silica exposure and lung cancer risk: a review of epidemiological studies 1996–2005," *Annals of Oncology,* vol. 17, no. 7, pp. 1039-1050, 2006.

[159] K. Steenland, A. Mannetje, P. Boffetta, L. Stayner, M. Attfield, J. Chen, M. Dosemeci, N. DeKlerk, E. Hnizdo, and R. Koskela, "Pooled exposure–response analyses and risk assessment for lung cancer in 10 cohorts of silica-exposed workers: an IARC multicentre study," *Cancer Causes & Control,* vol. 12, no. 9, pp. 773-784, 2001.

[160] S. Matsumoto, H. Mori, H. Miyake, Y. Yamada, S. Ueda, M. Oga, H. Takeoka, and K. Anan, "MRI signal characteristics of progressive massive fibrosis in silicosis," *Clinical radiology,* vol. 53, no. 7, pp. 510-514, 1998.

[161] J. Mosiewicz, W. Myslinski, G. Zlomaniec, R. Czabak-Garbacz, W. Krupski, and G. Dzida, "Diagnostic value of high resolution computed tomography in the assessment of nodular changes in pneumoconiosis in foundry workers in Lublin," *Annals of Agricultural and Environmental Medicine,* vol. 11, no. 2, pp. 279-284, 2004.

[162] J. D. Schroeder, A. S. McKenzie, J. A. Zach, C. G. Wilson, D. Curran-Everett, D. S. Stinson, J. D. Newell, and D. A. Lynch, "Relationships Between Airflow Obstruction and Quantitative CT Measurements of Emphysema, Air Trapping, and Airways in Subjects With and Without Chronic Obstructive Pulmonary Disease," *American Journal of Roentgenology,* vol. 201, no. 3, pp. W460-W470, 2013.

[163] B. M. Smith, E. A. Hoffman, D. Rabinowitz, E. Bleecker, S. Christenson, D. Couper, K. M. Donohue, M. K. Han, N. N. Hansel, R. E. Kanner, E. Kleerup, S. Rennard, and R. G. Barr, "Comparison of spatially matched airways reveals thinner airway walls in COPD. The Multi-Ethnic Study of Atherosclerosis (MESA) COPD Study and the Subpopulations and Intermediate Outcomes in COPD Study (SPIROMICS)," *Thorax,* vol. 69, no. 11, pp. 987-996, 2014.

[164] F. L. Rice, R. Park, L. Stayner, R. Smith, S. Gilbert, and H. Checkoway, "Crystalline silica exposure and lung cancer mortality in diatomaceous earth industry workers: a quantitative risk assessment," *Occupational and Environmental Medicine,* vol. 58, no. 1, p. 38, 2001.

[165] H. Checkoway, J. M. Hughes, H. Weill, N. S. Seixas, and P. A. Demers, "Crystalline silica exposure, radiological silicosis, and lung cancer mortality in diatomaceous earth industry workers," *Thorax,* vol. 54, no. 1, p. 56, 1999.

[166] N. M. Cherry, G. L. Burgess, S. Turner, and J. C. McDonald, "Crystalline silica and risk of lung cancer in the potteries," *Occupational and Environmental Medicine,* vol. 55, no. 11, p. 779, 1998.

[167] F. Wong, J. D. Boice, D. H. Abramson, R. E. Tarone, R. A. Kleinerman, M. Stovall, M. B. Goldman, J. M. Seddon, N. Tarbell, J. F. Fraumeni, and F. P. Li, "Cancer incidence after retinoblastoma: Radiation dose and sarcoma risk," *JAMA,* vol. 278, no. 15, pp. 1262-1267, 1997.

[168] A. Taghian, F. de Vathaire, P. Terrier, M. Le, A. Auquier, H. Mouriesse, E. Grimaud, D. Sarrazin, and M. Tubiana, "Long-term risk of sarcoma following radiation treatment for breast cancer," *Int J Radiat Oncol Biol Phys,* vol. 21, no. 2, pp. 361-7, 1991.

[169] M. Hisada, J. E. Garber, F. P. Li, C. Y. Fung, and J. F. Fraumeni, "Multiple primary cancers in families with Li-Fraumeni syndrome," *Journal of the National Cancer Institute,* vol. 90, no. 8, pp. 606-611, 1998.

[170] C. J. Kemp, T. Wheldon, and A. Balmain, "p53-deficient mice are extremely susceptible to radiation-induced tumorigenesis," *Nature genetics,* vol. 8, no. 1, pp. 66-69, 1994.

[171] J. M. Lee, J. Abrahamson, R. Kandel, L. A. Donehower, and A. Bernstein, "Susceptibility to radiation-carcinogenesis and accumulation of chromosomal breakage in p53 deficient mice," *Oncogene,* vol. 9, no. 12, pp. 3731-3736, 1994.

[172]   S. Salah, R. Ahmad, I. Sultan, S. Yaser, and A. Shehadeh, "Osteosarcoma with metastasis at initial diagnosis: Current outcomes and prognostic factors in the context of a comprehensive cancer center," *Molecular and clinical oncology,* vol. 2, no. 5, pp. 811-816, 2014.

[173]   A. Luetke, P. A. Meyers, I. Lewis, and H. Juergens, "Osteosarcoma treatment – Where do we stand? A state of the art review," *Cancer Treatment Reviews,* vol. 40, no. 4, pp. 523-532, 2014.

[174]   C. Li, D. Jin, C. Chen, E. M. Letuchy, K. F. Janz, T. L. Burns, J. C. Torner, S. M. Levy, and P. K. Saha, "Automated cortical bone segmentation for multirow-detector CT imaging with validation and application to human studies," *Medical Physics,* vol. 42, no. 8, pp. 4553-4565, 2015.

[175]   A. M. Aisen, W. Martel, E. M. Braunstein, K. I. McMillin, W. A. Phillips, and T. Kling, "MRI and CT evaluation of primary bone and soft-tissue tumors," *American journal of Roentgenology,* vol. 146, no. 4, pp. 749-756, 1986.

[176]   M. D. Bucknor, V. Rieke, L. Do, S. Majumdar, T. M. Link, and M. Saeed, "MRI-guided high-intensity focused ultrasound ablation of bone: Evaluation of acute findings with MR and CT imaging in a swine model," *Journal of Magnetic Resonance Imaging,* vol. 40, no. 5, pp. 1174-1180, 2014.

[177]   E. Y. Chang, J. Du, and C. B. Chung, "UTE Imaging in the Musculoskeletal System," *Journal of magnetic resonance imaging,* vol. 41, no. 4, pp. 870-883, 2015.

[178]   F. Del Grande, F. Santini, D. A. Herzka, M. R. Aro, C. W. Dean, G. E. Gold, and J. A. Carrino, "Fat-Suppression Techniques for 3-T MR Imaging of the Musculoskeletal System," *RadioGraphics,* vol. 34, no. 1, pp. 217-233, 2014.

[179]   S. M. Gillette, E. L. Gillette, B. E. Powers, and S. J. Withrow, "Radiation-induced Osteosarcoma in Dogs after External Beam or Intraoperative Radiation Therapy," *Cancer Research,* vol. 50, no. 1, p. 54, 1990.

[180]   H. Suit, S. Goldberg, A. Niemierko, M. Ancukiewicz, E. Hall, M. Goitein, W. Wong, and H. Paganetti, "Secondary Carcinogenesis in Patients Treated with Radiation: A Review of Data on Radiation-Induced Cancers in Human, Non-human Primate, Canine and Rodent Subjects," *Radiation Research,* vol. 167, no. 1, pp. 12-42, 2007.

[181]   G. P. Gupta and J. Massagué, "Cancer Metastasis: Building a Framework," *Cell,* vol. 127, no. 4, pp. 679-695, 2006.

[182]   B. Vogelstein and K. W. Kinzler, "Cancer genes and the pathways they control," *Nature medicine,* vol. 10, no. 8, pp. 789-799, 2004.

[183]   R. S. Herbst, J. V. Heymach, and S. M. Lippman, "Lung cancer," *N Engl J Med,* vol. 359, no. 13, pp. 1367-80, 2008.

[184]   D. A. Tuveson and T. Jacks, "Modeling human lung cancer in mice: similarities and shortcomings," *Oncogene,* vol. 18, no. 38, pp. 5318-24, 1999.

[185]   E. L. Jackson, K. P. Olive, D. A. Tuveson, R. Bronson, D. Crowley, M. Brown, and T. Jacks, "The differential effects of mutant p53 alleles on advanced murine lung cancer," *Cancer Res,* vol. 65, no. 22, pp. 10280-8, 2005.

[186]   M. A. Collins, F. Bednar, Y. Zhang, J.-C. Brisset, Galb, xE, S. n, Galb, xE, C. J. n, S. Rakshit, K. S. Flannagan, N. V. Adsay, and M. Pasca di Magliano, "Oncogenic Kras is required for both the initiation and maintenance of pancreatic cancer in mice," *The Journal of Clinical Investigation,* vol. 122, no. 2, pp. 639-653, 2012.

[187]   T. Deramaudt and A. K. Rustgi, "Mutant KRAS in the initiation of pancreatic cancer," *Biochimica et Biophysica Acta (BBA) - Reviews on Cancer,* vol. 1756, no. 2, pp. 97-101, 2005.

[188]   H. I. Pass and International Association for the Study of Lung Cancer., *Principles and practice of lung cancer : the official reference text of the IASLC*, 4th ed., 2010.

[189]   Y. Zhang, L. Wang, F. Luo, B. Qiu, L. Guo, Z. Weng, Z. Lin, and G. Chen, "An electrochemiluminescence biosensor for Kras mutations based on locked nucleic acid functionalized DNA walkers and hyperbranched rolling circle amplification," *Chemical Communications,* vol. 53, pp. 2910-2913, 2017.

[190]   S. Jones, X. Zhang, D. W. Parsons, J. C.-H. Lin, R. J. Leary, P. Angenendt, P. Mankoo, H. Carter, H. Kamiyama, A. Jimeno, S.-M. Hong, B. Fu, M.-T. Lin, E. S. Calhoun, M. Kamiyama, K. Walter, T. Nikolskaya, Y. Nikolsky, J. Hartigan, D. R. Smith, M. Hidalgo, S. D. Leach, A. P. Klein, E. M. Jaffee, M. Goggins, A. Maitra, C. Iacobuzio-Donahue, J. R. Eshleman, S. E. Kern, R. H. Hruban, R. Karchin, N. Papadopoulos, G. Parmigiani, B. Vogelstein, V. E. Velculescu, and K. W. Kinzler, "Core Signaling Pathways in Human Pancreatic Cancers Revealed by Global Genomic Analyses," *Science,* vol. 321, no. 5897, pp. 1801-1806, 2008.

[191]   M. Scialpi, A. Reginelli, A. D'Andrea, S. Gravante, G. Falcone, P. Baccari, L. Manganaro, B. Palumbo, and S. Cappabianca, "Pancreatic tumors imaging: An update," *International Journal of Surgery,* vol. 28, Supplement 1, pp. S142-S155, 2016.

[192]   E. Hammond, C. Sloan, J. D. Newell, J. P. Sieren, M. Saylor, C. Vidal, S. Hogue, F. De Stefano, A. Sieren, E. A. Hoffman, and J. C. Sieren, "Comparison of Low and Ultra-Low Dose Computed Tomography Protocols For Quantitative Lung and Airway Assessment," *Medical Physics,* vol. In review, 2017.

[193]   A. J. Aguirre, N. Bardeesy, M. Sinha, L. Lopez, D. A. Tuveson, J. Horner, M. S. Redston, and R. A. DePinho, "Activated Kras and Ink4a/Arf deficiency cooperate to produce metastatic pancreatic ductal adenocarcinoma," *Genes Dev,* vol. 17, no. 24, pp. 3112-26, 2003.

[194]   J. C. Sieren, J. Weydert, A. Bell, B. De Young, A. R. Smith, J. Thiesse, E. Namati, and G. McLennan, "An Automated Segmentation Approach for Highlighting the Histological Complexity of Human Lung Cancer," *Annals of biomedical engineering,* vol. 38, no. 12, pp. 3581-3591, 2010.

[195]   J. C. Sieren, J. Weydert, E. Namati, J. Thiesse, J. P. Sieren, J. M. Reinhardt, E. A. Hoffman, and G. McLennan, "A Process Model for Direct Correlation between Computed Tomography and Histopathology: Application in Lung Cancer," *Academic radiology,* vol. 17, no. 2, pp. 169-180, 2010.